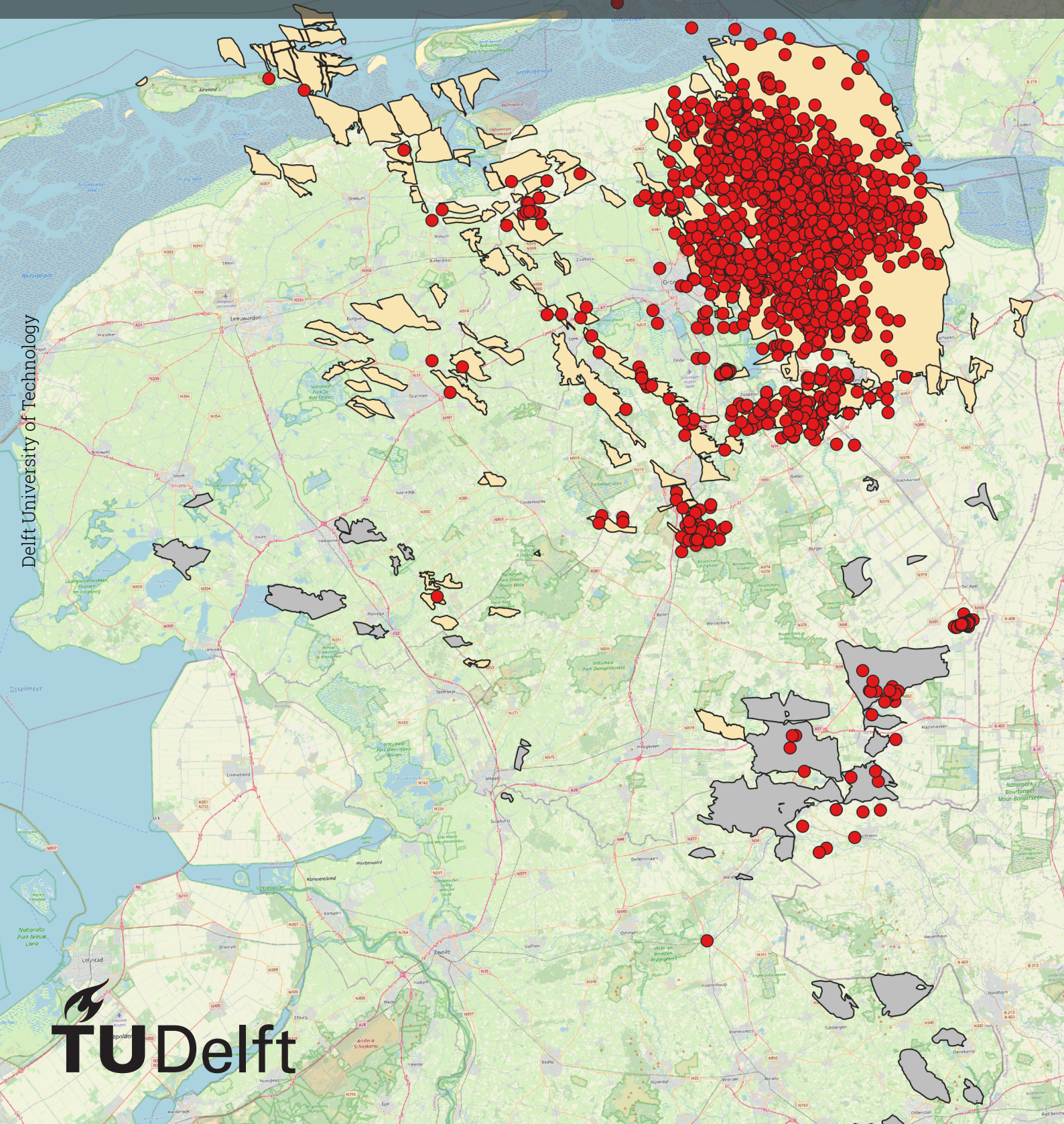


On the impact of the viscous Zechstein formation on the state of stress and seismicity in the North Eastern Netherlands

Tom Leltz



Delft University of Technology



On the impact of the viscous Zechstein formation on the state of stress and seismicity in the North Eastern Netherlands

by

Tom Leltz

to obtain the degree of Master of Science
at the Delft University of Technology,
to be defended publicly on Wednesday June 26, 2024 at 11:00 AM.

Student number: 5172594
Project duration: February 5, 2024 – June 26, 2024
Thesis committee: Dr. Ir. F.C. Vossepoel, TU Delft, supervisor
Dr. A.G. Muntendam-Bos, TU Delft, supervisor

This thesis is confidential and cannot be made public until December 31, 2024.

Cover: Overview of induced seismicity, the Zechstein-2 Carbonate (grey) and Rotliegend (yellow) gas fields in the Northeast Netherlands (created with QGIS3). Seismic data from KNMI and gas field files from NLOG.
Style: TU Delft Report Style

An electronic version of this thesis is available at <http://repository.tudelft.nl/>.

Abstract

This study investigates the impact of the viscous properties of the Zechstein formation on the state of stress and (a) seismic slip in depleting gas reservoirs. I have put the focus on the Rotliegend and Zechstein-2 Carbonate gas fields in the Northeast Netherlands. Six geomechanical models (four Rotliegend and two Carbonate) different were created in Plaxis, representing a fault in various gas fields. For the Carbonate models and two Rotliegend models, the halite is juxtaposed to the reservoir, while for the other two Rotliegend models, the halite is not juxtaposed to the reservoir. The models were simulated with both elastic and viscous properties for the Zechstein halite. Deformations and stresses were calculated around and on the fault using the finite element method.

The viscous property led to a significant increase in strain deformation in the halite and the reservoir juxtaposed to the halite, resulting in a greater compaction in the reservoir next to the halite. The change in strain in other layers was limited with the viscous property.

With depletion the stress ratio decreased in the reservoir and juxtaposed layers, increasing the risk of fault reactivation. In the layers above and below the reservoir, the stress ratio increased, moving away from criticality. While the pattern of stress change with depletion was similar for both elastic and viscous models, the magnitude differed.

For the viscous model, the stress ratio in the layers next to the halite are larger with respect to the elastic model. The high horizontal stresses of the halite significantly decreased the horizontal stresses and, consequently, the stress ratio in the Basal Zechstein below the Halite. Deeper in the reservoir, the decrease in vertical stress between the elastic and viscous was larger than the decrease in horizontal stress, resulting in a slightly larger stress ratio for the viscous model, moving the fault away from criticality. In some models, a slip patch was identified for the elastic model but not for the viscous model. Therefore, it can be concluded that a larger pore pressure depletion is needed for fault reactivation.

The difference in stress and slip between the elastic and viscous model were more pronounced when the halite was juxtaposed to the reservoir. Smaller stress changes and differences between the elastic and viscous were observed for the Carbonate reservoir compared to the Rotliegend reservoirs, due to the greater resistance to deformation. This results in a lower risk of fault reactivation with reservoir depletion. Fault reactivation is also not identified for the Carbonate models.

Acknowledgements

The past five months I have been working on my thesis, during which I received essential support and help from a number of people.

I would like to express my gratitude to my two supervisors, Femke Vossepoel and Annemarie Muntendam-Bos, for their support, suggestions and feedback. Thanks to our weekly meetings I was able to stay on track and finish my thesis on time.

Further I would also like to thank:

The Plaxis helpdesk and Ronald Brinkgreve for helping me out with software related issues and for providing me a Plaxis licence during my thesis.

All the AES teachers that I had over the past 5 years. For providing me the necessary background knowledge needed for this thesis.

My family, girlfriend and friends for supporting me during my study period.

*Tom Leltz
Delft, June 2024*

Contents

Abstract	i
Preface	ii
1 Introduction	1
2 Seismicity and Geology of the North-East Netherlands	3
2.1 Induced seismicity in the Netherlands	3
2.1.1 Induced seismicity related to Rotliegend reservoirs	4
2.1.2 Induced seismicity related to ZEZ2C reservoirs	6
2.2 Stratigraphy of the North-East Netherlands	7
2.2.1 Description of the Rotliegend Group	7
2.2.2 Description of the Zechstein Group	9
2.2.3 Description of the over- and underburden formations	11
3 Geomechanics	12
3.1 General concepts of geomechanics	12
3.1.1 Stress and strain	12
3.1.2 Elastic deformation and elastic moduli	13
3.2 Mechanisms of induced-seismicity	14
3.2.1 Mohr-Coulomb failure criterion	14
3.2.2 Fault reactivation due to gas production	15
3.2.3 Stress changes around the reservoir	16
3.2.4 Stress changes along the fault	16
3.3 Salt Rheology	17
3.3.1 Salt rheology	17
3.3.2 Rock salt with reservoir depletion	18
4 Modelling in Plaxis	19
4.1 Finite Element Analysis	19
4.2 Model Materials	19
4.2.1 Mohr Coulomb model	20
4.2.2 User-Defined: N2PC-MCT model	21
4.2.3 Discontinuity: Mohr-Coulomb model	22
5 Model set-up	23
5.1 Model Geometry	23
5.1.1 Rotliegend shallow model	23
5.1.2 Carbonate shallow model	24
5.1.3 Carbonate deep model	25
5.1.4 Rotliegend deep model	25
5.1.5 Fault geometry and the model boundaries	26
5.1.6 Elastic vs viscous Zechstein salt	27
5.2 Model set-up in Plaxis	28
5.2.1 Input parameters for the rock materials	28
5.2.2 Input parameters for the fault sections	31
5.2.3 Meshing in Plaxis	32
5.2.4 Phase construction	33
5.3 Output of Plaxis	34
5.3.1 Results in 2D	34
5.3.2 Results in 1D	34

6	Results	36
6.1	2D results around fault zone	36
6.1.1	Deformation	36
6.1.2	Effective stresses and K_0 ratio	42
6.2	1D results along fault	48
6.2.1	Carbonate models	49
6.2.2	Rotliegend models 1/4 offset	50
6.2.3	Rotliegend models 3/4 offset	51
6.2.4	Failure analysis	54
6.3	Summary of results	55
7	Discussion	57
7.1	Result validation	57
7.2	Limitations and assumptions	58
7.2.1	Limitations of software	58
7.2.2	Assumptions	58
8	Conclusion	62
	Bibliography	64
A	Seismicity and Geology of the North-East Netherlands	67
B	Model set-up	69
C	Results	73
D	Discussion	83

1

Introduction

Since the first earthquake related to gas production in 1986, more than two thousand earthquakes have been recorded in the North of the Netherlands, causing significant damage. 38 different gas fields are associated with seismicity (Muntendam-Bos et al., 2022), from which most events are linked to the Groningen gas field. The Groningen gas field is by far the largest gas field in the Netherlands and one of the largest in the world. The largest induced earthquake in the Netherlands occurred in the Groningen gas field with a magnitude M_L of 3.6 in 2012. Induced earthquakes are relatively small (≤ 4.0) compared to natural earthquakes, however due to the shallow depth and soft topsoil the earthquakes can result in a lot of damage (Muntendam-Bos et al., 2022). Infrastructures and buildings have been damaged, with several homes being declared uninhabitable. The damage has recently (April, 2024) led to the permanent closure of the Groningen gas field.

Induced seismicity is limited to the North of the Netherlands, where the gas fields are all overlain by a thick package of the Zechstein formation. The Zechstein formation is characterized by evaporite deposits, consisting of mainly rock salt/halite, which is characterized by a viscous component. It is known that the viscous component influences the state of stress and (a)seismic slip in the underlying depleting reservoir. Some research has been done on the impact of the viscous salt; however, the exact local effects have not been fully investigated and quantified (Orlić & Wassing, 2012; Kettermann et al., 2017; Muntendam-Bos, 2021). It is important to study the impact of the viscous salt on the state of stress and slip, in order to get a better understanding of the origin of the earthquakes.

Even though it is expected that gas production will decline in the future, the energy sector and industry will still be dependent on the use of gas in the upcoming years. Furthermore, understanding the consequences of the viscous property in reservoirs will also contribute to other subsurface projects such as CCS, H₂ storage and geothermal doublets. These projects will also be affected by the characteristics of the viscous behaviour of rock salt, as the Zechstein formation covers most of the Netherlands.

The purpose of this research is to get a better understanding of the influence of the viscous salt on the stress changes and (a)seismic slip. This will be done by answering the following research question and the related subquestions:

- How does the viscous salts in the Zechstein formation influence the state of stress and slip in the Rotliegend and Carbonate gas fields in the North-East of the Netherlands?
 - Does the viscosity of the salt affect the initial stress near a fault in such a manner that stress ratios are being reduced, which allows fault reactivation?
 - How does the viscosity of salt influence the slip behaviour for different fault offsets and different reservoir properties?
 - What is the impact of the depth, in terms of increasing pressure and temperature, on the viscous behaviour (deformation) of the salt and consequently the impact on the stress regime?

In order to answer these questions the finite element software Plaxis 2D will be used. Within Plaxis different geomechanical models will be created, representing the Rotliegend (sandstone) and ZE22C

(carbonate) reservoirs in the Northeast Netherlands. The models will be defined with the help of existing literature on the seismicity and geology in the Northeast Netherlands, as well as on reservoir mechanics and model implementation in Plaxis. After defining the models, reservoir depletion will be modelled using the numerical finite element method, with two different properties for the overlying Zechstein halite. One in which the halite is modelled with elastic properties and one with viscous behaviour, in order to assess the differences in impact on the stress development. The results of the numerical simulations will extensively be analysed, after which a conclusion can be made.

The report will be structured as follows. First of all, some background information is given on the induced seismicity and geology of the North-East Netherlands in Chapter 2. Chapter 3 will provide a theoretical background on geomechanics, in particular related to a depleting reservoir. Information about modelling with the finite element software Plaxis will be given in Chapter 4. The model definition and the assumptions made for the geomechanical model can be found in Chapter 5. Chapter 6 will present the results and the analysis of the results, which is followed by a discussion in Chapter 7. Finally, a conclusion will be made in Chapter 8, with some recommendations for further research.

2

Seismicity and Geology of the North-East Netherlands

The aim of this chapter is to introduce the background information of the Northeast Netherlands, which is needed to get an overview of the induced induced seismicity related to gas production and the (petroleum) geology of the Netherlands and the link between the two. This will later be used in the assessment of defining the models.

First an overview of induced seismicity in the Netherlands is given in Section 2.1, with a focus on the Groningen gas field and the smaller gas fields in the North-East Netherlands. The seismicity will be linked to gas fields and the reservoir units, in order to see which fields can be assigned to seismicity. After which the reservoir units will be studied in detail in Section 2.2 Together with a short stratigraphic overview of the other important formations in the North-East Netherlands, which are needed for the final models.

2.1. Induced seismicity in the Netherlands

An overview of the seismicity in the Netherlands can be found in figure 2.1. The induced events can be linked to several oil and gas fields, however most events occur with gas extraction. Gas fields can primarily be found in the zone where the Rotliegend Slochteren Sandstone is overlain by thick evaporite deposits (Zechstein formation), spreading from England through the Netherlands all the way into Poland. The Zechstein group vanishes to the south of the Netherlands roughly between Amsterdam and Arnhem (Muntendam-Bos, 2021).

An important thing to note is that below this boundary there have not been any recorded seismic events related to the gas fields. These gas fields, in the West Netherlands Basin (WNB), are from the Mesozoic (younger than Permian Zechstein) and hence are not overlain by evaporites. Geomechanical simulations have indicated that a thick salt formation in the subsurface may have a big impact on the occurrences of seismicity (Orlić & Wassing, 2012).

The focus in this project will be on the gas fields in the North-East of the Netherlands (Lauwerssea Trough, Groningen High and Lower Saxony Basin, see abbreviations in Figure 2.1), this excludes the Rotliegend gas fields in the North-Holland Platform (NHP) and Friesland Platform (FP). The gas fields in the North East can be subdivided into Rotliegend gas fields, with the Slochteren Sandstone (SS) as host rock, and in carbonate gas fields, with the Zechstein-2 Carbonate member (shortened to ZE2C in this project) as host rock. Both reservoirs are overlain by a thick rock salt layer.

The Rotliegend reservoirs are located in the Groningen High (GH) and the Lauwerssea Trough (LT), whereas the ZE2C reservoirs are restricted to the Lower Saxony Basin (SLB). The following sections will dive deeper into the seismicity related to the Rotliegend reservoirs (subdivided into the Groningen reservoir and the smaller Rotliegend gas fields in the LT) and the ZE2C reservoirs.

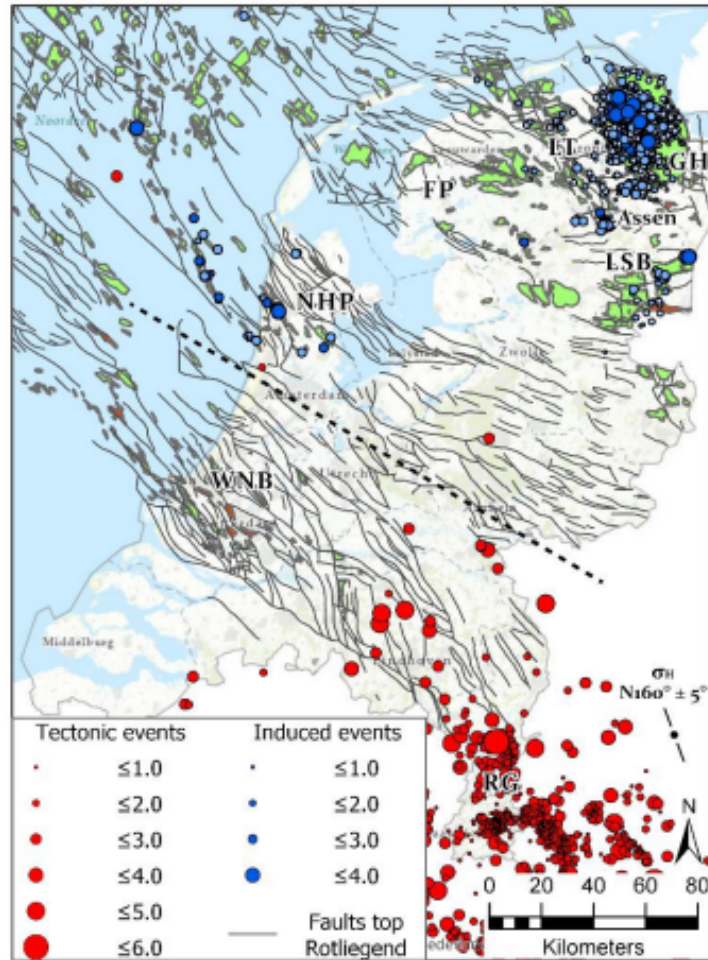


Figure 2.1: Overview of seismicity in the Netherlands. With the Lauwerssea Trough (LT), Groningen High (GH) and Lower Saxony Basin (LSB) in the Northeast Netherlands. (Muntendam-Bos, 2021) For an overview of the extent of these platforms and basins see Figure A.1 in appendix.

2.1.1. Induced seismicity related to Rotliegend reservoirs

Groningen

The largest gas reservoir of the Netherlands is the Groningen reservoir. Gas production has started since the 1960's and the first registered earthquake occurred in December 1991. Ever since, the Groningen reservoir has registered another 1396 earthquakes (until January 2021), with magnitudes up to 3.6 (Muntendam-Bos et al., 2022). As can be seen in figure 2.2, the earthquakes are centred into two "clouds". One big cloud in the centre to NNW and one smaller cloud in the west of the field. The area which has been most effected by the earthquakes is around the city of Loppersum. This city is located just North of the centre of the big "cloud", where the magnitudes have been the largest. This area will later be used as a guidance for determining the geometry of one of the geomechanical models.

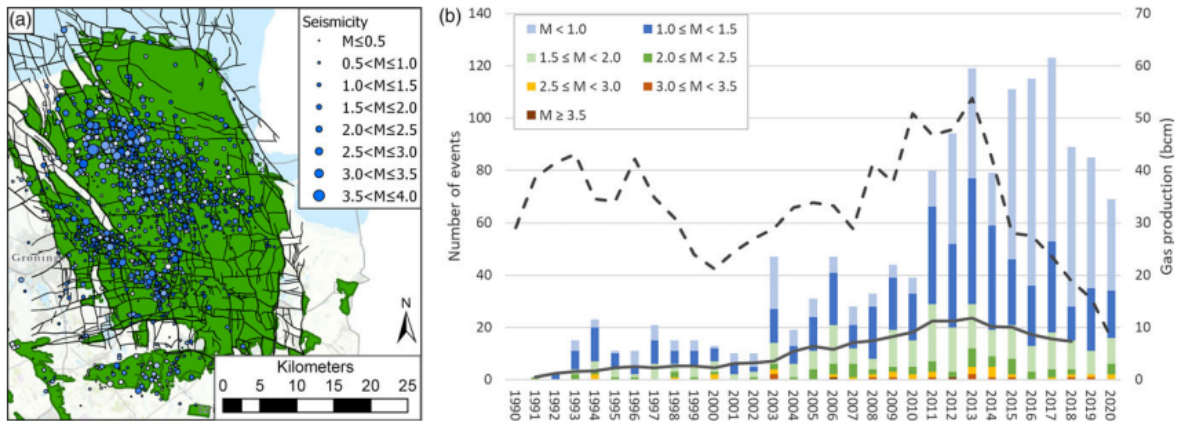


Figure 2.2: An overview of the seismicity in the Groningen gas field in map view (a) and over time (b), together with the gas production over time. (Muntendam-Bos et al., 2022)

Smaller gas fields

The different Rotliegend reservoirs can be found in Figure 2.3. As can be seen apart from the big Groningen field there are a lot of relatively small other fields. These are all more or less aligned in the Lauwerssea Trough. About half of these fields may be associated with seismic events in the past, this can be seen in Figure 2.4. One of these fields registered the first seismic event in the Netherlands in December 1986, with a magnitude of 2.8. This is the Eleveld field, which is the most southern field in the Lauwerssea Trough.

Roholl et al. (2022), has studied the possibility of seismic events in the all gas fields. This study is based on the following indication parameters: the ratio between the drop in pressure and the initial pressure (DP/P_{ini}), the relation between the fault surface and the total rock volume and finally the ratio in Young's modulus (resistance against deformation) between the overburden and the reservoir. This study has concluded that most of the smaller Rotliegend gas fields have a potential risk of seismicity, apart from a few fields in the North, due to the absence of large faults.

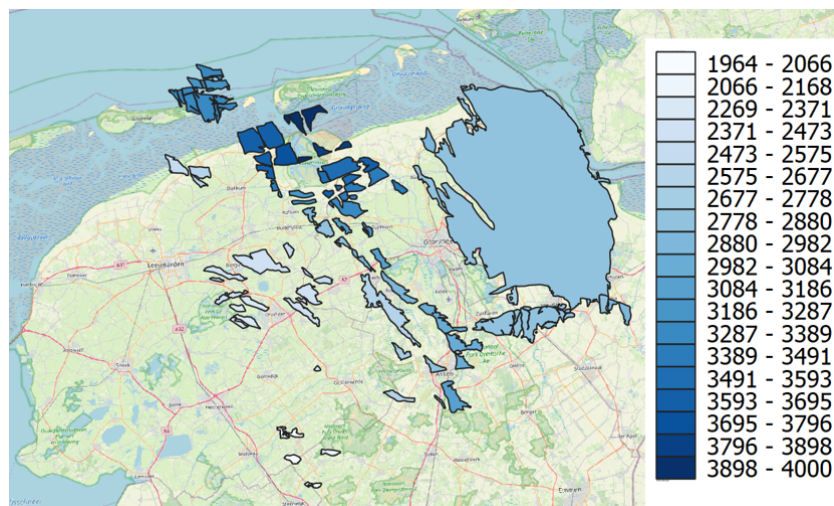


Figure 2.3: The depth of all the onshore Rotliegend Slochteren fields, excluding the fields which are in development. Figure has been made using QGIS, with data from the winningsplannen from www.nlog.nl.

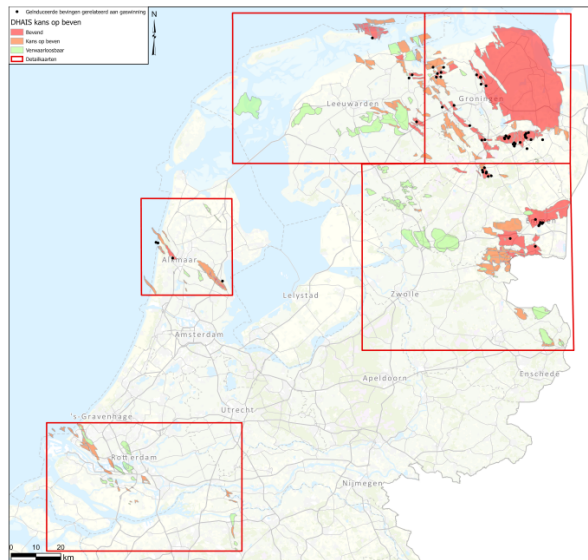


Figure 2.4: Red fields have had events in the past, orange have a possibility of events and green fields have a negligible risk.(Roholl et al., 2022)

2.1.2. Induced seismicity related to ZE22C reservoirs

The ZE22C reservoirs are primarily located in the Southeast of Drenthe (Figure 2.5). The carbonate fields which can be associated with earthquakes are Dalen (total of 3 until 2016), Emmen (11), Emmen-Nieuw Amsterdam (1), Schoonebeek (3) and Coevorden (2) (Van Thienen-Visser et al., 2016). The fields are indicated with the red colour in the bottom right square of Figure 2.4. It is important to note that the earthquakes related to the Coevorden field are registered in the German extension of the field, this also applies to some earthquakes related to the Schoonebeek field.

The first ZE22C reservoir-related earthquake was registered in the Emmen field in October 1991 (Roholl et al., 2022). As can be seen in Figure 2.5, the five fields associated with seismicity are located at depths greater than 2700m. The other fields, which are located significantly shallower (< 2300m), have a negligible risk of seismicity (see Figure 2.4).

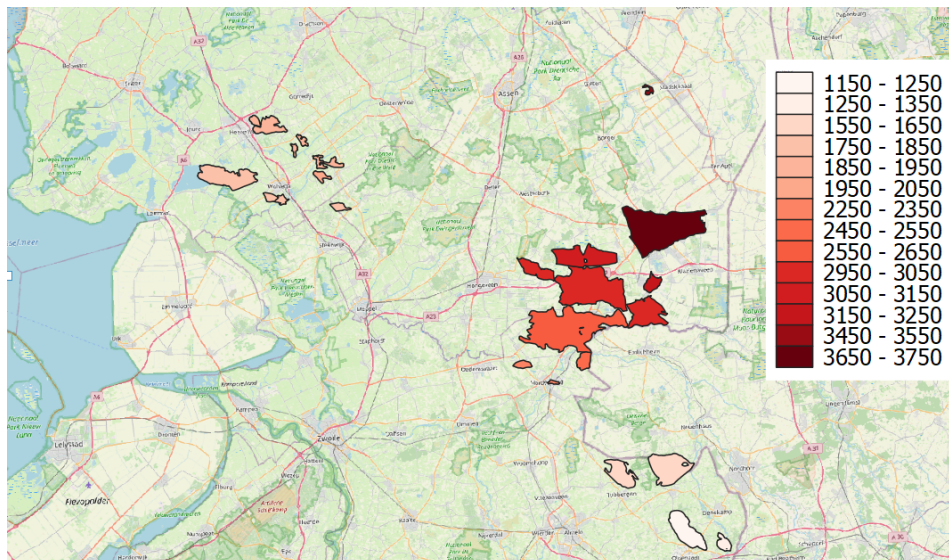


Figure 2.5: The depth of all the onshore Carbonate ZE22C fields, excluding the fields which are in development. Figure has been made using QGIS, with data from the winningsplannen from www.nlog.nl.

2.2. Stratigraphy of the North-East Netherlands

In order to get the final models for the Rotliegend and ZEZ2C reservoirs, the properties of the reservoir rocks and the surrounding layers have to be known and therefore the stratigraphy must be studied. The stratigraphy of the formations and their age will be studied with the help of the stratigraphic nomenclator (see Figure A.2) of Dinoloket (TNO-GDN, 2024).

Figure 2.6, shows in which period of time the onshore Rotliegend and Z2 Carbonate reservoirs can be found. Both are hosted in the Permian, the Rotliegend in the middle Permian and the ZEZ2C in the late Permian. The Rotliegend formation consist of the Slochteren Sandstone and the younger Ten Boer Claystone. Below the Slochteren formation the Carboniferous Limburg group (underburden) can be found. The ZEZ2C is part of the massive evaporite Zechstein formation. A more detailed description of the Rotliegend and Zechstein formation will follow in Sections 2.2.1 and 2.2.2. On top of the Zechstein the following overburden formations can be found from old to young: Triassic lower- and upper Germanic Trias Groups, followed by the Jurassic Altena group, the Cretaceous Rijnland and Chalk group and finally the North Sea group from the Tertiary. These Groups will be described in Section 2.2.3.

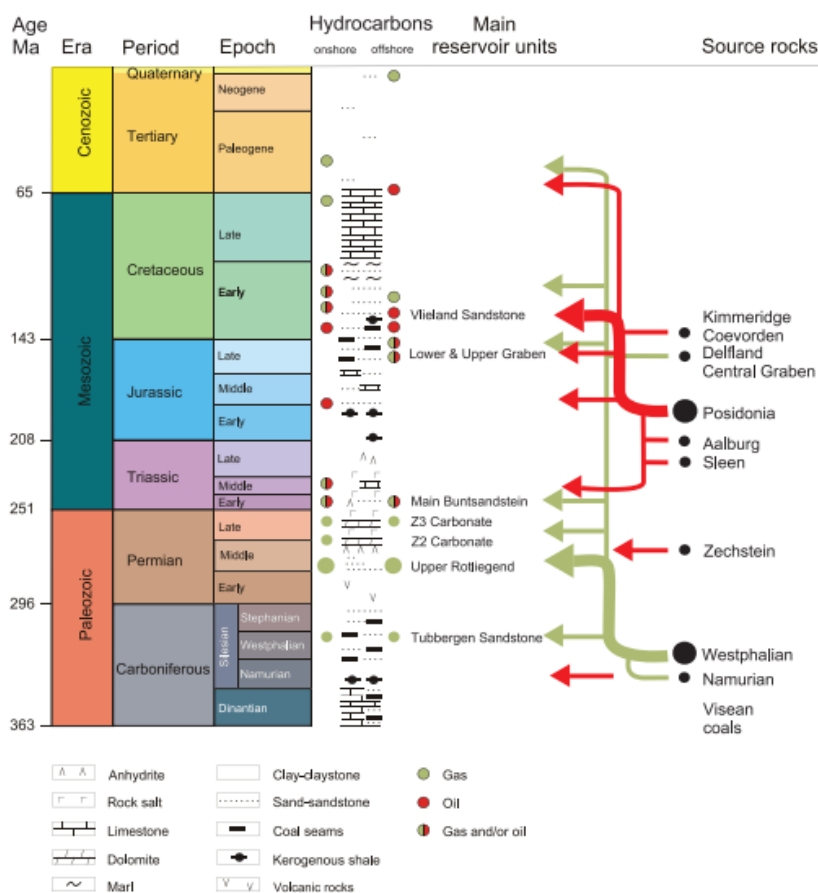


Figure 2.6: Hydrocarbon systems in the Dutch subsurface. Arrows show from which source rocks the main reservoirs have been charged with gas and/or oil. (de Jager & Geluk, 2007)

2.2.1. Description of the Rotliegend Group

The Rotliegend Group can be subdivided into the Slochteren member and the ten Boer member. During the formation of the Rotliegend group, the North of the Netherlands was located in the Southern Permian Basin. There was an high sediment income originated from the Variscan mountains located just south of the Netherlands (van Uijen, 2013). The depositional environment was characterized by fluvial deposits, sheet floods and aeolian dunes. As can be seen in Figure 2.7a, the environment of interest in this project is fluvial. The Slochteren Formation consist of a sequence of conglomerates and course-grained sandstone layers, interbedded with medium- and fine-grained sandstone layers (NLOG, 2024). North of

the current shoreline there was a desert lake. Towards that lake smaller grained material was deposited such as shales and some evaporites. With the rise of the sea level, the Slochteren formation was overlain by the smaller grained siltstones from the North, the ten Boer member (see Figure 2.8a).

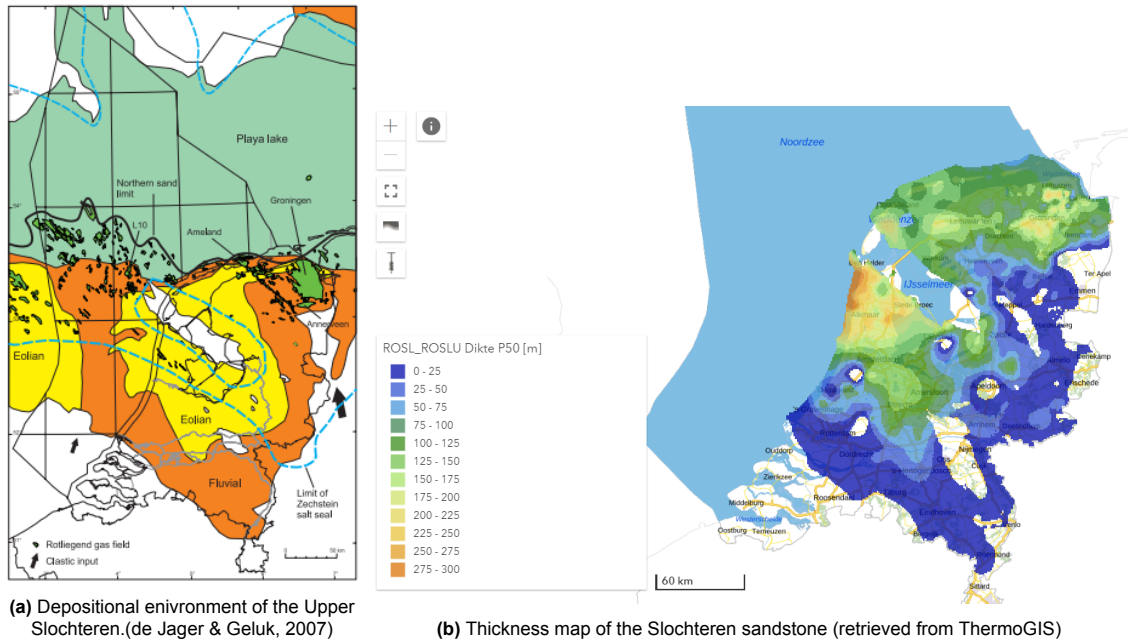


Figure 2.7: Map overview of the Slochteren formation.

The Slochteren Sandstone is the most important host rock for gas reservoirs in the Netherlands. The coarse grained sandstones allow for high porosities and permeabilities. The gas is migrated upwards over time from the underlying Limburg Group and trapped in the Slochteren formation. The overlying finer grained ten Boer formation has significantly lower porosity and permeability. Consequently this member acts as either a seal, some gas has migrated into small sand lenses in the ten Boer layer, however this is relatively limited (see Figure 2.8b). Besides the ten Boer layer faults also function as seal, as well as the Zechstein formation, where the Slochteren sandstone is juxtaposed to the Zechstein.

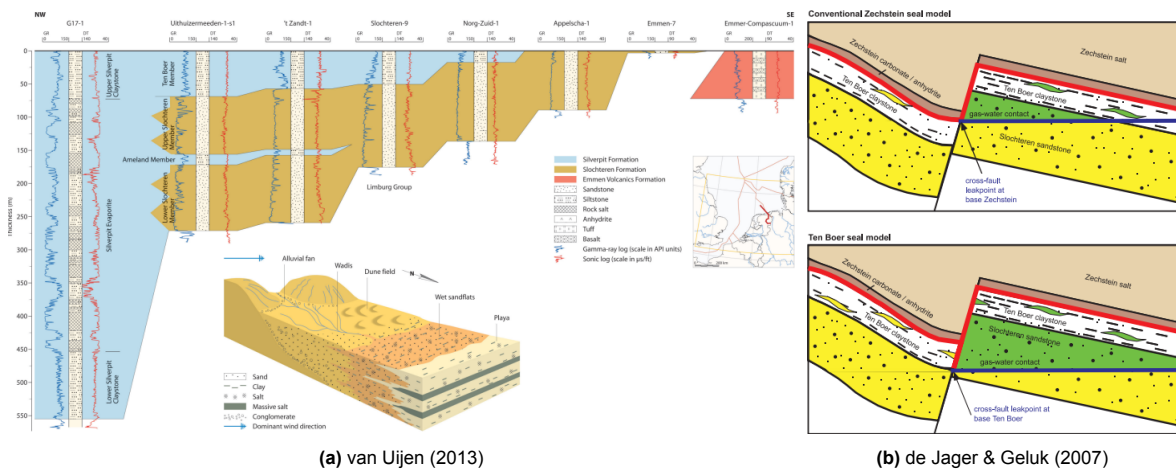


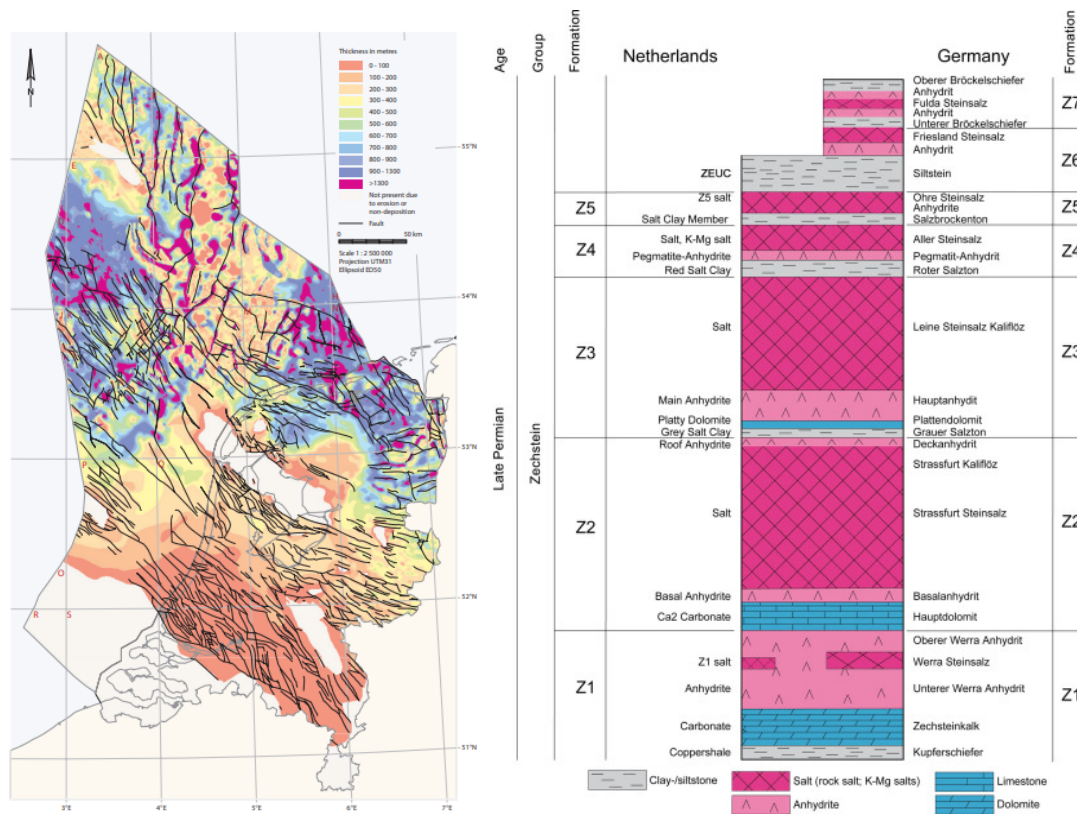
Figure 2.8: Visualisation of the Rotliegend formation, with the depositional environment and the lateral variation of the Slochteren sandstone and the ten Boer member (a) and an illustration of how the gas is trapped in the Slochteren sandstone and the sand lenses in the ten Boer (b).

2.2.2. Description of the Zechstein Group

After the deposition of the Rotliegend formation, an increase in water level, resulted under the prevailing dry climate in an evaporitic environment. This resulted in cyclic evaporite depositions. The cyclicity is controlled by a sea level change due to deglaciation and glaciation and consequently the salinity of the water. With higher sea levels and lower salinity carbonates and or thin shales are deposited. By a decrease in sea level and an increase in salinity the sedimentation changes from carbonate deposition to gypsum precipitation (anhydrite). By further decreasing the sea level the evaporate precipitation changes in nature from gypsum to halite. Giving a full cycle, a new cycle is formed by a sudden sea level rise. (Tolsma, 2014)

In the Netherlands 5 cycles have been characterised within the Zechstein formation. Consisting of the aforementioned shales, carbonates, anhydrites and halite deposits. An overview of the cycles is given in Figure 2.9b. The bottom part (cycle Z1 and beginning of Z2) consist of mainly carbonates and anhydrites (Basal Zechstein unit), whereas when moving upwards the Zechstein formation is dominated by Halite (Rocksalt).

The five cycles resulted in a total Zechstein formation up to 2000m thick (see Figure 2.9a), covering mainly the North of the Netherlands. Outside the Netherlands in Germany and Poland the Zechstein formation can reach up to a thickness of 5500 meters (Peryt et al., 2010). Due to the small density of halite (2.1kg/m³), compared to the overburden layers, the halite can move upwards, locally forming salt domes. The pink patches in Figure 2.9a, can be identified as salt domes.



(a) Thickness distribution of the Zechstein formation (Duin et al., 2006). (b) Overview of the Zechstein cycles in the Netherlands and Germany. (Strozyk et al., 2017).

Figure 2.9: Combined figure showing (a) thickness distribution of the Zechstein formation and (b) overview of the Zechstein cycles.

In this project the Zechstein group will be subdivided into 4 different layers (similar to Buijze et al. (2017)). The bottom layer will consist of the Z1 formation, in which the anhydrite is dominant. The next layer will be the ZE22 Carbonate layer, which will be the reservoir layer for the carbonate fields. This layer will be followed by the sealing ZE22 Basal Anhydrite (ZE22A). These three layers are the non-mobile rock units of the Zechstein Group, these units are formed prior to the deposition of the

first thick and ductile Zechstein salt (ZEZ2H). The ductile Zechstein salt forms the last Zechstein layer and includes the halite layer from the second cycle and the deposits of all the other cycles, as they are mainly characterised by halite.

The ZEZ2 Carbonate layer is the reservoir layer for the carbonate reservoirs. Generally, evaporites are characterized by a very low or absence of porosity (good seal for the Rotliegend reservoir). The porosity and permeability of halite for example is almost zero. The porosity of the Carbonate matrix is also relatively low, however the gas reservoirs in the SE of Drenthe do have a carbonate layer as reservoir rock. The porosity and permeability of the ZEZ2C reservoir is mainly originated from the presence of fractures. When looking at Figure 2.10 it can be concluded that the ZEZ2C is being deposited from north to south on a platform, slope and in the basin. The slope deposits consist of the largest fractures with dm-m size and the smallest spacing. In other words the fracture density is the highest on the slope, resulting in a relatively high permeability. When looking at the map view it can be seen that the gas reservoirs in the Southeast of Drenthe are exactly located within the depositional slope environment. At the slope the ZEZ2C layer is the thickest and thins out towards the basin (North) and the platform (South).

With the deposition of the ZEZ2 Halite the sea level has dropped to platform level, consequently the halite precipitation was mainly restricted to the basin and slope areas, filling almost the entire basin in the North of the Netherlands (Paulides, 2016). Resulting in very thick halite layers covering the Rotliegend reservoirs in the North and a thinner halite layer covering the Carbonate reservoirs in the South. However, a significantly thick layer is present at both locations.

The ZEZ2A layer has a relative constant lateral thickness, slightly thicker above the Carbonate reservoir than the Rotliegend reservoirs.

For the Z1 cycle the sea level was higher, giving a shoreline more to the south. This resulted in thinner deposits at the Carbonate and Rotliegend reservoirs locations compared to the ZEZ2 deposits. Especially the ZEZ1 Carbonate layer is thin (<10m) in the areas of interest and therefore the layer is combined with the ZEZ1 Anhydrite layer which is significantly thicker (up to 60m above the Carbonate reservoirs). Towards the south the ZEZ1 layers become thicker, however, that is outside of the area of interest.

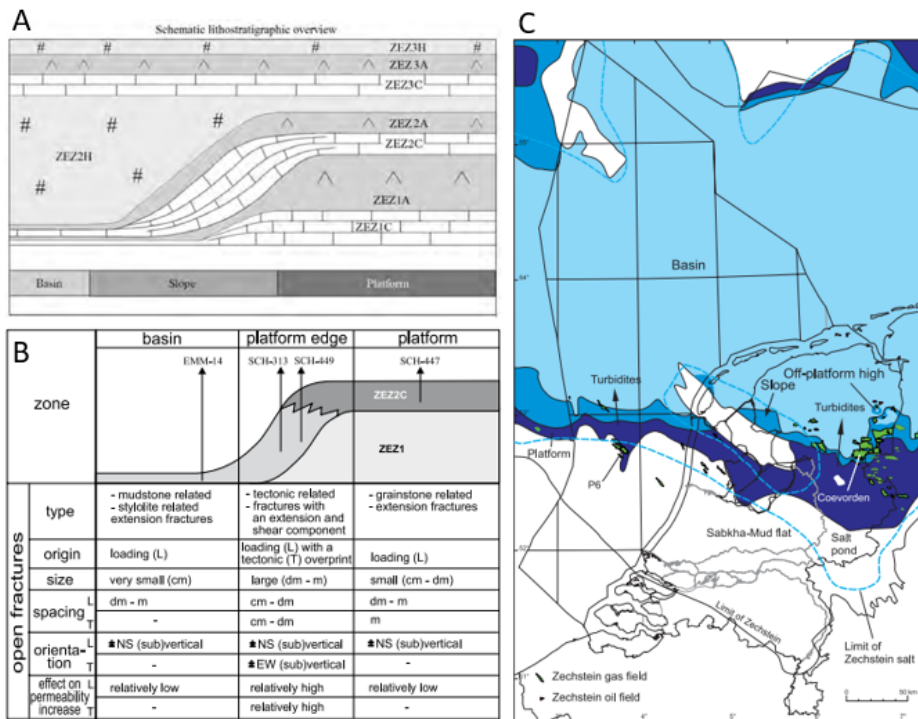


Figure 2.10: ZEZ2C: A) the lateral variation of the ZEZ1 and ZEZ2 formations (Reijers, 2012). B) The characteristics of the ZEZ2C per environment (Reijers, 2012). C) Map overview of the ZEZ2C depositional environment (de Jager & Geluk, 2007).

2.2.3. Description of the over- and underburden formations

Now that the reservoirs formations are described, the over- and underburden formations will be discussed as they are also included within the geomechanical model, a short description of the formations is given. The descriptions follow the lithological descriptions from Dinoloket (TNO-GDN, 2024).

Figure 2.11, gives a cross section of the subsurface (up to 6000m depth) from the North (Lauwerssea Trough) of the study area to the south (Lower Saxony Basin) of the study area. The cross sections show the important formations that will be used in the model, the formations are already mentioned in the introduction of Section 2.2.

In the model there will be one underburden layer, the Limburg Group (grey). This layer is deposited during the the Carboniferous and is overlain by the Rotliegend formation in the North and the Zechstein Group in the South of the North east Netherlands. The Limburg Group consist of mostly grey to black, fine-grained siliclastic sediments. Coal layers can be found in the middle and upper part of the formation. These coal layers are also the source rock for the gas in the overlying reservoirs.

The overburden consist of multiple groups, as described in the introduction of this Section (2.2). The Lower- and Upper Germanic Trias Groups (Pink) will be combined into one layer in the model. Both the lower and upper group consist of a high variety of rocks including: sandstones, siltstones, claystones and evaporites, the (silty) claystones are dominant. The evaporites are found in the Röt formation in the lower part of the Upper Germanic Trias group and is similar to the Zechstein group. Because the Röt formation is relatively thin compared to the whole Trias Group, this formation will not be included as a separate layer in the model. The thickness of Triassic varies from about 500 meters in the north to 1000m in the south. The next layer that will be used consist of the Altena Group and the Weiteveen formation deposited in the Jurassic. These formations are only present in the south of the study area, where the Carbonate reservoirs are located. Similar to the Triassic formations the Jurassic formations consist of mainly claystones.

The Cretaceous layer consist of the upper Cretaceous Chalk Group and the lower Cretaceous Rijnland Group (green). The Cretaceous rocks are dominated by carbonate rocks (Chalk group). Due to the deep burial, the Chalks were compacted and formed dense limestones. The lower Cretaceous Rijnland Group is significantly thinner then the Chalk Group and consist of clastic deposits similar to the Jurassic and Triassic rocks. The thickness of the Cretaceous is more or less similar throughout the study area (except for the location of the salt dome).

Finally the upper layer consist of the North Sea groups (yellow and red), which will be combined into a Tertiary (age: Paleogene and Neogene) layer. The North Sea Groups consist of (shallow) marine deposits, in which mainly clays can be found in the North of the Netherlands. The layer can reach thicknesses up to a 1000m in the North of the study area.

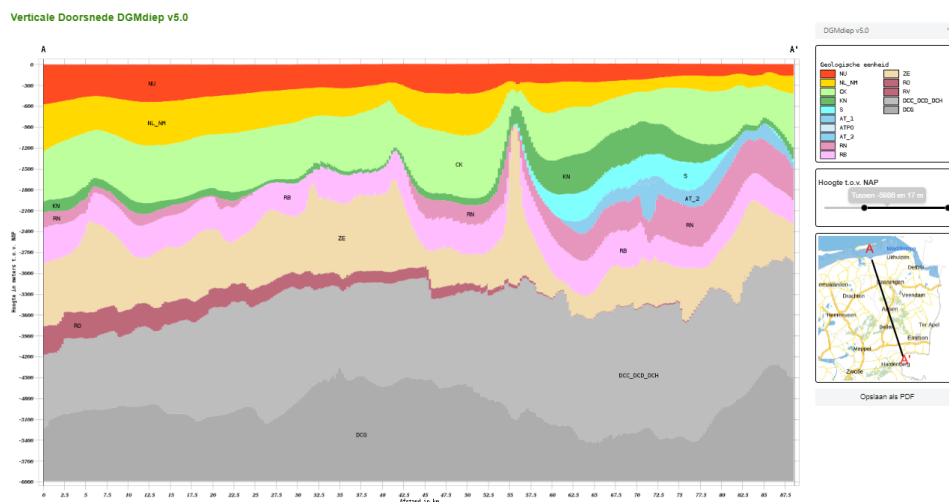


Figure 2.11: Cross section of the subsurface from the most northern onshore Rotliegend gasfields to the Carbonate gas fields in South-East Drenthe. (taken from Dinoloket) Grey: DC Limburg Group (Carboniferous), Red-Brown: Rotliegend (Permian), Light-Yellow: Zechstein (Permian), Pink: Lower Germanic Trias Group (Triassic) and dark pink: upper Germanic Trias group (Triassic), Blue: Altena Group (Jurassic), Dark green: Rijnland group (Cretaceous) and light Green: Chalk group (Cretaceous) and yellow: lower North Sea Group (Paleogene) and red: Upper North Sea Group (Neogene).

3

Geomechanics

In this chapter the basic principles of geomechanics are explained. This will help to understand the reason behind stress changes and deformations in the subsurface as well as the origin of seismicity. First the general concepts of geomechanics are covered in Section 3.1, explaining stress, strain and the elastic parameters. After which, the stress changes in depleted gas reservoirs are explained and how faults are reactivated. Finally, the behaviour of rock salt will be covered.

3.1. General concepts of geomechanics

3.1.1. Stress and strain

With the presence of overburden weight and the movement related to plate tectonics, subsurface rocks are subjected to forces. In geomechanics stress is used to express the forces that are acting on a rock. Stress (σ) is simply defined by the force (F) divided by the area (A) on which the force is acting:

$$\sigma = \frac{F}{A} \quad (3.1)$$

The SI unit for stress is Pascal ($\text{Pa} = \text{N}/\text{m}^2$). In this project, the stresses will reach values in the order of $10^6 - 10^8 \text{Pa}$, which is equivalent to $1 - 100 \text{MPa}$.

An important aspect to take into consideration is the direction of the force relative to the area on which it is acting. If the force is not acting normal to the surface, the force can be decomposed into a normal component and a shear component, this is shown in figure 3.1a (Fjær et al., 2008b). The shear component is called the shear force and is acting parallel to the surface. The corresponding shear stress is given by $\tau = F_s/A$, whereas the normal stress is given by $\sigma_n = F_n/A$.

In 3d this gives a normal stress in all 3 directions, as well as shear stresses along all the planes in the 3 dimensions. This can be seen in Figure 3.1b, all the stresses are summarized with the stress tensor, with the normal stresses on the diagonal and shear stress outside of the diagonal:

$$\sigma = \begin{pmatrix} \sigma_{11} & \sigma_{12} & \sigma_{13} \\ \sigma_{21} & \sigma_{22} & \sigma_{23} \\ \sigma_{31} & \sigma_{32} & \sigma_{33} \end{pmatrix} = \begin{pmatrix} \sigma_{11} & \tau_{12} & \tau_{13} \\ \tau_{21} & \sigma_{22} & \tau_{23} \\ \tau_{31} & \tau_{32} & \sigma_{33} \end{pmatrix} \quad (3.2)$$

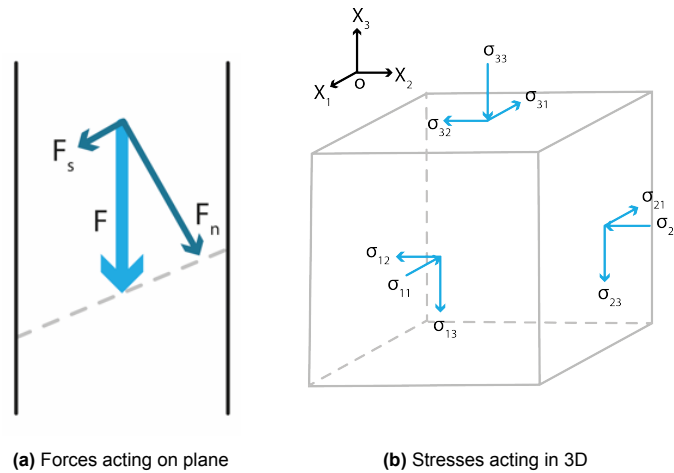


Figure 3.1: Overview of normal and shear stresses.

Rocks subjected to a particular stress can deform, this deformation is indicated by the term strain. Strain is defined by the difference between the initial and final length divided by the initial length:

$$\varepsilon = \frac{\Delta L}{L} \tag{3.3}$$

There exists two kinds of strain: simple strain and shear strain. Simple or elongated strain is the strain which occurs due to a normal stress. The deformation can be characterised by compaction or extension. With an uniaxial stress acting on a rock, the rock compresses in the direction of the stress, but it extends in the other directions (see Figure 3.2d). The ratio between the strain perpendicular to the stress divided by the strain perpendicular to the stress is called the Poisson ratio ($\nu = \varepsilon_x / \varepsilon_z$). The larger the Poisson ratio, the larger the deformation in the horizontal direction with deformation in the vertical direction.

Shear strain is the strain caused by shear stress, this causes a change in shape. The different kind of strain deformations are given in Figure 3.2.

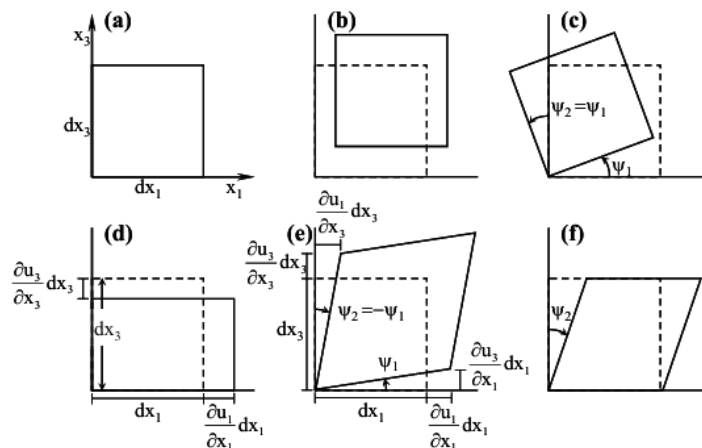


Figure 3.2: Examples of different types of deformation and strain: (a) Undeformed; (b) Translation; (c) Rotation; (d) Normal strain; (e) Pure shear strain; (f) simple shear strain. (Mulders, 2003)

3.1.2. Elastic deformation and elastic moduli

For a rock in general, the stress can be plotted against the strain, giving a curve similar to the curves in Figure 3.3. A rock has the ability to recover from it's deformation, this is defined as the elasticity (Fjær

et al., 2008b). Within the elastic region the rock will return to its initial volume and shape if the stress is released, this region is given by the red curve in the figure. If the stress reaches the yield stress, the strain becomes permanent. The rock does not return to its initial shape after stress release, however, the elastic part can still be reversed (Figure 3.3). The next section (3.2.1), will discuss the transition from elastic to plastic behaviour.

The gradient of the elastic curve can be described by Hooke's law. Hooke's law describes a material's resistance against deformation and can be defined by the relation between the stress and the strain:

$$E = \frac{\sigma}{\varepsilon} \quad (3.4)$$

In which E is the Young's Modulus. The larger the Young's Modulus the steeper the elastic curve becomes and the more stress is needed to deform a rock. Similar to the Young's Modulus the resistance against shear strain can also be described. This is given by the Shear Modulus (G), which is the relation between the shear stress and the shear strain. The relation between the Young's and Shear Moduli can be expressed using the Poisson's ratio $G = \frac{E}{2(1+\nu)}$.

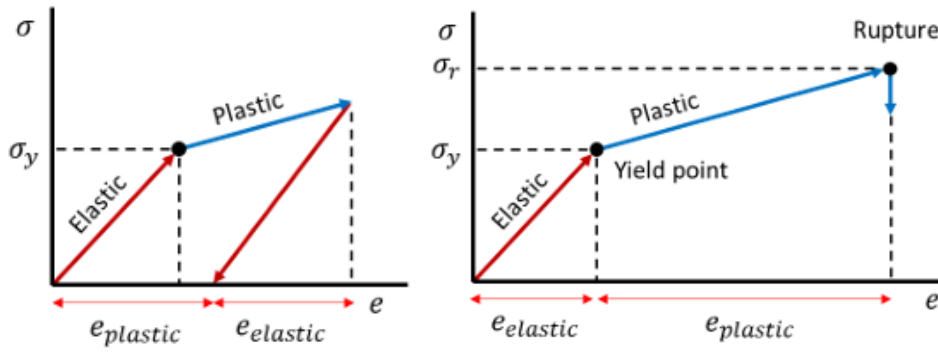


Figure 3.3: Stress-strain curve for elastic and plastic deformation. (Fossen, 2016)

3.2. Mechanisms of induced-seismicity

With the depletion of a reservoir, the pore pressure is being reduced, this causes stress changes, which can eventually lead to fault reactivation.

3.2.1. Mohr-Coulomb failure criterion

A fault will reactive if failure/slip occurs and deformation/strain becomes plastic. Rock failure can be described by a certain failure criterion ($\tau = f(\sigma'_n)$). The Mohr-Coulomb failure criterion is the most common failure criterion and is described by the following equation:

$$\tau = C_0 + \sigma'_n \tan(\phi) = C_0 + \sigma'_n \mu \quad (3.5)$$

In which C_0 is the cohesion, μ the friction coefficient and ϕ the angle of friction. These are specific rock parameters, defining the strength of the rock.

The Mohr-Coulomb failure criterion for a rock is illustrated by the linear line in Figure 3.4. The circle which is plotted, corresponds to the smallest (σ_3) and largest (σ_1) principal stress. If the circle touches the failure criterion, a fracture will develop with a dip = β . For an existing fault plane, with a particular σ_1 and σ_3 acting on the plane, a point is located in the shaded area of Figure 3.4b. If the smallest and largest principal stresses are directed perpendicular to the strike of the fault plane, the effective normal and shear stresses can be calculated (and thus the location of the fault plane in the circle can be determined) (σ_3 and σ_1) by the following equations:

$$\sigma'_n = \frac{1}{2}(\sigma'_1 + \sigma'_3) + \frac{1}{2}(\sigma'_1 - \sigma'_3) \cos 2\beta \quad (3.6)$$

$$\tau = \frac{1}{2}(\sigma'_1 - \sigma'_3)\sin 2\beta \tag{3.7}$$

In which β equals the dip of the fault.

The strength properties of a fault are characterized by a smaller cohesion compared to the surrounding rock, usually the cohesion is assumed to be zero. This will bring the failure criteria line down, closer to failure. If the fault plane in the Mohr circle touches the failure line of the fault, the fault will be reactivated and (a) seismic slip will occur.

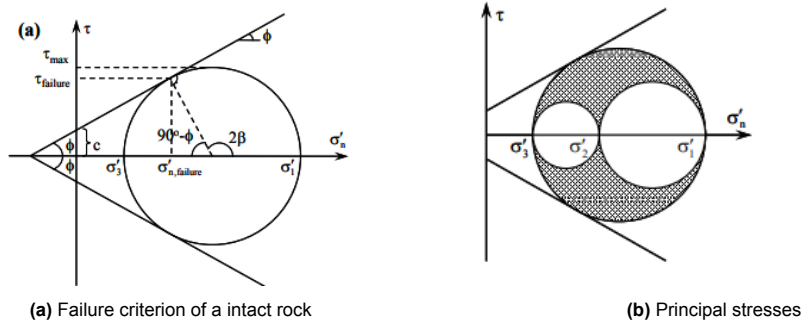


Figure 3.4: Mohr-Coulomb failure criterion. (Zbinden et al., 2017)

3.2.2. Fault reactivation due to gas production

In a normal faulting regime, σ_3 is considered to be horizontal and σ_1 vertical. With reservoir depletion the pore pressure is being reduced. According to the effective stress equation $\sigma' = \sigma - \alpha P_p$, this will increase the effective stress for both σ_v and σ_h and shift the Mohr circles with the fault plane away from the failure criteria. However, due to mainly vertical compaction, poroelasticity takes place. Resulting in a larger increase in effective vertical stress than effective horizontal stress. The change in effective horizontal stress can be described by $\Delta\sigma'_h = -\alpha(\nu/(1-\nu))\Delta P$. Where α is the Biot-Willis coefficient and ν the Poisson's ratio. The vertical stress change is described by $\Delta\sigma'_v = -\alpha\Delta P$. As the difference between the vertical and horizontal effective stress increases with depletion, the Mohr circle also increases, approaching the failure line. This can be seen in Figure 3.5.

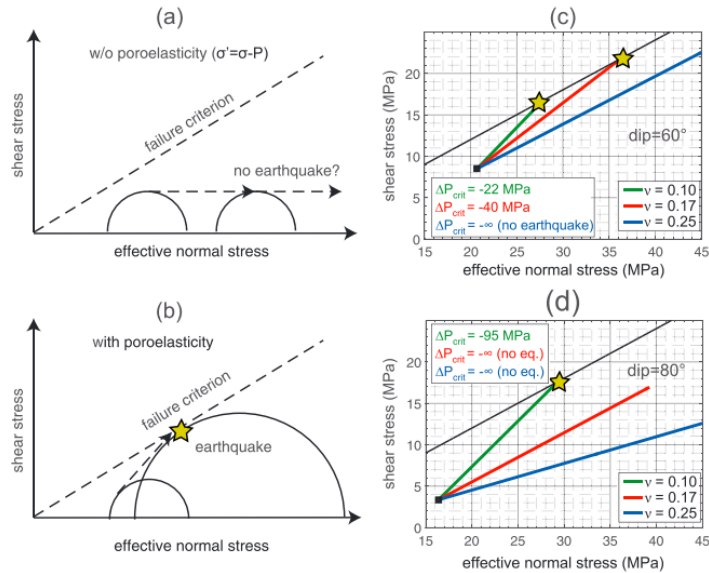


Figure 3.5: Theory of poroelasticity described by the Mohr-Coulomb failure criterion.. (Zbinden et al., 2017)

The ratio between the effective horizontal stress and effective vertical stress is described by the follow-

ing equation:

$$K_0 = \frac{\sigma'_x}{\sigma'_y} \quad (3.8)$$

The smaller the ratio, the larger the difference in stress and the bigger the Mohr circle. A larger Mohr circle means a higher risk of reaching the failure criterion. For smaller values of ν , the smaller the stress ratio will be and the larger the risk of failure, this can also be seen in Figure 3.5c/d. After a fault reactivates, the fault's strength is being reduced, giving a decrease in friction coefficient. The initial friction coefficient is called the static friction coefficient μ_s and the coefficient after failure is the dynamic friction coefficient μ_d .

3.2.3. Stress changes around the reservoir

With depletion, the change in stress is not limited to the reservoir. Due to volume reduction of the reservoir rock, horizontal stresses are decreased juxtaposed to the reservoir. On the other hand, the vertical stress is increased next to the reservoir. Consequently, the K_0 ratio is decreased, resulting in a larger potential of normal faulting (failure). On top of the reservoir the lateral shrinking causes an increase in horizontal stress, on the contrary the vertical stress is being decreased due to the compaction below. This gives a larger K_0 ratio above the reservoir and a smaller risk of failure. These stress changes can be seen in Figure 3.6 (Buijze et al., 2017)

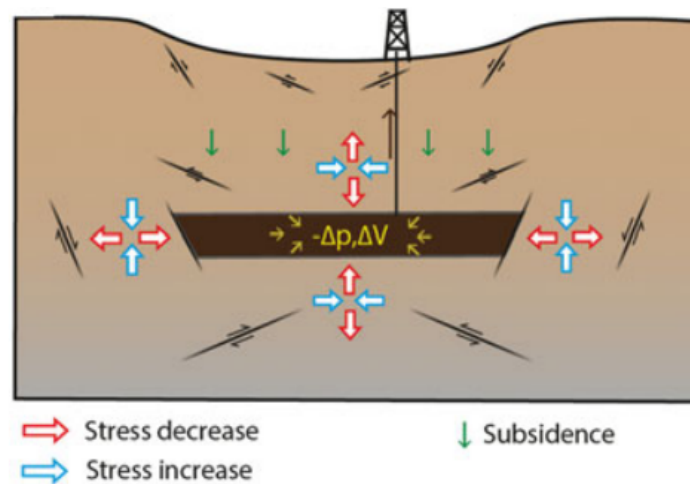


Figure 3.6: Stresses changes outside of a depleting reservoir (Buijze et al., 2017).

3.2.4. Stress changes along the fault

How the effective normal stress and shear stress changes with depletion can be found in Figure 3.7. As can be seen both the effective normal and shear stress (like the horizontal and vertical stress) increase with depletion in the reservoir. The locations with the largest increase are the boundaries where the reservoir is no longer juxtaposed to itself. This is the area where failure is most likely to occur. Above and below the reservoir, the shear stress is decreasing (in agreement with the decreasing vertical stress) to a positive stress. A positive shear stress means the tendency to reverse faulting. van den Bogert (2018) and Buijze et al. (2017) have studied the impact of the offset on the slip. They came to the conclusion that with a larger offset a smaller pressure depletion is needed to have reactivate the fault. This means that the juxtaposition interval in Figure 3.7 becomes smaller and the boundary peaks are moved towards each other. According to van den Bogert (2018), slip occurs with the smallest pressure decrease when the offset is exactly one reservoir thickness.

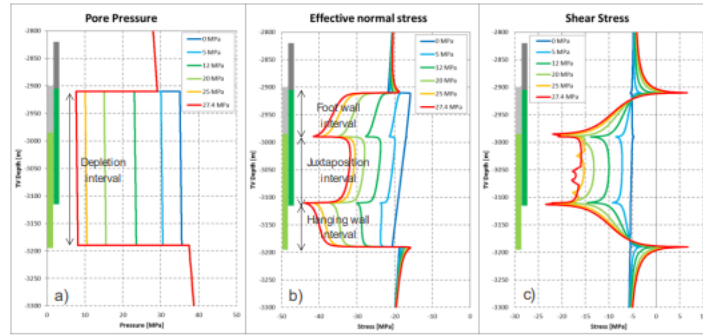


Figure 3.7: Stresses along the fault for a depleting reservoir. (van den Bogert, 2018)

3.3. Salt Rheology

3.3.1. Salt rheology

In order to understand the stress changes due to the visco-elastic salt, the behaviour of the salt must be known. In contrast to other rocks, rock salt is viscous and has a time dependent deformation property (creep). Creep occurs at slow strain rates and can be characterised as ductile behaviour. The slow strain mechanisms occurring in rock salt are defined as dislocation creep, pressure-solution creep and plasticity or micro-cracking (Figure 3.8). The mechanisms are influenced by a number of factors such as stress, fluid content, grain size, grain boundary structure and temperature Kettermann et al. (2017).

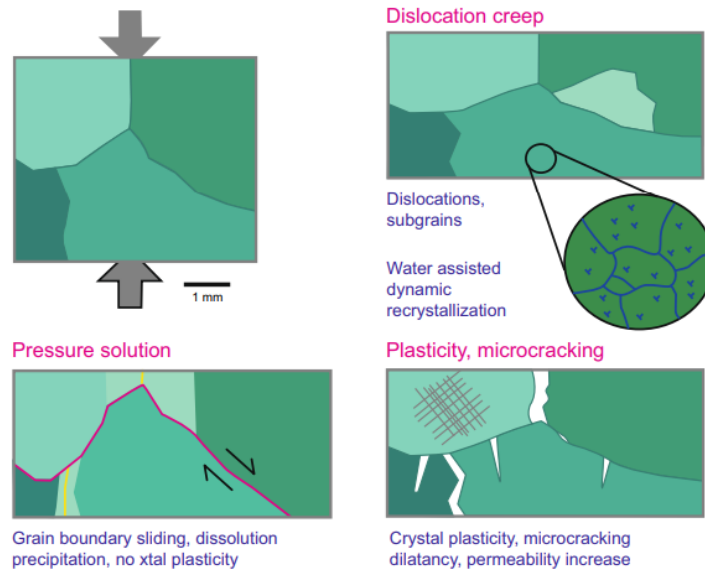


Figure 3.8: Deformation mechanisms of rock salt at 20-200 °C. (Li & Urai, 2016)

Rock salt rheology in the subsurface is mainly dominated by the dislocation creep and pressure-solution creep. Dislocation creep is dominant under high differential stress and can be described by non-Newtonian power law creep. On the other hand pressure solution creep is more dominant at lower stresses and behaves according to the Newtonian flow law. The strain through creep for the mechanisms is given by the following equations (Li et al., 2012; Li & Urai, 2016; Kettermann et al., 2017):

$$\dot{\epsilon}_{DC} = A(\sigma)^n = A_0 \exp\left(-\frac{Q_{DC}}{RT}\right) (\sigma_1 - \sigma_3)^n \quad (3.9)$$

$$\dot{\epsilon}_{PS} = B(\sigma) = B_0 \exp\left(-\frac{Q_{PS}}{RT}\right) \left(\frac{\sigma_1 - \sigma_3}{TD^m}\right)^n \quad (3.10)$$

Where A_0 and B_0 are material parameters, Q activation energy, R gas constant, T temperature, D grain size and n and m are stress and grain-size exponents.

The difference between the two mechanisms is the non-Newtonian ($n>1$) vs Newtonian behaviour ($n=1$). Another difference is that dislocation creep is mainly dependent on the differential stress, whereas pressure solution creep is mainly dependent on grain size, which can be seen in the formulas. If the two processes occur simultaneously, the strain is given by the sum of the two strain rates:

$$\dot{\epsilon} = \dot{\epsilon}_{DC} + \dot{\epsilon}_{PS} \quad (3.11)$$

3.3.2. Rock salt with reservoir depletion

There has already been some research to the influence of halite with a viscous property near a fault in a depleting reservoir.

The isotropic stress state in the salt cause an increase in the stress ratio in the underlying formations. The thicker the Zechstein formation, the larger the stress ratio, giving high stress ratios for the North-Eastern gas reservoirs (Muntendam-Bos, 2021).

It has been concluded that with a rock salt caprock (modelled directly above the reservoir), the initial state of stress differs from when there is an elastic caprock. The high horizontal stresses in the rock salt reduce the initial horizontal stresses and K_0 ratio near the fault. Resulting in a larger risk of fault reactivation (Orlić & Wassing, 2012; Muntendam-Bos, 2021). However, the exact local effects have not been quantified and investigated. This will be done in this study.

The high horizontal stresses can also dilate a fault, causing a salt flow downwards along the fault (Kettermann et al., 2017). After the salt has intruded the fault the dilation is further amplified, causing an extra decrease in horizontal stress. Unfortunately, salt intrusion will not be covered in this study due to software limitations.

4

Modelling in Plaxis

In this chapter the theory behind the models and calculations that are used in Plaxis are explained. This is needed to understand how the deformations and stresses are calculated. It can also help to understand how rock behaviour is being approached with the used model, to explain limitations and possible errors. First the general basics of the Finite element method are explained and the steps needed for a finite element analysis. After which the implementation behind the material models are covered.

4.1. Finite Element Analysis

Plaxis is a finite element software for 2D analysis of deformation and stability in geotechnical engineering and rock mechanics. In this project the finite element method in Plaxis will be used for geomechanical simulations. The finite element method (FEM), solves partial differential equations (PDE) that describe the physical behaviour, such as heat transfer, fluid dynamics and rock deformation (Dhatt et al., 2013). The biggest advantage of the finite element method compared to other numerical methods for solving PDE's (such as finite difference method (FDM) is that it can deal with complex structures, such as salt domes or like in this projects faults. Most studies that study fault behaviour with geomechanical models use finite element software, such as DIANA (Buijze, 2020; Lele et al., 2015; van den Bogert, 2018; Baisch et al., 2023).

In order to do the finite element analysis in Plaxis a few steps have to be taken. The first step is to create a model geometry, assign properties to the materials and determine the equations that want to be solved. The equations related to the material models will be discussed in the following sections. After this step, the geometry is divided into separate elements of finite dimension, therefore the name finite element. All the elements together are called the mesh. The finer the mesh the more accurate the results are, but the larger the computational intensity. The resolution of the mesh can be set separately for different locations. In Plaxis 2D the elements are triangularly shaped and consist of either 6 or 15 nodes.

The next step is done in the calculation phase in Plaxis and consist of the finite element calculations, including the evaluation of the stiffness matrix, applying the boundary conditions and solving the system of equations (OpenLearn, 2019). The basic equations for this step can be found in the Plaxis scientific manual (Plaxis, 2023c). After analysing the results it can be decided to refine the mesh or to make other adaptations to the model.

4.2. Model Materials

Plaxis contains four models specifically suitable for modelling rock type behaviour. These include the Linear Elastic, Mohr-Coulomb, Jointed Rock and Hoek-Brown models. The Jointed Rock model is not applicable for this project as it needs multiple elastic moduli for one layer to model anisotropic behaviour, which is too complex for this study. The Hoek-Brown model is not suitable for stratified or jointed rock sections, as it is designed to model weathered rocks. This leaves the Linear Elastic and

Mohr Coulomb model. The Linear Elastic model only models the elastic deformation of the materials and does not include failure and plastic behaviour. The Mohr-Coulomb model uses the Linear Elastic model, with the failure and plastic behaviour. Therefore it is chosen to use the Mohr-Coulomb model for the rock materials. This model is used for all the layers, however, the Halite layer is also being simulated with the viscous property. For this case the User-Defined N2PC-MCT model is used. Finally, the fault sections are also modelled with a specific model, which also is the Mohr Coulomb model, but then for discontinuities.

4.2.1. Mohr Coulomb model

This section is based on the Plaxis materials manual (Plaxis, 2023a). The Mohr Coulomb model is a linear elastic perfectly plastic model. The deformation of the model is characterized by an elastic part and plastic part:

$$\varepsilon = \varepsilon^e + \varepsilon^p \quad (4.1)$$

The elastic part is modelled using Hooke's law, in which the strain is calculated from the stress and the Young's modulus as explained in Section 3.1.2. The strain of the elastic part can be seen in Figure 4.1, which is similar to the elastic curve in Figure 3.3. The plastic part is defined by the Mohr-Coulomb failure criterion, similar to the theory described in Section 3.2.1. If the failure line has been reached, the rock becomes plastic. With perfectly plastic behaviour, the stress does not increase for an increasing strain, this is also known as no hardening or softening behaviour.

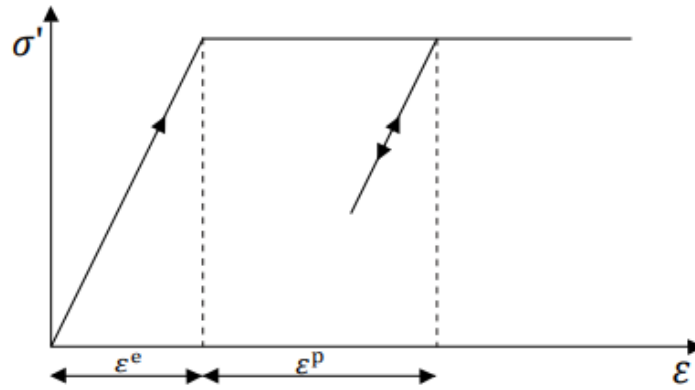


Figure 4.1: Basic idea of an elastic perfectly plastic model (Plaxis, 2023a).

The Mohr-Coulomb model has been implemented in Plaxis using yield functions. These functions are based on the principal stresses and follow the following equations:

$$f_{1a} = \frac{1}{2} (\sigma'_2 - \sigma'_3) + (\sigma'_2 + \sigma'_3) \sin(\varphi) - C \cos(\varphi) \leq 0 \quad (4.2)$$

$$f_{1b} = \frac{1}{2} (\sigma'_3 - \sigma'_2) + (\sigma'_3 + \sigma'_2) \sin(\varphi) - C \cos(\varphi) \leq 0 \quad (4.3)$$

$$f_{2a} = \frac{1}{2} (\sigma'_3 - \sigma'_1) + (\sigma'_3 + \sigma'_1) \sin(\varphi) - C \cos(\varphi) \leq 0 \quad (4.4)$$

$$f_{2b} = \frac{1}{2} (\sigma'_1 - \sigma'_3) + (\sigma'_1 + \sigma'_3) \sin(\varphi) - C \cos(\varphi) \leq 0 \quad (4.5)$$

$$f_{3a} = \frac{1}{2} (\sigma'_1 - \sigma'_2) + (\sigma'_1 + \sigma'_2) \sin(\varphi) - C \cos(\varphi) \leq 0 \quad (4.6)$$

$$f_{3b} = \frac{1}{2} (\sigma'_2 - \sigma'_1) + (\sigma'_2 + \sigma'_1) \sin(\varphi) - C \cos(\varphi) \leq 0 \quad (4.7)$$

In which φ equals the friction angle ($\tan^{-1}(\mu)$) and C the cohesion.

The equations follow from a combination of Equations 3.5, 3.6 and 3.7. These yield functions are visualized in 3D in Figure 4.2. Points that are within the yield surfaces behave elastically, following

Hooke's law. Points that are at the yield surfaces behave plastically. Points can not be outside of the yield surfaces, because if a point become plastic the stress does not change.

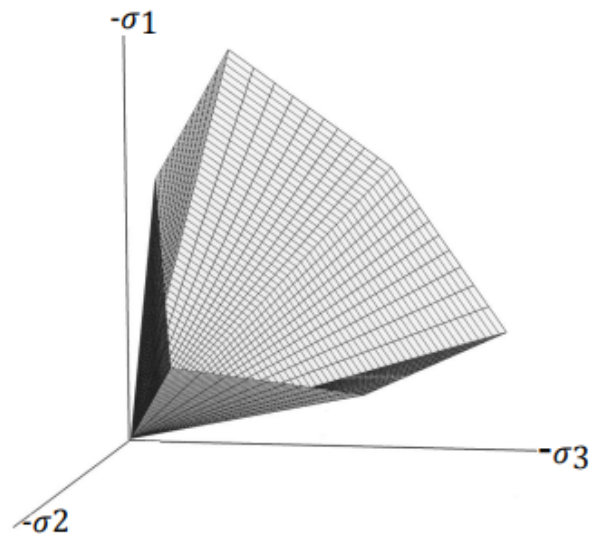


Figure 4.2: The Mohr-Coulomb yield surface in principal stress space ($c=0$) (Plaxis, 2023a).

4.2.2. User-Defined: N2PC-MCT model

This section is mainly based on the N2PC-MCT manual Plaxis (2022). For the halite the user-defined N2PC-MC model is being used. This is a visco-plastic creep model including a plastic failure mechanism for rocks. The Zechstein rock salt is considered to be visco-elastic, however, a visco-plastic model is being used. Plaxis does contain a visco-elastic model, however, this model is not specifically designed for salt creep and uses relaxation parameters, which are not known for the Zechstein. Therefore, I have chosen to use the visco-plastic model, which is specifically designed for rock salt. The difference between a visco-elastic and visco-plastic model is shown in Figure 4.3. After stress release the strain does not return to its initial state for the visco-plastic model. Only depletion is considered in this study and no injection after depletion. Therefore there is no stress release, hence the visco-plastic model is applicable for this study.

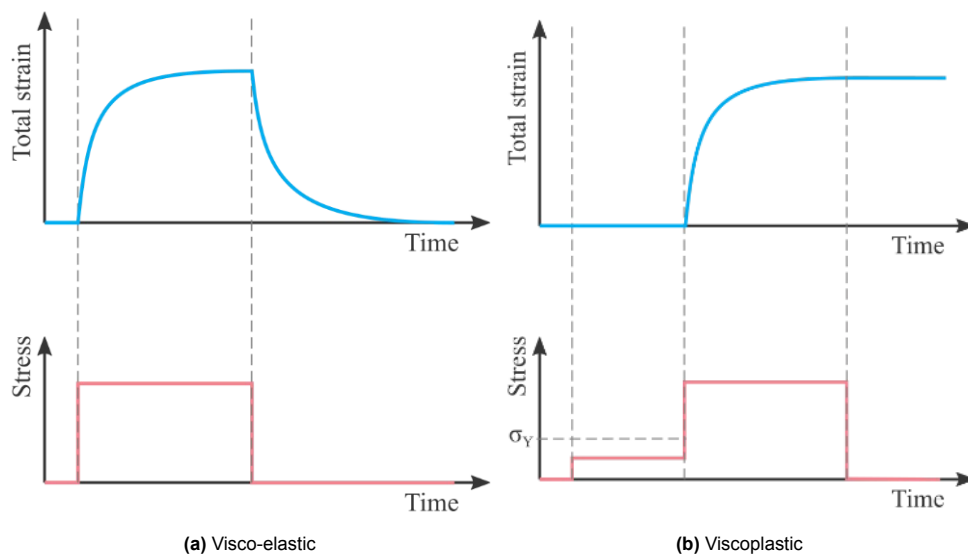


Figure 4.3: Difference between visco-elastic and visco-plastic strain behaviour as a function of stress. (Retrieved from lecture slides CEGM2006)

The deformation of the N2PC-MC model is described by the following equation:

$$\varepsilon = \varepsilon^e + \varepsilon^{vp} + \varepsilon^p \quad (4.8)$$

This equation has similar terms as the Mohr-Coulomb model, however an extra strain element is added: ε^{vp} , which is the viscoplastic strain, including creep behaviour. The viscoplastic strain is modelled as follows:

$$|\dot{\varepsilon}^{vp}| = A_1 e^{-\frac{Q_1}{R} \frac{1}{T}} \left(\frac{q}{q_0} \right)^{N_1} + A_2 e^{-\frac{Q_1}{R} \frac{1}{T}} \left(\frac{q}{q_0} \right)^{N_2} \quad (4.9)$$

In which q_0 is the reference stress, N is a stress exponent parameters (typically ranging from 1-8) and the $Ae^{-\frac{Q_1}{R} \frac{1}{T}}$ a viscosity like parameters (1/time unit).

The equation is comparable to Equations 3.9, 3.10 and 3.11. The power law equation of the dislocation creep is similar to the first term of equation 4.9. The q_0 is added in this equation, but that is included in the A_0 parameter of equation 3.9. On the other hand, the pressure solution strain equation (3.10) is slightly different from the second term in this equation. The pressure solution is dependent on the grain size, which is missing in this equation, as well as the grain size exponent. Furthermore, the parameters are similar to the literature.

Points that experience creep strain (ε^{vp}) are displayed within the Plaxis Output as "cap points".

4.2.3. Discontinuity: Mohr-Coulomb model

This section is mainly based on the Plaxis reference material (Plaxis, 2023b).

Similar to the rock materials, the fault will be modelled with the Mohr Coulomb model. The Mohr Coulomb model for discontinuities uses stiffness parameters k_n and k_s , to model the elastic behaviour (see figure 4.4a) instead of the Young's and Shear modulus.

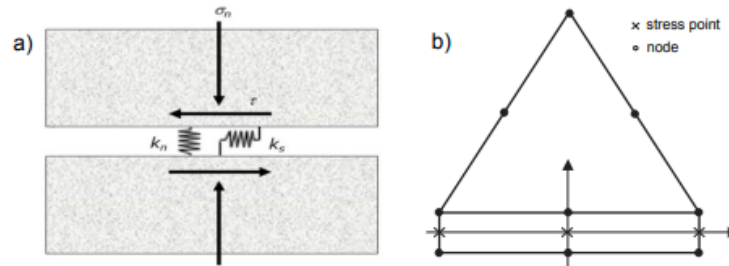


Figure 4.4: Discontinuity element. a) Illustration of discontinuity implementation b) Discontinuity element with 6-node distribution (Plaxis, 2023b).

Furthermore, the implementation in Plaxis is similar to the materials Mohr Coulomb model, however, for the discontinuity slip weakening can be added. Once the peak strength of the discontinuity is reached, the discontinuity strength will be reduced from its initial strength to a residual strength μ_d (as mentioned Section 3.2.2), described by the following equations:

$$RSF = \frac{\mu_d}{\mu_s} = \frac{\tan\varphi_{res}}{\tan\varphi_{ini}} \quad (4.10)$$

$$c_{res} = RSF \cdot c_{ini} \quad (4.11)$$

If $RSF = 1$, there is no weakening of the fault after failure.

Most studies use linear slip-weakening for fault modelling, in which the friction and cohesion are linearly decreased over a slip distance until a critical slip distance is reached. In this model there is no slip weakening, but the friction coefficient is directly reduced to its dynamic value with failure.

5

Model set-up

In this chapter the methodology behind the model definition will be explained as well as which parameters will be analysed in the conclusion. It will become clear which assumptions have been made and what the sources are for the input data. The approach and model set-up will be similar to the study of Buijze et al. (2017), which uses a model of the Groningen gas field. However, this study will also include models for other gas fields.

Section 5.1, will discuss the different kind of models and their geometries. The input parameters that are used will be explained in Section 5.2. Finally, Section 5.3 will discuss which output results will be analysed and why.

5.1. Model Geometry

As mentioned in Chapter 2.1, seismicity can be allocated to both Rotliegend and Zechstein Carbonate gas fields in the North-East of the Netherlands. To compare the effect of the viscous Zechstein, separate models will be made for those fields. The set-up of the models will be similar, however, there will be a difference in geometry and lithostratigraphy. For example as mentioned in Chapter 2.2, in the North of the study area, you can find the Rotliegend ten Boer and Slochteren layers, whereas to the South these layers disappear. On the contrary, in the south formations from the Jurassic layer are present, whereas these are not present in the Northern part of the area.

The following sections will discuss the model lithostratigraphy for the different models and which data is used to determine this. There will be four different models, two Rotliegend models and two Carbonate models, with a distinction in depth and location, which leads to a differences in the various layer thicknesses. A Carbonate shallow and deep model and a Rotliegend shallow and deep model. Finally, the Rotliegend shallow and deep models will be subdivided into again two different models with different offsets. Resulting in a total of six different model geometries.

5.1.1. Rotliegend shallow model

Different studies have been using a model of the Groningen gas field, for this project the study of Buijze et al. (2017) is being used as a guideline for the Rotliegend shallow model. As this allows to make reliable decisions and to validate the results of the software in the end. Buijze et al. (2017), uses the lithology of the Stedum-01 well (SDM-01) as a reference. The stratigraphy and the final formations of their model are summarized in Figure 5.1. When comparing the stratigraphy (Left side of the figure) and the final depths/thicknesses (Top right of the figure), it can be seen that the thin ZE1K copper shale member is left out of the final model. The ZE1W Anhydrite member and the ZE1C carbonate member are combined into one formation, whereas the ZE2A Anhydrite member and ZE2C carbonate member have been divided into two separate layers. This will also be done in this project as for the Carbonate fields the ZE2C Carbonate member is the reservoir formation, so a separate layer for this formation allows for a comparison between the different fields. Buijze et al. (2017) uses the ZE2H Halite layer as top layer (which include multiple smaller Zechstein layers with mainly halite), with a homogeneous overburden of 2000m thickness. In this project the overburden will not be modelled as

one homogeneous layer, but will be subdivided into a few big formations, as discussed in Section 2.2.3.

The depth of the Slochteren member is at 2845m according to Buijze et al. (2017) and the thickness is 200m. In this project the thickness is the same, but depth is rounded to 2850m. Consequently the other layers are also 5 meters deeper. For the overburden formations and the top of the halite layer, again well SDM-01 is being used to determine the depths and the thicknesses. However, more wells from NLOG have been used to compare and validate the lithologies of the SDM-01 well. The wells that are used are Zeerijp-01 (ZRP-01), de Paauwen-01 (PAU-01), Barnheem-01 (BRH-01), Oldorp-01 (ODP-01) and Schildmeer-01 (SMR-01) wells. These wells are all located in the Loppersum area, which is the area that is most effected by earthquakes as described in Section 2.1.1. Table B.3 in the appendix, summarizes the formation depths for all the used wells. The depths are retrieved from the stratigraphic units along the borehole in NLOG, after which they are corrected to the true vertical depth. From the table it can be seen that the lithostratigraphy of the wells is relatively similar. The final thicknesses and depths of the formations for the Rotliegend Shallow model can be found in Table 5.1.

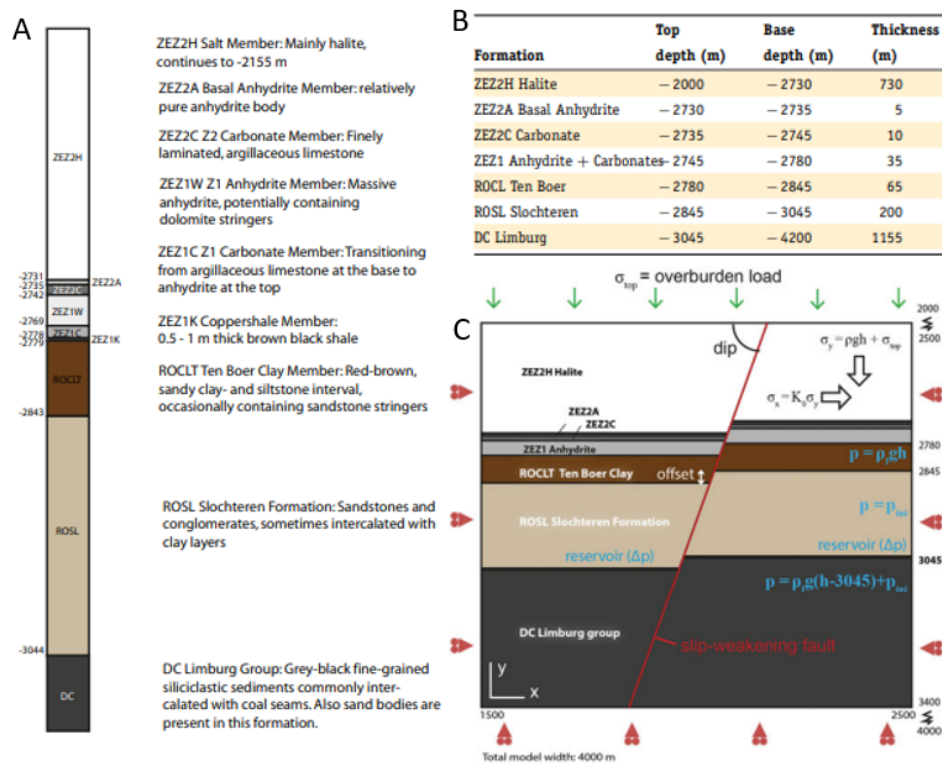


Figure 5.1: Model description of the study of Buijze et al. (2017): A) Lithostratigraphy of Northwestern part of the Groningen field, taken from SDM-01. B) Input parameters for model formations. C) Model geometry.

5.1.2. Carbonate shallow model

In order to make an appropriate comparison between the Rotliegend and Carbonate reservoirs, the depth of the Carbonate ZEZ2C formation should be similar to the depth of the Rotliegend Slochteren formation. Figure 2.5, shows the depth of the Carbonate fields, giving a depth around the 2850 meter for the following fields: Schoonebeek = 2900m, Dalen = 2950 and Coevorden = 2760. Wells of these fields will be used for the stratigraphy of the Carbonate Shallow model. The wells that are used can be found in Table B.1 in the appendix, with the true vertical depth per formation, retrieved from NLOG. The Dalen and Schoonebeek wells are selected because they are closest to previous epicenters of seismic events or because they are close to the fault which in theory can cause the biggest earthquake (Van Thienen-Visser et al., 2016). For the Coevorden field the wells are selected throughout the whole field. The final thicknesses of the formations (see Table 5.1) are approximately based on the average layer thicknesses from all the wells. Some small adjustments have been made in the overburden layers with the largest standard deviation such that the ZEZ2C reservoir is at a depth of 2850m, similar to the

Rotliegend shallow model. The final reservoir thickness equals 60m.

5.1.3. Carbonate deep model

From Figures 2.3 and 2.5, it can be seen that for both the Rotliegend and Carbonate fields there is a large variation in depth of the different gas fields. Because both shallower and deeper fields can be linked to seismicity, it is decided to make additional models with a greater depth. This will help to understand the impact of the viscous salt at higher stresses and temperatures. After all, the viscous behaviour of the salt is dependent on the temperature and stresses (see Equation 3.11). The deepest field for the carbonate reservoir is the Emmen field located around a depth of 3700 meters. Log data from this field will be used for the model. Figure 5.2, shows that the ZE2C reservoir layer and the Zechstein halite layer are very heterogeneous throughout the field, which makes it more difficult to choose a suitable model. The heterogeneity is being expected, because as discussed in Section 2.2.2, the presence of the platform, slope and basin cause a large change variability in thicknesses of the anhydrite, carbonate and halite layers (Figure 2.10). The thick halite layer in the east is more located in the basin, giving a larger thickness.

Multiple wells have been compared and taken into consideration (Emmen-08/09/10/12/14), however in the end it is chosen to use wells EMM-08 and EMM-09 for the final model. These wells are located closest to the seismicity, which is mainly located at the south side of the field (Van Thienen-Visser et al., 2016). The average thickness of these two wells is being used for the lithostratigraphy. The final depth of the reservoir is set at 3680m as this also matches the Rotliegend wells in the next section.

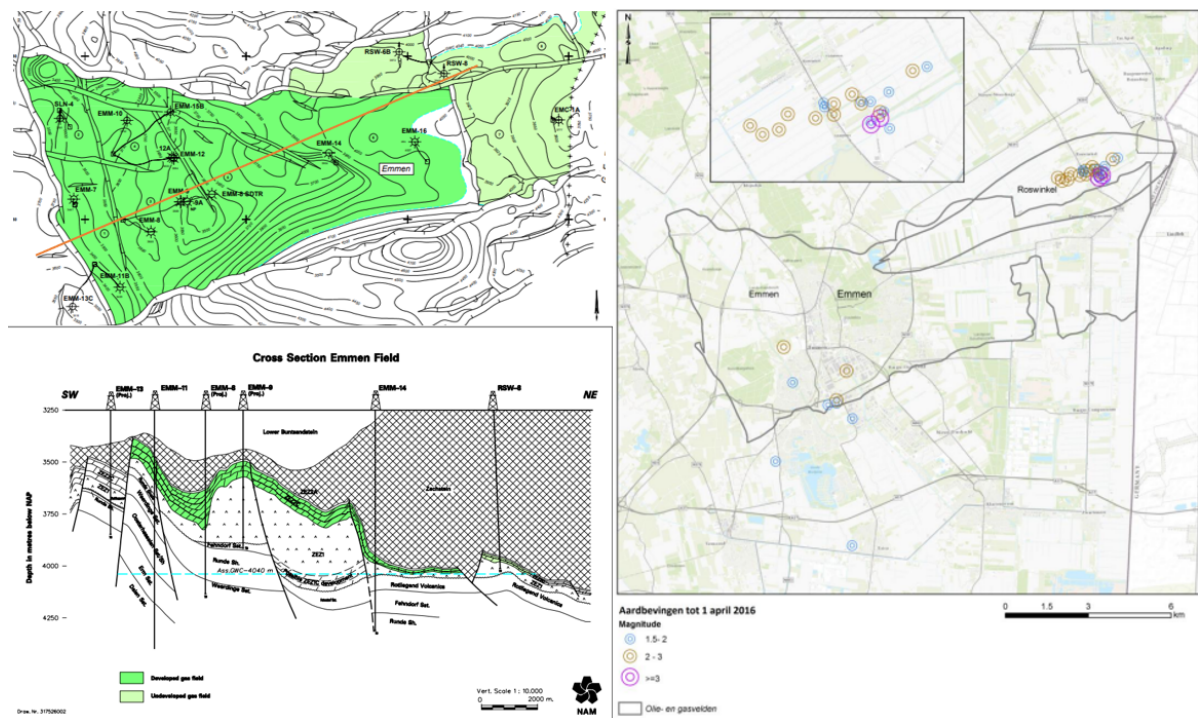


Figure 5.2: Overview of the Emmen gas field, with top left contour/structure map including the wells (www.nlog.nl). Bottom left the cross section, crossing the orange line (winningsplan Emmen nlog). At the right the recorded seismic events (Van Thienen-Visser et al., 2016).

5.1.4. Rotliegend deep model

Figure 5.3, shows the Rotliegend fields which are approximately at the same depth as the Emmen field. From these fields log data will be used: Nes (3680m), Mestlawier (3650m) and Anjum (3760m). The wells that are being used are Moddergat-02 (MDG-02 in Nes field), Anjum-02 (ANJ-02: Mestlawier field) and Anjum-01 (ANJ-01: Anjum field) (see also Table B.4 in the appendix). The final model is mainly based on well ANJ-02, as this well has similar Zechstein halite thickness as the shallow Rotliegend model. The other wells have thinner halite layers. The difference between the wells is relatively large, giving a larger uncertainty for this model. The final thicknesses and depths of the Rotliegend deep

mode can be seen in Table 5.1.

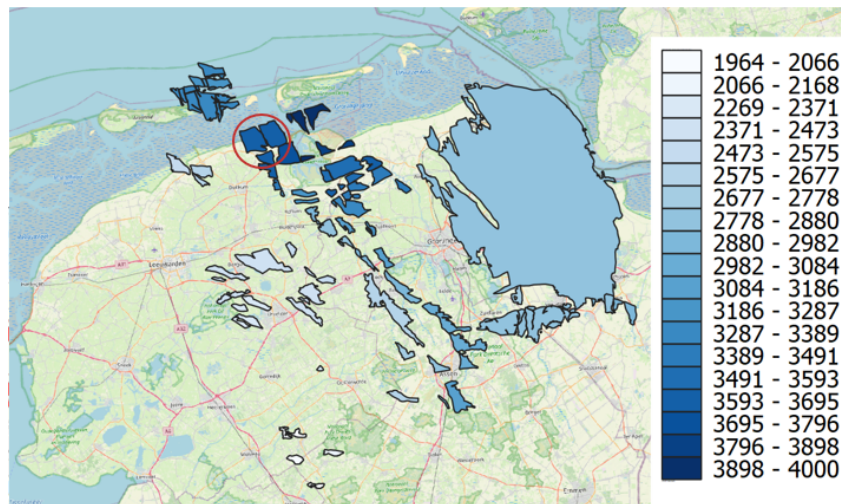


Figure 5.3: Overview of depth the onshore Rotliegend fields. In the red circle the 3 fields are indicated with a depth around 3700m.

Table 5.1: Final thicknesses and depths of the formations for the different models. The reservoir layer is indicated with the dark green colour and the layers which are not included in the model because they are too thin are indicated with the stars. The ZE1 layer consist of the ZE1W anhydrite member and the ZE1C carbonate member.

Formation	Carbonate				Rotliegend			
	Shallow		Deep		Shallow		Deep	
	Thickness	Depth	Thickness	Depth	Thickness	Depth	Thickness	Depth
Tertiary	400	0	380	0	850	0	1200	0
Cretaceous	750	400	1150	380	955	850	950	1200
Jurassic	255	1150	310	1530		1805		2150
Triassic	1000	1405	1480	1840	130	1805	500	2150
Halite (Zechstein)	440	2405	350	3320	800	1935	900	2650
ZE2A	5	2845	10	3670	5	2735	5	3550
ZE2C	60	2850	100	3680	10	2740	10	3555
ZE1	50	2910	125	3780	35	2750	35	3565
Coppershale member	1*		1*		1*		1*	
ten Boer					65	2785	80	3600
Slochteren	1*		1*		200	2850	220	3680
Carboniferous		2960		3905		3050		3900

5.1.5. Fault geometry and the model boundaries

Fault geometry

In contrast to the stratigraphies the fault geometry that is modelled will be the same for the different reservoir models. As this will allow comparisons in stress between the different models. A normal fault is included with a dip of 70 degrees, which is slightly steeper than the 60 degrees which is expected for a normal fault with respect to the principal stresses. However, 70 degrees is in line with the value used in other studies (Buijze et al., 2017; Muntendam-Bos, 2021).

At the top end, the fault propagates into the Basal Zechstein layers and stops at the bottom boundary of the Halite layer in the footwall. At the bottom, the fault propagates to roughly 5500m depth in the Carboniferous.

Fault offset

The fault offset that is being used in all models is 1/4 of the reservoir thickness, which corresponds to the real offsets given in Table 5.2. For Groningen this is in line with the fault offsets near the SDM-01

and ZRP-01 well, which vary between 25 to 250m and in line with the offset of the major faults ranging between 50 and 150m (Buijze et al., 2017). It is also similar to the relative offset used in the study of Buijze et al. (2017) for the Groningen model (in this project Rotliegend shallow).

For the carbonate shallow and deep models this results respectively in offset of 15 and 25m. This relative offset juxtaposes the viscous Halite to the ZE2C reservoir, as the ZE2A layer in between is smaller than the offset. However, for the Rotliegend models this does not juxtapose the viscous halite to the Slochteren reservoir, as the layers in between the Slochteren and Halite (ten Boer, ZE21, ZE2C and ZE2A) are thicker together than the offset. For these models it has been decided to add an extra model with a relative offset equal to 3/4 of the reservoir thickness, to juxtapose the viscous halite to the reservoir. This offset is still in line with the Groningen fault offsets between the 25 and 250m.

Table 5.2: Overview of the real offsets corresponding to the relative offset

Relative offset	Real offset (m)			
	Carbonate shallow	Carbonate deep	rotliegend shallow	Rotliegend deep
1/4	15	25	50	55
3/4	x	x	150	165

Model boundaries

In order to prevent the boundaries from interacting with the stresses near the fault, the boundaries are taken at a sufficient distance from the fault. The top of the model is set at $y=0$, similar to the elevation of the Dutch surface (0 NAP). The bottom of the model is set at 6000m, which is at a significant distance from the stress changes in the depleted reservoir. The left and right boundary are at 0 and 6000m, which is far away from where the fault is crossing the reservoir and the Zechstein layers.

5.1.6. Elastic vs viscous Zechstein salt

The model geometries have now been defined for the reservoirs, an overview of these models implemented in Plaxis can be seen in Figure 5.4. These models will be used to compare the results for different salt characteristics. In one case the Halite layer is being modelled as a perfect elastic plastic model, without the viscous property (Mohr Coulomb model). In the other case, the halite layer is being modelled with a creep model (N2PC-MC model).

The intention was to have a model in which there is salt present in the fault, to simulate the intrusion of the salt. However, it is not possible to give material properties such as viscosity to a fault in Plaxis. Therefore the total amount of models will be 12, the overview is given in Figure 5.5.

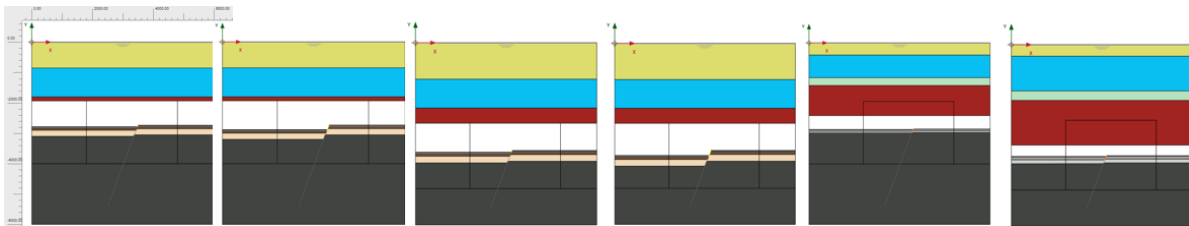


Figure 5.4: Overview of all the basic models. The layers correspond to the colour of the formations in table 5.1. From left to right: shallow Rotliegend 1/4 offset, shallow Rotliegend 3/4 offset, deep Rotliegend 1/4 offset, deep Rotliegend 3/4 offset, shallow carbonate and deep carbonate.

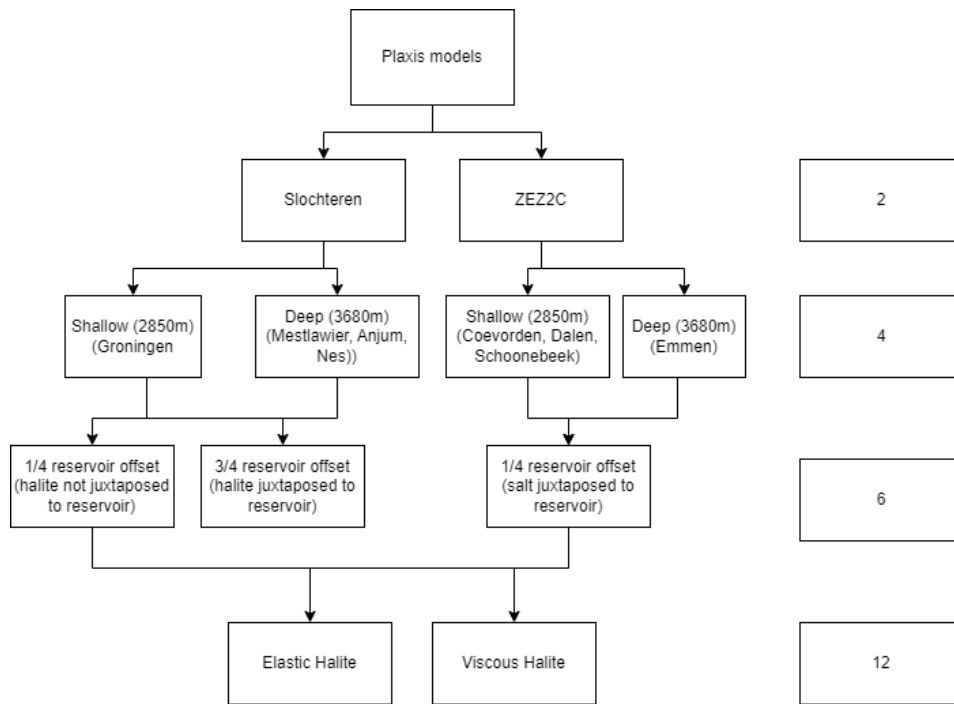


Figure 5.5: Overview of all the different models that are used

5.2. Model set-up in Plaxis

With the stratigraphy and model geometry being determined, the following step is to assign parameters to the layers and the fault, this will be done in this section. After assigning the parameters to the materials, the next step in Plaxis is to do the meshing, in which the resolution of the model will be defined. After the meshing, the different phases of the model must be defined, in which different pore pressures will be assigned to the model to simulate reservoir depletion.

5.2.1. Input parameters for the rock materials

As mentioned in Chapter 4, the linear elastic perfectly plastic Mohr-Coulomb model will be used to simulate the behaviour of the rocks. Except for the case in which the viscous property of the Zechstein halite layer is modelled. For this material the user-defined N2PC-MCT model is being used, which is a visco-plastic creep model (Plaxis, 2022). The input parameters that are needed for the Mohr-Coulomb and the N2PC-MCT models will be explained, as well as the source from which they are retrieved.

Mohr-Coulomb model

Figure 5.6, shows the input parameters needed for the Mohr Coulomb model. On the top of the figures the following tabsheets can be found: General, Mechanical, Groundwater, Thermal, Interfaces and Initial. The groundwater and thermal tabs are not needed, as groundwater and or thermal flow are neglected in this study. The interfaces tab is only needed if the material is assigned to a interface structure, this can be for example a fault. However, the fault will be modelled with a discontinuity element in this project. Therefore this tab will also not be used.

Similar to the model geometry, the input parameters have been mainly retrieved from Buijze et al. (2017), however, these do not include the overburden layers. These values will be mainly retrieved from Lele et al. (2015). There are some parameters, which are not included in one of these papers. An overview of all the parameters needed for the necessary tabsheets, with their sources is given in table 5.3

General			Mechanical			Groundwater			Thermal			Interfaces			Initial		
Property	Unit	Value	Property	Unit	Value	Property	Unit	Value	Property	Unit	Value	Property	Unit	Value	Property	Unit	Value
Material set			Stiffness			K0 settings											
Identification		Zechstein (Halite)	E'_{ref}	kN/m ²	35.00E6	K_0 determination		Manual									
Soil model		Mohr-Coulomb	ν (nu)		0.3500	$K_{0,x}$		1.000									
Drainage type		Drained	Alternatives			$K_{0,z}$		1.000									
Colour		<input type="checkbox"/> RGB 255, 255, 255	G_{ref}	kN/m ²	12.96E6	$K_{0,x} = K_{0,z}$		<input checked="" type="checkbox"/>									
Comments			E_{ped}	kN/m ²	56.17E6												
Unit weights			Depth-dependy														
γ_{unsat}	kN/m ³	21.50	E'_{inc}	kN/m ² /m	0.000												
γ_{sat}	kN/m ³	21.50	γ_{ref}	m	0.000												
Void ratio			Wave velocities														
e_{init}		1.00E-3	V_s	m/s	2432												
n_{init}		1.000E-3	V_p	m/s	5063												
Rayleigh damping			Strength														
Input method		SDOF equivalent	Shear														
Rayleigh α		0.000	c'_{ref}	kN/m ²	4800												
Rayleigh β		0.000	ϕ' (phi)	°	38.66												
ξ_1	%	0.000	ψ (psi)	°	0.000												
ξ_2	%	0.000	Depth-dependy														
f_1	Hz	0.1000	c'_{inc}	kN/m ² /m	0.000												
f_2	Hz	1.000	γ_{ref}	m	0.000												
			Tension														
			Tension cut-off		<input checked="" type="checkbox"/>												
			Tensile strength	kN/m ²	0.000												

Figure 5.6: Tabsheets with the needed input parameters for the Mohr-Coulomb model, here shown for the Zechstein Halite layer (non-viscous as Mohr-Coulomb is being used).

For the density, Young's Modulus and Poisson's ratio, the values for the Tertiary, Cretaceous and Triassic layers are retrieved from Lele et al. (2015). This study, does not take into account the Jurassic layer, similar to other papers, which model the Groningen reservoir, as the Jurassic layer is not present above the Rotliegend gas fields. However, the paper from Orlic (2016), does take into account the Altena group in their model in the West of the Netherlands and this paper shows the same values for Jurassic and Triassic layers. This is also in line with the description in Dinoloket as the formations both consist of mainly claystones (see also chapter 2.2). Therefore it has been decided to use the Triassic values from Lele et al. (2015), for the Jurassic layer.

Both the papers from Lele et al. (2015) and Buijze et al. (2017) do not contain any porosity values. Different porosity values have been found from different sources, these values can be found in Figure B.5 in the appendix. The final value for the ZE22C is based on the thesis of Paulides (2016), as this study contains porosity values from the Dalen and Emmen fields which are also used in this project.

The Young's modulus and the Poisson's ratio have been retrieved in a similar manner as the density, the overburden layers from Lele et al. (2015) and the other layers from Buijze et al. (2017). However, the Slochteren value used in Buijze et al. (2017) for the Poisson's ratio was significantly lower (0.1) than in other sources BOA (1993) = 0.25, Muntendam-Bos et al. (2008) = 0.1-0.25, TNO (2015) = 0.2 and Muntendam-Bos (2021) = 0.2. The Poisson's ratio is depended on the porosity of the formation, the higher the porosity, the higher the Poisson's ratio Lele et al. (2015). For the Slochteren sandstone this results in a Poisson's range varying between 0.1-0.25 Muntendam-Bos et al. (2008). The low Poisson's ratio of 0.1 causes numerical instabilities, as it inhibites the model to converge, therefore it is decided to use a larger Poisson's ratio of 0.2 for the Slochteren sandstone.

In the initial tab the K_0 value must be selected, this is the ratio of the effective horizontal stress and the effective vertical stress (similar to equation 3.8). According to Muntendam-Bos (2021), K_0 can reach up to much higher values approaching a lithostatic K_0 of 1 when overlain by a thick isotropic, viscous Zechstein formation. The thicker the Zechstein formation the high effective stress ratio, giving high ratio's in the Rotliegend and Zechstein reservoirs considered in this project.

The stress ratios from the study of Buijze et al. (2017) can not be used as the stress ratio is defined as the total stress ratio in this study, whereas Plaxis uses the effective stress ratio. Therefore, the ratio is being calculated with the horizontal stress gradient retrieved from Muntendam-Bos (2021) and the vertical stress gradient of the overburden. For the Rotliegend reservoirs in the Groningen High

and Lauwerssea Trough the horizontal stress gradient equals 19.9 MPa/km ($d < 1.5\text{km}$) and for the Carbonate reservoirs in the Lower Saxony Basin the stress gradient equals 19.6 MPa/km (Zechstein is thinner in LSB, giving lower gradient). The vertical stress gradient is set to 22 MPa as this corresponds approximately to the average densities of the overburden layers. With the pore pressure of 35 MPa in the shallow models (explained later) at 2850m depth, this results in a K_0 ratio of 0.78 for the Rotliegend reservoir in the GH and LT and $K_0 = 0.75$ for the carbonate reservoir in the LSB. The 0.78 will be assigned to the Carboniferous, Slochteren and Ten Boer. The 0.75 will be assigned to the ZEZ1, ZEZ2C and ZEZ2A, for simplicity also in the Rotliegend models in the GH and LT. With depth the overpressure becomes larger in the North of the Netherlands (Verweij et al., 2012), which results in a smaller K_0 ratio for the deeper reservoir (0.75 (ROT) and 0.71 (CARB)). However, due to time constraints the K_0 ratios will be set similar for the shallow and deep models. This assumption affects the results in a way that for the deep model fault reactivation takes place for larger depletion pressure, as a smaller K_0 gives a easier reactivation. The exact impact of this assumption will be extensively covered in the results and discussion chapters (8 and 7).

For the isotropic halite, the K_0 ratio equals 1. The K_0 for the layers above the halite are calculated with the horizontal stress gradient of 14.8 MPa ($d < 1.5\text{km}$) and a hydrostatic water gradient, giving a ratio of 0.4. It is also assumed that the K_0 value is equal in both the horizontal directions, as the level of anisotropy is found to be very low (2-3%) (Muntendam-Bos, 2021). With the uncertainty of the K_0 values this percentage can be neglected.

Table 5.3: Input parameters for the Mohr Coulomb model. The bold parameters are the needed input parameters in Plaxis, the other parameters are either needed to calculate the bold parameters or are calculated from the bold parameters.

Parameter	Tertiary	Cretaceous	Triassic	Jurassic	Halite	ZEZ2A	ZEZ2C	ZEZ1A	TB	SS	DC	Source
General:												
ρ (kg/m ³)	2150	2350	2350	2350	2150	2900	2700	2900	2500	2500	2700	Lele et al. (2015) and Buijze et al. (2017)
γ (kN/m ³)	21.5	23.5	23.5	23.5	21.5	29	27	29	25	25	27	
ϕ or n (-)	0.35	0.25	0.18	0.2	0.001	0.02	0.02	0.02	0.07	0.15	0.05	see appendix figure B.5
e	0.538	0.333	0.220	0.25	0.001	0.111	0.111	0.111	0.075	0.176	0.053	
Mechanical:												
E_{ref} (GPa)	2	10	16	16	35.00	65.00	35.00	65.00	20.00	15.00	25.00	Lele et al. (2015) and Buijze et al. (2017)
ν	0.3	0.25	0.25	0.25	0.35	0.30	0.30	0.30	0.20	0.20	0.20	Lele et al. (2015) and Buijze et al. (2017)
G_{ref} (GPa)	0.77	4.00	6.40	6.40	12.96	25.00	13.46	25.00	9.09	6.82	10.42	equation ??
E_{oed} (GPa)	2.69	12.00	19.20	19.20	56.17	87.50	47.12	87.50	20.45	15.34	27.78	$\frac{E(1-\nu)}{1+\nu(1-2\nu)}$
V_s (m/s)	598.15	1304.66	1650.27	1650.27	2455.46	2936.10	2232.88	2936.10	1906.93	1651.45	1964.19	$\sqrt{G/\rho}$ Plaxis (2023b)
V_p (m/s)	964.49	2062.84	2609.31	2609.31	4034.73	4734.32	3600.41	4734.32	2828.43	2449.49	3042.90	$\sqrt{E/\rho}$ Plaxis (2023b)
c (MPa)	0	3	5	5	5	5	5	5	5	8	5	BOA (1993) and Hol et al. (2015)
μ		0.7	0.7	0.7	0.8	0.7	0.7	0.7	0.38	0.6	0.5	Hunfeld (2020) (Figure B.6) & Muntendam-Bos (2021).
φ (°)	20	34.99	34.99	34.99	38.66	34.99	34.99	34.99	20.81	30.96	26.57	$\tan^{-1}(\mu)$, Tertiary from BOA (1993)
ψ (°)										15.6		Pijnenburg (2019)
Initial:												
K_0	0.4	0.4	0.4	0.4	1	0.75	0.75	0.75	0.78	0.78	0.78	Muntendam-Bos (2021)

Norton's creep model

For the N2PC-MCT creep model, that is used to model the viscous behaviour of the halite, the user-defined option must be selected as soil model in the general tab. Furthermore, the parameters in the general tab as well as the initial tab are similar to the Mohr Coulomb model, only the mechanical tab is different. Figure 5.7, shows the input parameters needed for the N2PC-MCT model and the corresponding values that are used. On top the N2PC-MCT model is being selected. The Shear modulus (G), the poisson's ratio (ν), Cohesion, friction angle and dilation angle are equal to the halite values in the Mohr Coulomb model. The tensile strength is set to a very small value of 100 kPa, as it is recommended to use a value larger than zero to avoid numerical instability (Plaxis, 2022).

The parameters that are different from the Mohr-Coulomb model are the $A1/A2$, $N1/N2$, $Q1/Q2$ and the $q0$ values, which are the viscous parameters explained in Chapter 4. The values for these parameters are retrieved from an example in the Plaxis manual Plaxis (2022), which uses a rock salt model with dislocation creep and pressure solution, similar to this study. There also have been some studies on the parameters of rock salt (Li et al., 2012; Li & Urai, 2016), however these use the slightly different equations from Section 3.3.2 and are not specifically for the Zechstein halite. Therefore it has chosen to use parameters specifically for the equations used in the Plaxis model.

Another parameter is the deviatoric stress threshold q_{th} , which is the minimum deviatoric stress for which the material starts to behave viscous. This is set to 0.2 MPa, which is the minimum deviatoric stress threshold for pressure solution creep according to Oosterhout et al. (2022).

General Mechanical Groundwater Thermal Interfaces Initial			
Property	Unit	Value	
User-defined model			
DLL file		n2pc_salt64.dll	
Model in DLL		CreepRock_N2PC_MCT	
User-defined parameters			
Elastic shear modulus G	kN/m ²	12.96E6	
Poisson ratio nu		0.3500	
Stress exponent N1		5.000	
A1 (or A1* if Ignoring Temp.)	1/day	0.6220	
Stress exponent N2		1.000	
A2 (or A2* if Ignoring Temp.)	1/day	40.60	
Unit reference stress q0	kN/m ²	1000	
Q1/R (Not needed if Ignoring Temp.)	K	6485	
Q2/R (Not needed if Ignoring Temp.)	K	2950	
Deviatoric stress threshold q _{th}	kN/m ²	3000	
Cohesion C	kN/m ²	4800	
Friction angle Phi	°	38.66	
Dilation angle Psi	°	0.000	
Tensile strength sig _T	kN/m ²	100.0	
Excess pore pressure calculation			
Determination		v-undrained definition	
v _{w, equivalent} (nu)		0.4950	

Figure 5.7: Mechanical tabsheet for the N2PC-MCT creep model, for the viscous Zechstein Halite layer.

5.2.2. Input parameters for the fault sections

As the fault only juxtaposes the Carboniferous, Slochteren, Ten Boer and the Zechstein layers, there are no fault elements needed for the overburden layers. The fault is being modelled with the discontinuity element and the parameters that are needed are shown in Figure 5.8. Similar to the rock materials, the groundwater and thermal tabs are not needed.

General Mechanical Groundwater Thermal			General Mechanical Groundwater Thermal		
Property	Unit	Value	Property	Unit	Value
Material set			Properties		
Identification		33	Stiffness		
Material model		Mohr-Coulomb	Normal stiffness, k _n	kN/m ³	150.0E6
Drainage type		Drained	Shear stiffness, k _s	kN/m ³	68.20E6
Colour		RGB 196, 180, 130	Strength		
Comments			Strength method		Peak and Residual
			Cohesion, c'	kN/m ²	0.000
			Friction angle, φ' (phi)	°	30.96
			Dilatancy angle, ψ (psi)	°	0.000
			Residual Strength Factor (RSF)		0.5800
			Consider gap closure		<input checked="" type="checkbox"/>

Figure 5.8: Tabsheets with the needed input parameters for the discontinuity element, in this case for the Slochteren Sandstone

The stiffness parameters can be calculated from the Young's and Shear moduli, by the following equa-

tions (Buijze, 2020):

$$k_n = f_k E \quad (5.1)$$

$$k_s = f_k G \quad (5.2)$$

In which $f_k = 1/w$ (Mulders, 2003) is the thickness of the fault zone. The discontinuity element in the geometry has a zero thickness, but by adding the f_k term to the moduli a finite thickness is represented. Assuming the fault zone is thin, elastic displacements on the fault should be very small compared to deformation in the surrounding formations. To achieve this the stiffness should be as high as possible without inhibiting convergence in the model Buijze et al. (2017). $f_k = 10$ is being used similar to Buijze et al. (2017) and Buijze (2020), as this corresponds to a typical value for faults with an offset of 10-100m.

The fault is assumed to be cohesionless, in agreement with other studies Orlić & Wassing (2012) & van den Bogert (2018). This in contrast to the study of Buijze et al. (2017), which does assign a small cohesion to the fault, as a consequence of the fault healing. The longer the healing time, the greater the re-strengthening of the fault and the higher the cohesion. After, the critical slip distance is being reached again, Buijze et al. (2017) does use a cohesionless fault. For simplicity and due to limitations in Plaxis fault healing is being ignored and a cohesion of zero is being used.

The friction angles are taken from the study of Hunfeld (2020), which empirically measures the frictional properties of the fault gouge in the Groningen gas field. The Residual strength factor is calculated using Equation 4.10 and the static and dynamic friction coefficient from Hunfeld (2020) (see Figure B.6 in appendix). The static and dynamic friction coefficient for the Zechstein rocksalt equals 0.8 (Buijze, 2020). The parameters for all the fault elements can be found in Table 5.4.

For simplicity the fault element can only be assigned to one lithology. When two different lithologies are juxtaposed, the fault element will be assigned to the weakest lithology, with TB<DC<SS<BZ. For any juxtaposition with the rocksalt, the friction coefficient is taken from the rocksalt.

Table 5.4: Input parameters for the discontinuity elements with their corresponding source.

Parameter	Halite	ZEZ2A	ZEZ2C	ZEZ1A	TB	SS	DC	Source:
c'ref	0	0	0	0	0	0	0	van den Bogert (2018)
μ_{ini}	0.8	0.7	0.7	0.7	0.38	0.6	0.5	Hunfeld (2020)
φ	38.66	34.99	34.99	34.99	20.81	30.96	26.57	$\tan^{-1}(\mu)$
Ψ						15.6		Pijenburg (2019)
fk	10	10	10	10	10	10	10	Buijze (2020)
kn	350	650	350	650	200	150	250	equation 5.1
ks	129.63	250.00	134.62	250.00	90.91	68.18	104.17	equation 5.2
μ_{after}	0.8	0.27	0.27	0.27	0.3	0.35	0.3	Hunfeld (2020)
RSF	1.00	0.39	0.39	0.39	0.79	0.58	0.60	μ_{after}/μ_{ini}

5.2.3. Meshing in Plaxis

After the geometry and the input parameters have been defined, the geometry has to be divided into elements, for the finite element calculations. The composition of the finite elements is called a mesh and is created in the mesh mode (Plaxis, 2023b). A finer mesh will give a better accuracy, however this increases the computational time. The distribution of the mesh resolution is defined by the coarseness factor, with a standard value of one. The coarseness factor must be assigned to all the layers, boundaries and discontinuity elements. Lower than one gives a finer mesh and bigger than one gives a coarser mesh. Thinner layers in general have smaller finite elements and thus a finer grid. It is decided that the fault element has the finest mesh with a coarseness factor of 0.25, as the results along the fault will be analysed. Around the fault and the reservoir layers the coarseness factor will be 1. The further away from the reservoir and fault the coarser the mesh becomes, up to a coarseness factor of 4.0 in the Tertiary layer. After defining the coarseness factor the mesh of the whole model can be run, with a specific resolution for the whole model, which is set to the default setting: medium. The input mesh for the Carbonate shallow model can be found in Figure 5.9, together with the corresponding output mesh. As can be seen the elements are largest in the top layer and the bottom of the model and decrease in

size towards the centre. Each triangular element consist of 15 nodes, distributed over the element (12 along the boundary and 3 in the centre).

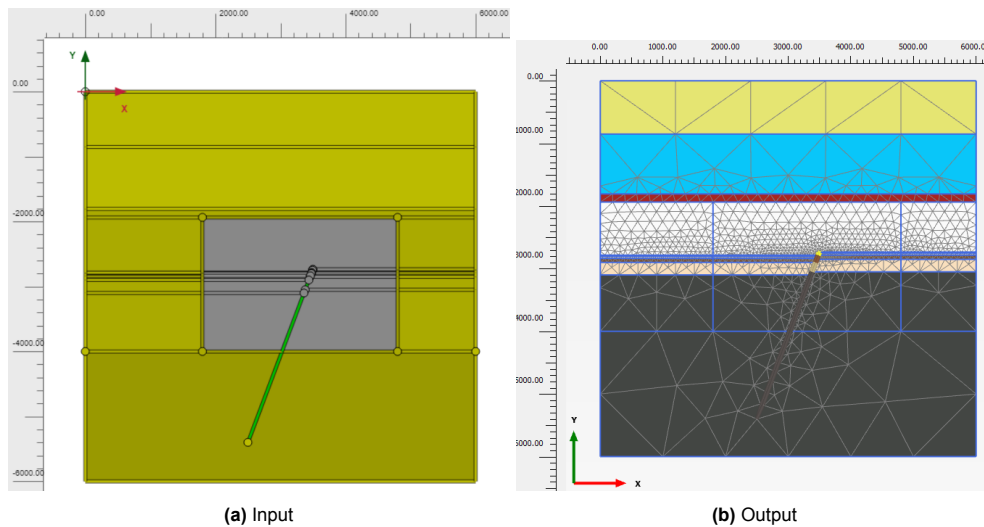


Figure 5.9: Overview of the mesh in and output in Plaxis. The bright green colour corresponds to a coarseness factor of 0.25, the grey colour to 1 and the yellow-greenish colour to ≥ 2 .

5.2.4. Phase construction

The next step is to assign the different phases to the model. The first phase that is being defined is the model before the initialization. This phase is calculated as the K_0 procedure, in which the initial stresses are defined based on the K_0 values of the layers. After this step, the initialization takes place in the second phase. A plastic calculation is used to carry out an elastic-plastic deformation analysis with the initial stresses. This will be done for the initial pore pressure. The phases that will follow next will contain the reservoir pressure for depletion and will also be calculated with the plastic calculation.

Pore pressure

In order to define the initial phase the initial pore pressure is needed. The formation fluids in the North of the Netherlands are generally overpressurised (Verweij et al., 2012), meaning that the pore pressure is higher than hydrostatic pressure. For the Groningen gas field the initial pressure equals 35MPa, which is an overpressure of about 7.5 MPa. According to the "winningsplannen" retrieved from NLOG and the results from Verweij et al. (2012) the initial pressure for the Coevorden, Dalen and Schoonebeek (Carbonate shallow fields) is also about 7-8 MPa higher than the hydrostatic pressure. Therefore it has been decided to set the initial pore pressure of the shallow reservoirs to 35 MPa. For the Deep reservoirs (>3500m depth) the overpressure is about 10-20 MPa for the Rotliegend formation in the Lauwerssea Trough (Anjum, Nes and Mestlawier) and Zechstein formation in the Lower Saxony Basin (Emmen field) (Verweij et al., 2012). With the large uncertainty it is decided to set the initial reservoir pressure for the deep reservoirs at 50 MPa, which is in agreement with the overpressure of 10-20 MPa. For depletion it has been decided to decrease the pore pressure by $\Delta P = 10$ MPa, per phase, which results in Table 5.5 with reservoir pressures per phase. The pressure is assumed to be equal throughout the reservoir as the reservoir contains gas, which has a very low hydrostatic gradient (2 MPa/km against 10 MPa/km for water).

Table 5.5: The reservoir pressure per calculation phase

Pressure (MPa):	Phase 1: before initialization	Phase 2: after initialization	Phase 3	Phase 4	Phase 5	Phase 6
Model:						
Shallow	35	35	25	15	5	x
Deep	50	50	40	30	20	10

For layers other than the reservoir and for the fault sections, the following assumptions have been

made:

- The halite layer gets a pore pressure of zero, due to the absence of porosity
- Below the halite the layers get the hydrostatic pressure of water plus the same overpressure as for the reservoir (7.5 MPa for shallow models and 14 MPa for deep models)
- Layers above halite get hydrostatic pressure of water without overpressure
- Only the pore pressure is reduced in the reservoir (ZEZ2C for carbonte models and Slochteren for Rotliegend), not in surrounding layers
- The pore pressure is reduced evenly throughout the whole reservoir
- The discontinuity elements adjacent to the reservoir get the reservoir pore pressure, except for the halite fault section (0 MPa)

Phase assumptions for viscous model

The viscous material model is dependent on temperature (Equation 4.9). Therefore, the temperature of the model is set to an earth gradient of 31.3 K/km, which is the average thermal gradient of the Netherlands (Bonté et al., 2012). The temperature is only relevant for the viscous model, not for the elastic. Thermal flow is not considered, as temperature is constant over all phases.

Viscous creep is a time dependent mechanism, therefore a certain time interval must be defined for the phases. The time interval is set to 15 years per phase, as that is the approximate time it takes for the Groningen gas field to reduce the pore pressure 10MPa. This however, is a very large reservoir, for the smaller reservoirs the depletion rate is much faster, giving a smaller time for a depletion of 10 MPa. This has an impact on the results, as the total deformation of the salt is dependent on the time, unless equilibrium has been reached before the first 5 years. The consequences of this assumptions will be covered in the discussion chapter 7.

For the initialization phase the time is much larger and is set to a significant large number in this case 1e6 days which is large enough to reach equilibrium. There is no difference between in creep between 1e6 and 1e7 days. The time interval only influences models with a time dependent property, such as the N2PC-MC model.

5.3. Output of Plaxis

With the geometry, parameters, assumptions and phases being defined all the models can be run. The results can be visualized in the output program. The results consist of a deformation menu and a stress menu, which can be visualized with the geometry of the model.

5.3.1. Results in 2D

The deformation menu consist of the total and phase displacement and the total and Cartesian strains. The stress menu consist of the total and effective (principal) stresses, the pore pressures, heat and groundwater flow and finally the plastic points. In this report the total strain will be analysed in the horizontal and vertical direction (ε_{xx} and ε_{yy}) and the effective stresses in the horizontal and vertical direction (σ_{xx} and σ_{yy}). The plastic points will also be used as this shows the nodes, in which failure occurs, or for the viscous model which experience creep strain.

The output program also has all the results for all the calculated parameters in tables. These tables will be exported to excel, after which they are imported in python. This allows for calculations with the results and it makes it easier to plot different results next to each other. In python the effective horizontal and vertical stress will be used to calculate the K_0 ratio (Equation 3.8). The viscous and elastic results will also be subtracted from each other, to clearly see where and how the viscous property influences the deformation and state of stress.

5.3.2. Results in 1D

Similar to the results in 2D, there is also a deformation and stress menu for the results along the fault. The deformation menu consist of the fault displacement and the relative displacement between both sides of the fault. The stress menu consist of the total and effective normal stress, the shear stress, the pore pressure and the plastic points. In this project the relative displacement, effective normal stress and shear stress will be used.

The total relative displacement is not always parallel to the fault, except when failure occurs then relative displacement (slip) is parallel to the fault. The relative horizontal and vertical displacements ($u_{x,rel}$ and $u_{y,rel}$) are used and projected to the on the fault using the following equation:

$$u_{rel} = u_{y,rel} \cos \frac{20}{180} \pi + u_{x,rel} \cos \frac{70}{180} \pi \quad (5.3)$$

In which, 20 is the angle between vertical and the fault and 70 the angle between horizontal and the fault.

The effective normal stress and shear stress are used to calculate the Shear Capacity Utilization given by the following equation:

$$SCU = \frac{\tau}{C + \sigma_n \mu} \quad (5.4)$$

If $SCU < 1$ the failure strength has not yet been reached and the element is responding elastically. If $SCU = 1$, the fault element has reached the failure criterion and deforms (slips) plastically (Buijze et al., 2017). The friction coefficient μ is equal to the static friction coefficient μ_s until failure has reached, where it decreases to the dynamic friction coefficient μ_d . In the plotting script the static friction coefficient decreases to the dynamic friction coefficient if the relative displacement is larger then 5mm (equal to the critical slip distance in Buijze et al. (2017)). For simplicity, the dynamic friction coefficient μ_d will be set equal to the 0.3 (μ_d of SS) for all fault sections. The static friction coefficient will be different for the fault section according to Table 5.4.

6

Results

In this chapter the results of the geomechanical model simulations will be discussed. As discussed in the previous chapter, the results contain the strain deformation and the effective stresses around the fault. As well as the effective normal and shear stress acting on the the fault, including the calculated SCU and the (a) seismic slip.

The results will help answering the research questions proposed in the introduction.

The type of reservoir, depth and offset of the model might be abbreviated in this chapter to the following:

Carbonate (C), Rotliegend (R), Shallow (S), Deep (D), 1/4 relative offset (1) and 3/4 relative offset (3). For example: The Rotliegend deep model with an offset of 3/4 will become RD3. If the Rotliegend models with an offset of 1/4 are meant without the specifying the depth, this will give R1. The Carbonate shallow model becomes CS.

First of all, the 2D results of the strain will be given in the Section 6.1.1. This section is followed by Section 6.1.2, covering the stress results in 2D. Section 6.2, discusses the stresses acting on the fault. A small summary will be given in Section 6.3

All these sections present the result, first comparing the viscous model with the elastic model for each model separately. At the end of each section, there is a reservoir comparison, in which the difference between the Carbonate, Rotliegend 1/4 and Rotliegend 3/4 are covered. In the end Section 6.2.4, analyses the fault reactivation of the models, using both 2D and 1D results.

6.1. 2D results around fault zone

The 2D strain and stress results can be found in this section. For both the deformation and stress sections, the Carbonate shallow results are plotted for every depletion phase, to see the change in strain/stress over depletion and the difference before and after the initialization phase. Because of the large amount of figures and because the depletion pattern is more or less similar for all different models, the results for the other models (CD and R) will only be shown for $\Delta P = 20\text{MPa}$ ($P_{p,shallow} = 15\text{MPa}$ and $P_{p,deep} = 30\text{MPa}$). The results for all phases of the other models can be found in appendix C.

6.1.1. Deformation

Carbonate models

As mentioned in Section 4, stress points which produce creep strain are displayed as "cap points" in Plaxis Plaxis (2022) output. For the viscous Carbonate Shallow model the cap points are given in Figure 6.1 for the phase after initialisation and the final phase. Only these two phases are shown, as there is no strain before initialization, therefore no creep points and in the other phases the cap point cloud is just growing till the final phase, which is shown. It can be seen that after initialization, but before depletion (left figure), points already experience creep strain. The cap points are mainly centered around the fault and above the hanging wall next to the footwall. With the depletion of the

ZEZ2C reservoir, the creep points are spreading out away from the fault.

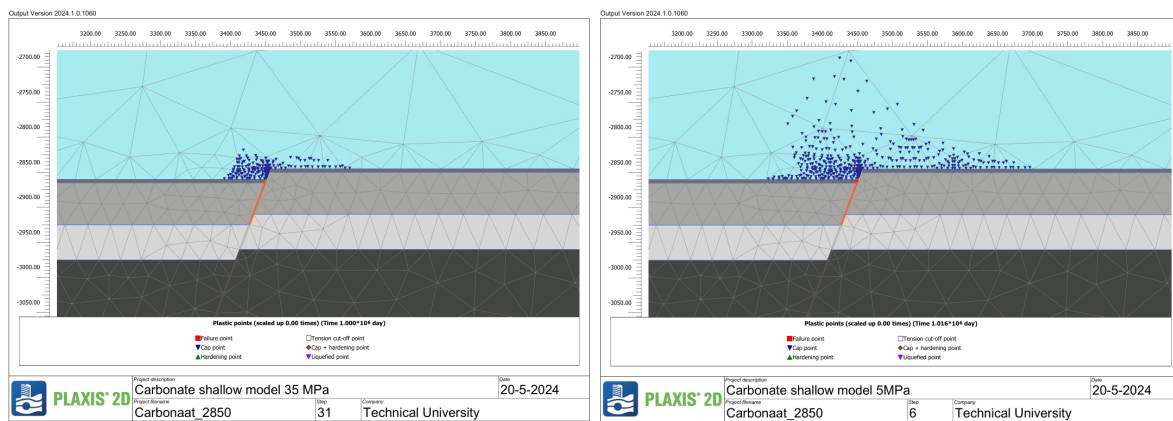


Figure 6.1: Plastic points for the phase after initialisation, before depletion and the final phase of the Carbonate Shallow model. The cap points are considered as the viscous creep points.

The cap points only show the points experiencing creep strain, not the amount of strain. The actual strain can be subdivided into the horizontal and vertical strain. The horizontal and vertical strain for the Carbonate Shallow model are shown in Figures 6.2 and 6.3. The strain is plotted for the elastic and viscous model, as well as the difference between the two models.

The location where strain is taking place and the direction of the strain is similar for the elastic and viscous models and is increasing with depletion. For the horizontal strain, the strain is mainly located where the reservoir is being juxtaposed to a different layer.

For the vertical strain the reservoir shows the largest strain values, due to the compaction. The larger the depletion, the larger the compaction and the larger the strain. There is also some strain in the layers juxtaposed to the reservoir, with the same direction as the reservoir compaction.

Even though the location and direction of the strain is similar for the elastic and viscous model, the amount of strain is significantly higher for the viscous model. The horizontal strain in the halite in particular is about twice as high for the viscous model compared to the elastic model, which is clearly visible in the difference plot at the bottom of Figure 6.2. The increase in strain with the viscous property in the halite also influences the strain on the other side of the fault, however not as strongly as in the halite. The impact of the viscous property is limited in the layers below the halite.

The viscous property has a similar influence on the vertical strain as for the horizontal strain. In the reservoir, juxtaposed to the halite, the difference in vertical strain becomes more negative. Hence, more compaction is taking place in the reservoir for the viscous model.

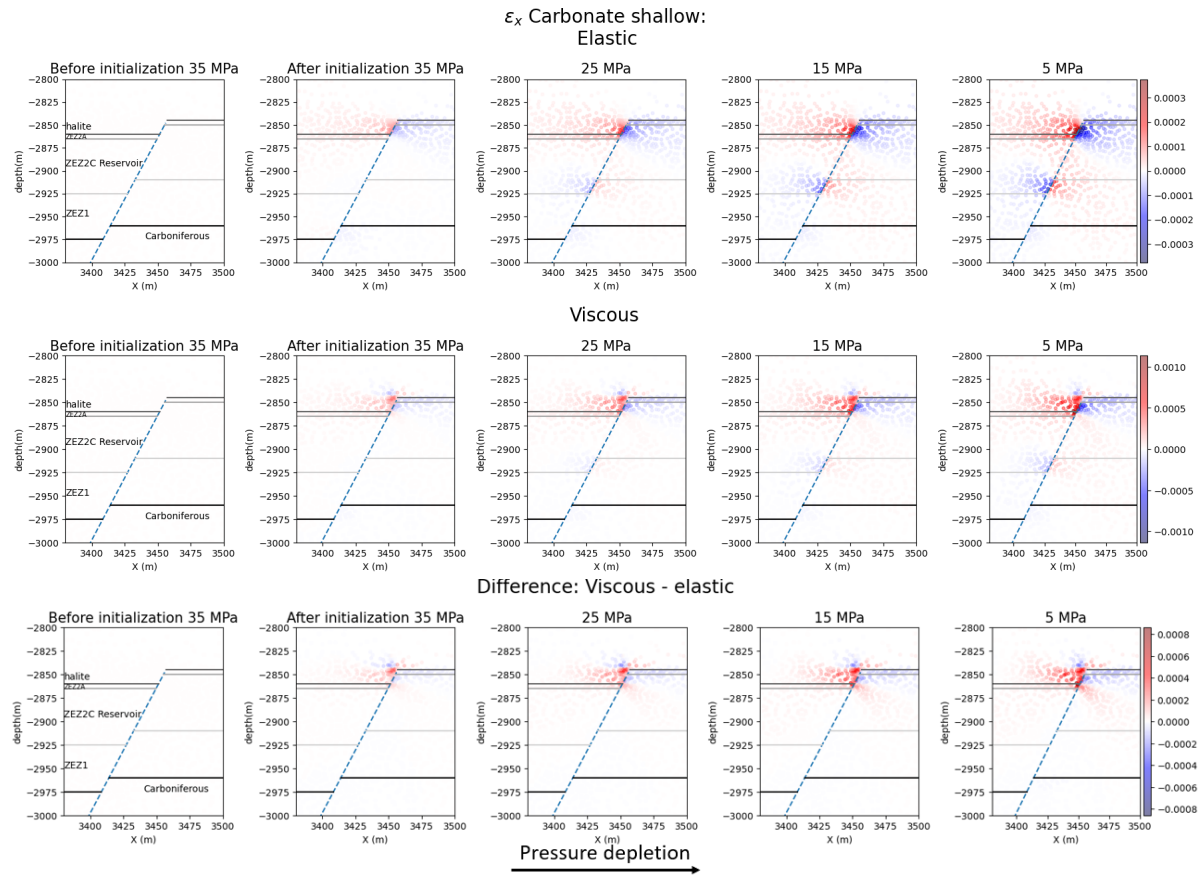


Figure 6.2: Total cartesian strain in the x direction for the Carbonate shallow model. The top row corresponds to the case in which the halite is modelled elastically. The middle row corresponds to the viscous case and the bottom row is the difference between the viscous and elastic models (second row minus first row). The pressure depletion is from left to right.

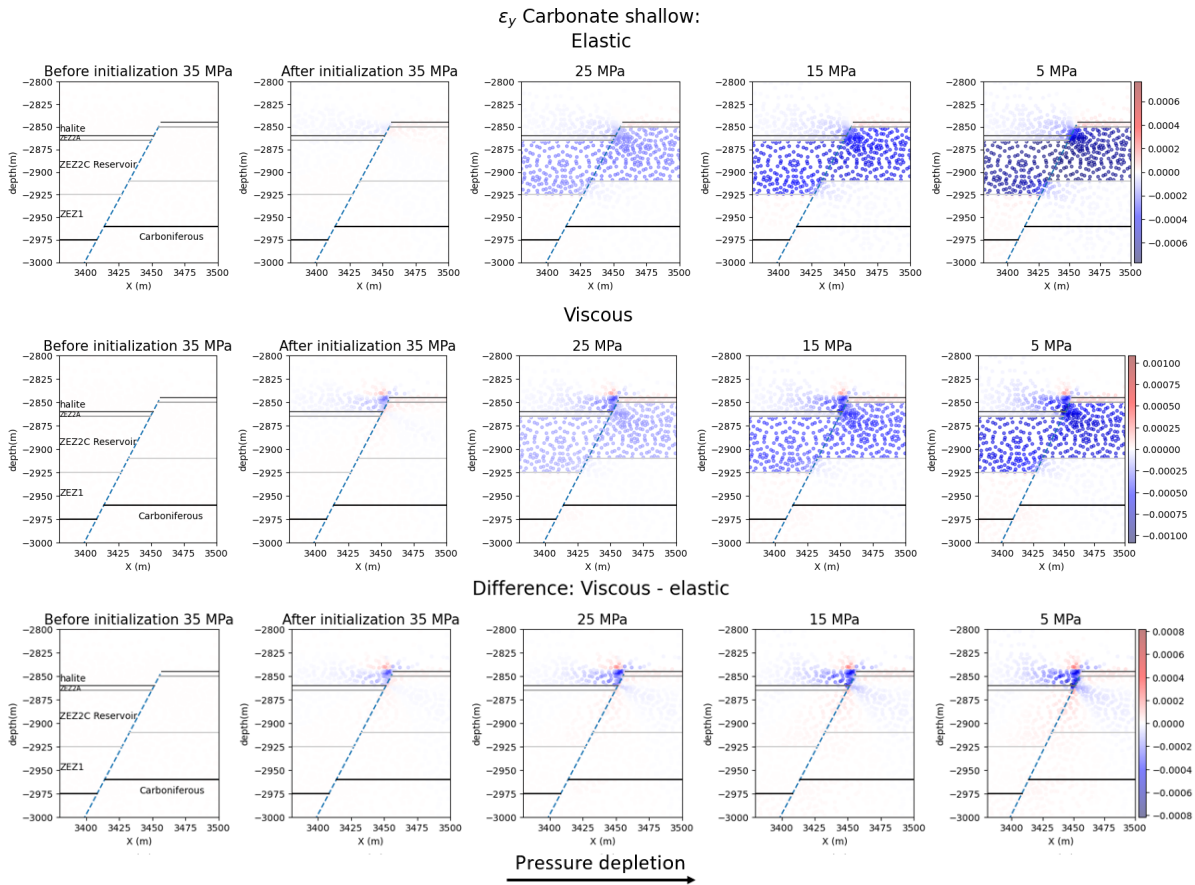


Figure 6.3: Total cartesian strain in the y direction for the Carbonate shallow model. The top row corresponds to the elastic case, the middle row to the viscous case and the bottom row is the difference between the viscous and elastic models (second row minus first row). The pressure depletion is from left to right.

Figure 6.4, shows the horizontal and vertical strain for the Carbonate Deep model at 30MPa. Similar to the Shallow model the total strain and the difference between the viscous and elastic is largest in the halite layer. The viscous model also gives a more negative vertical strain in the reservoir juxtaposed and thus more compaction. On the other hand, below the halite around the fault, the strain becomes red in the difference plot. This indicates that the strain is less negative and less compaction is taking place in the reservoir here.

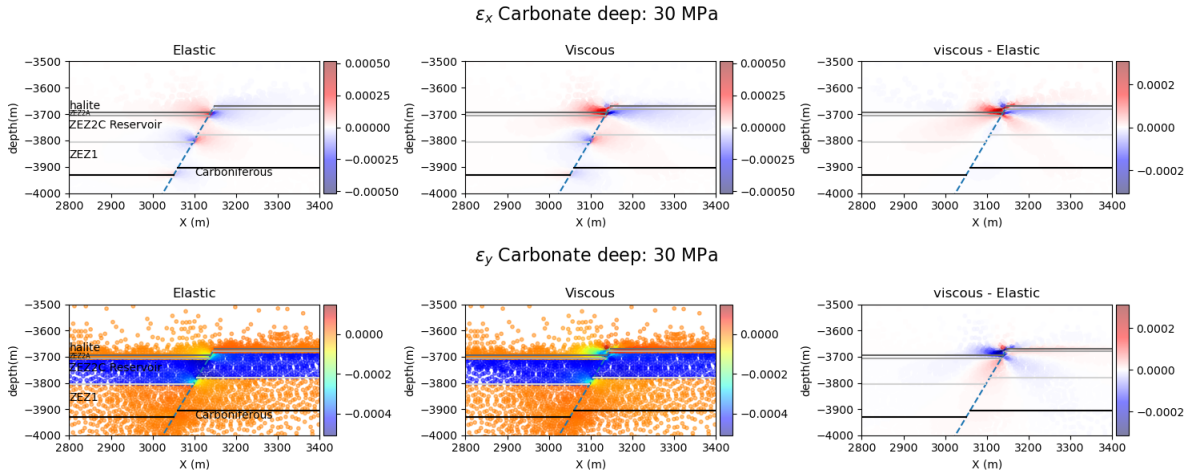


Figure 6.4: Total cartesian strain in the x and y direction [-], for the Carbonate deep model. The strain is given for the elastic and viscous model and the difference between the two. A negative x strain means strain directed to the left and a positive strain means strain directed to the right. A negative y strain means strain directed towards the bottom and a positive strain is directed to the surface.

Rotliegend models

The horizontal and vertical strains for the Rotliegend models at a depletion of $\Delta P = 20$ can be found in Figures 6.5, 6.6, 6.7 and 6.8. The RS1 and RD1 models show similar patterns and magnitudes. The largest horizontal strain (up to 0.005) is not located in the halite, but at the reservoir juxtaposition with the Ten Boer and Carboniferous layer. The vertical strain reaches up to compaction values of -0.0015 in the reservoir.

When comparing the elastic with the viscous model, the elastic model shows limited strain in the halite, however with the viscous property this increases. This is also visible in the difference plots, for both the horizontal and vertical strain. In the Slochteren reservoir and the Ten Boer layers around the fault, the vertical strain is slightly larger (positive) for the viscous model compared to the elastic model. Hence there is slightly less compaction in the reservoir around the fault with the viscous property.

When comparing the difference plot on the right of the RS1 and RD1 models, it can be seen that the difference is slightly larger for the deeper model compared to the shallower model. The reddish area in the halite layer in the horizontal strain plot and the blueish area in the vertical strain plot is slightly darker for the deeper model compared to the shallower model.

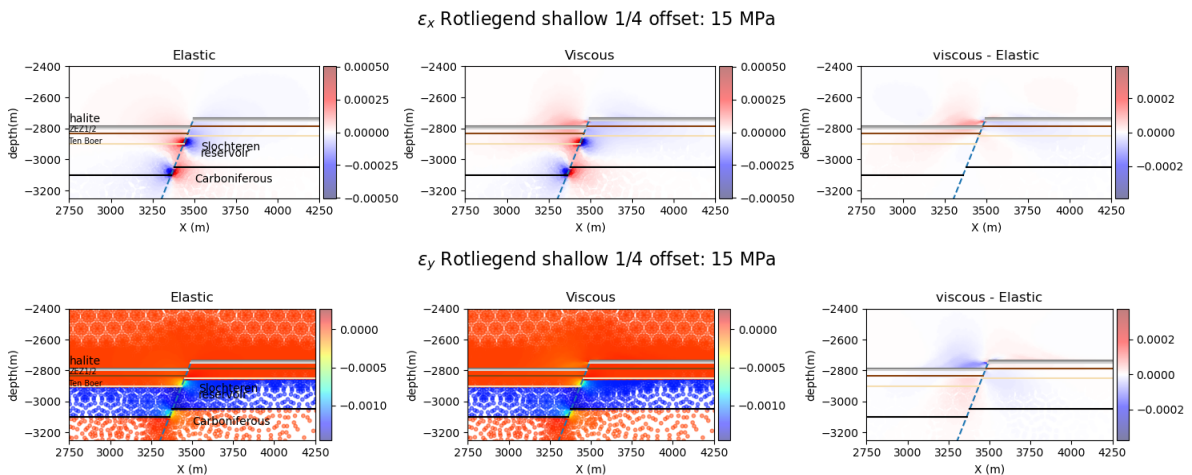


Figure 6.5: Total cartesian strain in the x and y direction [-], for the Rotliegend shallow model with a relative reservoir offset of 1/4.

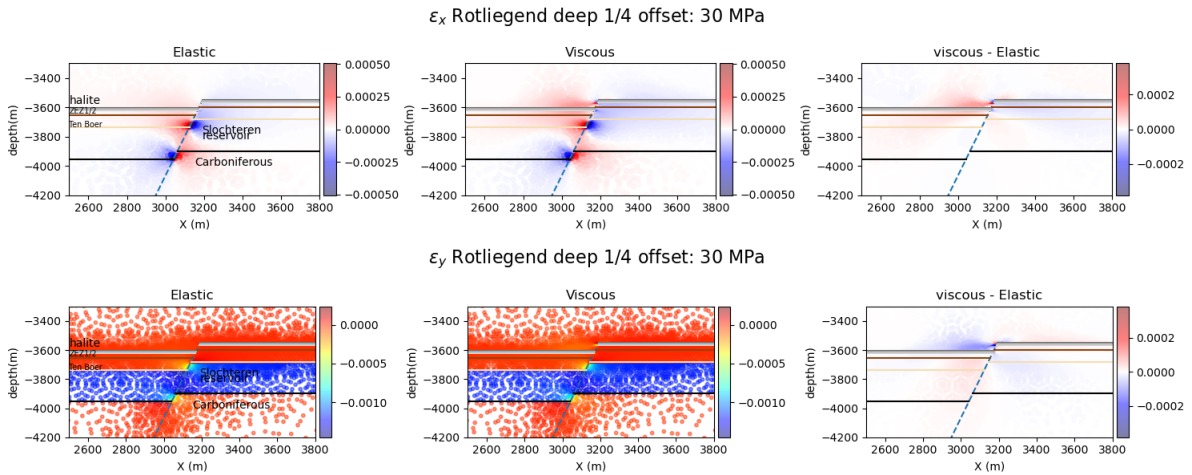


Figure 6.6: Total cartesian strain in the x and y direction [-], for the Rotliegend deep model with a relative reservoir offset of 1/4.

For the RS3 and the RD3 models (figures below) both the horizontal and vertical strain reaches up to values of (-)0.002. For the elastic model the horizontal strain is mainly located at juxtaposition with the reservoir and a different layer. With the viscous property the amount of strain changes mostly in the halite and the juxtaposition with the reservoir. When comparing the difference plot of the shallow and deep models, it can be seen that both show differences of about 0.002. Hence, the difference between the deeper models is not visible in this plot.

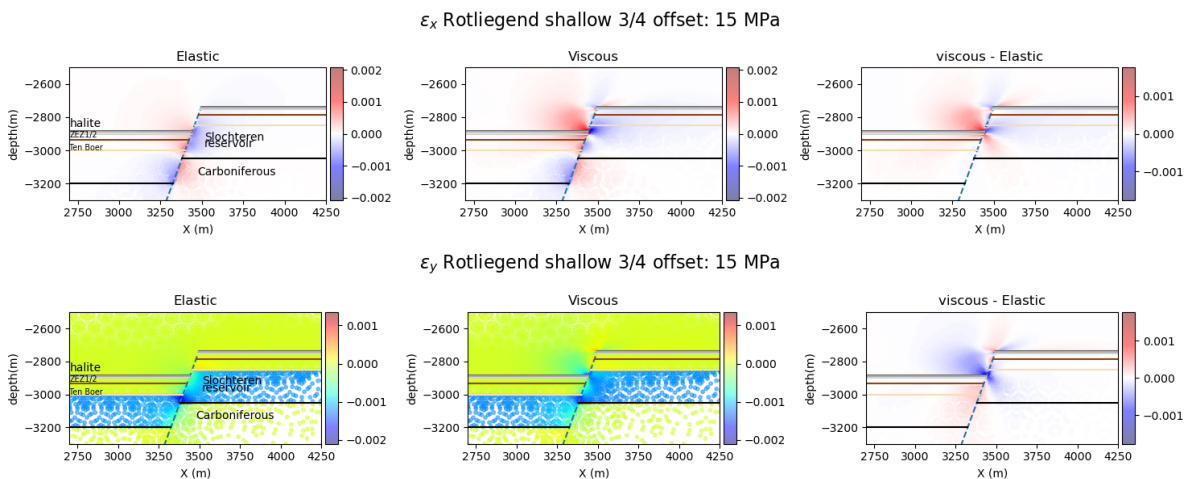


Figure 6.7: Total cartesian strain in the x and y direction [-], for the Rotliegend shallow model with a relative reservoir offset of 3/4.

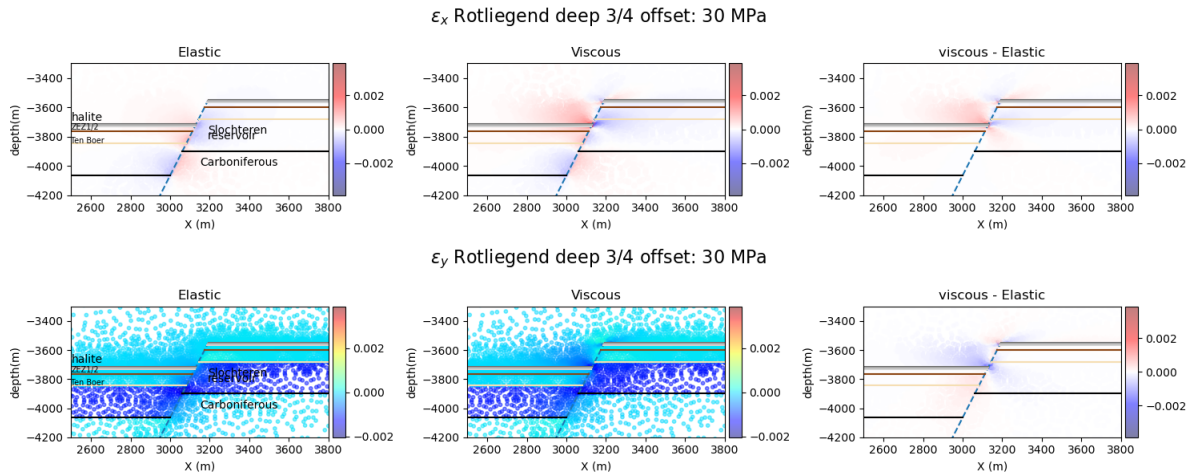


Figure 6.8: Total cartesian strain in the x and y direction [-], for the Rotliegend deep model with a relative reservoir offset of 3/4.

Reservoir comparison

As discussed above, there is limited difference in strain behaviour between the shallow and deep model. However, there are significant differences between the Carbonate, R1 and R3 models. The R3 models show much larger maximum strains (4 times) as the C and R1 models, which have more or less similar strain magnitudes. For the vertical strain the R3 models also have the largest maximum strain. However, the R1 models does show a significantly larger vertical strain compared to the C models. This is because the elastic properties of the Slochteren reservoir and the ZEZ2C reservoir are different. The ZEZ2C is more resistant to deformation (larger Young's modulus), giving a smaller compaction. The horizontal strains (in magnitude) are similar for the R1 and C, because the juxtaposition of the halite with the reservoir in C compensates for the larger resistance against deformation.

With the presence of the viscous property the strain increases mainly in the halite for all models, amplifying the strain of the elastic models. For the Carbonate and R3 models this increase in strain is largest, due to the juxtaposition of the halite to the reservoir. The viscous property has similar effects on the horizontal strain as for the vertical strain, the strain is mainly increased in the halite and juxtaposed to the halite. For the vertical strain the compaction in the reservoir becomes larger directly juxtaposed to the halite, but slightly smaller below the halite around the fault.

6.1.2. Effective stresses and K_0 ratio

Carbonate models

This section will cover the K_0 results in the same window as the deformation results. For the K_0 the effective horizontal and vertical stress are needed (Equation 3.8). The effective horizontal and vertical stresses have been plotted, as well as the K_0 for every phase of the Carbonate Shallow model in Figures 6.9, 6.10 and 6.11. For the other models the K_0 results are only shown for depletion pressure of 20MPa, the K_0 figures per phase for the other can be found in Appendix C.

An important thing to notice is that the stresses are negative, meaning that if the stress becomes more negative, the stress becomes larger.

As can be seen in Figures 6.9 and 6.10 is that the effective stresses in the halite are significantly higher then in the other layers, due to the absence of a pore pressure in that layer. With the decreasing pore pressure in the reservoir the effective stresses are also increased. The increase in vertical stress is larger than the increase in horizontal stress, giving a decrease in K_0 in the reservoir as can be seen in Figure 6.11 (in agreement with poro-elasticity).

In the layers next to the reservoir the effective horizontal stress decreases over the depletion. On the other hand, above the reservoir the horizontal stress is slightly increasing. The vertical stress shows the opposite pattern as the stress slightly increases next to the reservoir and slightly decreases above the reservoir. The decrease in horizontal and increase in vertical stress next to the reservoir results in a clear decrease in K_0 over depletion as can be seen in Figure 6.11 (tendency of normal faulting).

Whereas above the reservoir the K_0 increases. These changes are in agreement with the theory explained in Section 3.2.3 (Figure 3.6).

From Figure 6.9, it can be seen that for the elastic model the effective horizontal stress decreases in the halite juxtaposed to the reservoir, whereas it remains constant in the viscous model. This results in a negative difference (red) in stress in the difference plot, meaning that the stress is larger in the for the viscous model. The stress is also larger in the layer juxtaposed to the halite for the viscous property compared to the elastic property. On the other hand in the layers directly below the halite the horizontal stress is lower for the viscous property.

For the vertical effective stress, the difference in stress is lower in the halite for the viscous model. As the stress becomes higher over depletion for the elastic case and does not change for the viscous model. Juxtaposed to the halite the vertical stress is larger for the viscous property.

The results from the effective horizontal and vertical stress difference between the elastic and viscous models can also be found in the K_0 difference plot. The K_0 remains constant at 1 for the viscous model, whereas for the elastic model it becomes lower in the halite. In the reservoir next to the halite the K_0 increases for the viscous model, whereas directly below the halite the K_0 decreases for the viscous model. When going further down at the difference in stress ratio becomes positive (red) in the reservoir around the fault, meaning that the K_0 is larger for the viscous model and move away from criticality.

Another important thing to notice is that with the initialization, the effective horizontal stress and consequently the K_0 is already different compared to before the initialization. There is already a difference between the elastic and viscous model after the initialization. In the Carbonate Shallow plots it is not very significant, but when looking at the Rotliegend models with a relative offset of 3/4, the difference in initialization is very clear (see appendix).

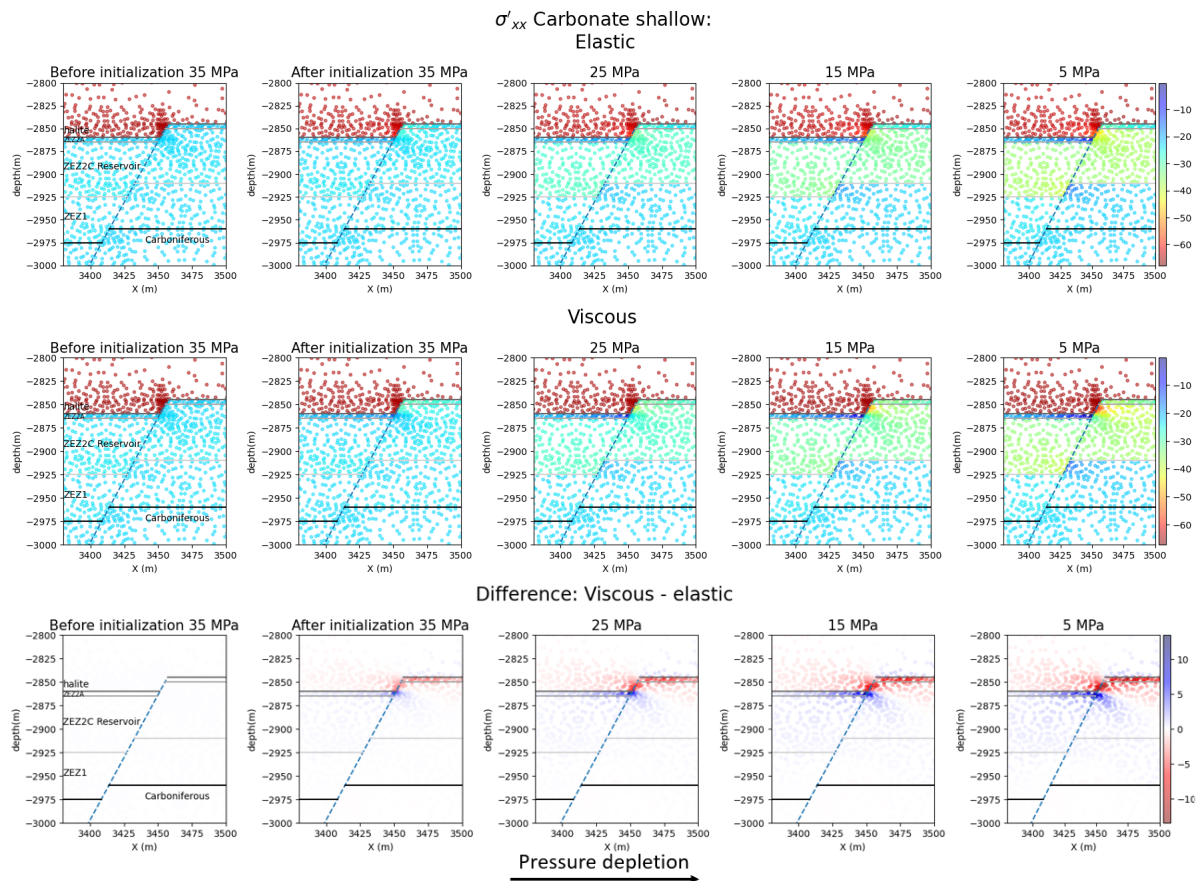


Figure 6.9: Effective horizontal stress for the Carbonate shallow model. The top row corresponds to the elastic case, the middle row to the viscous case and the bottom row is the difference between the viscous and elastic models (second row minus first row). The pressure depletion is from left to right.

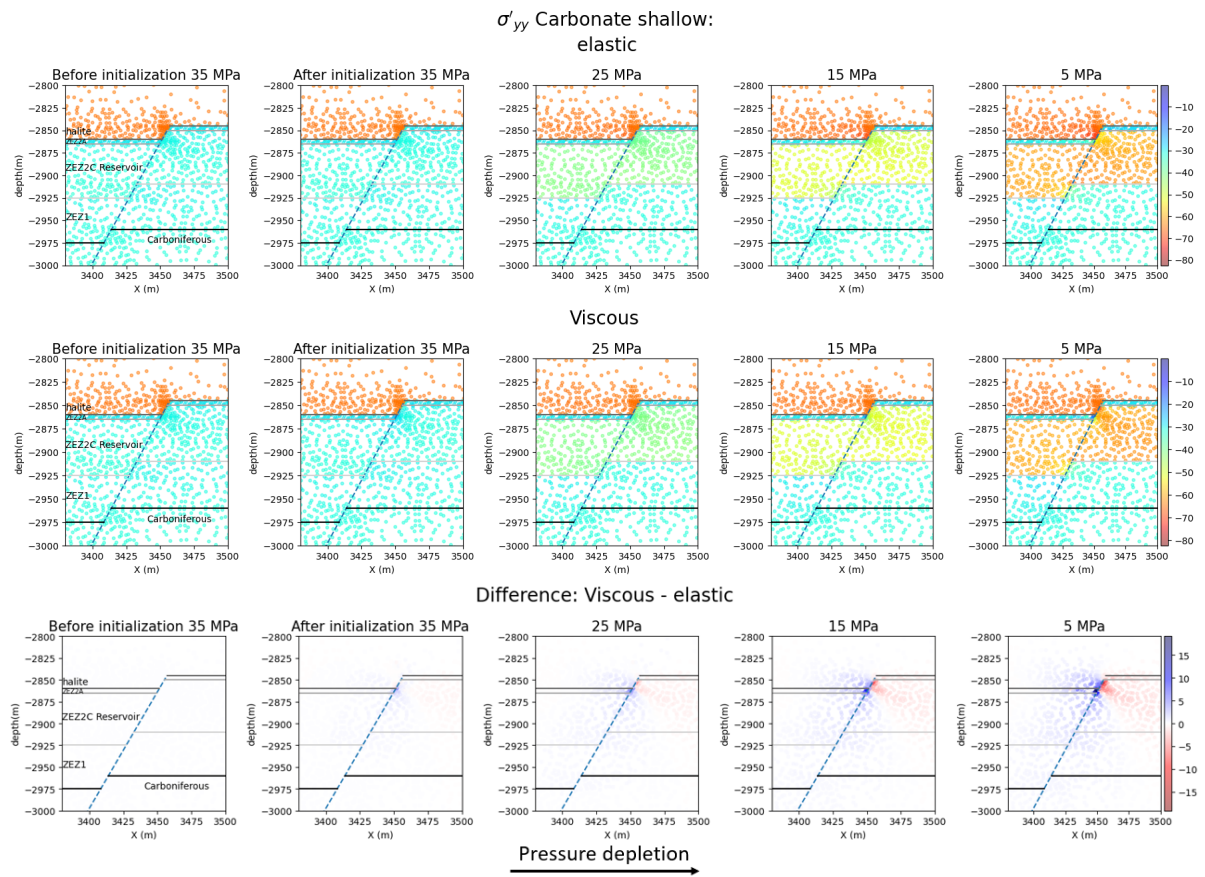


Figure 6.10: Effective vertical stress for the Carbonate shallow model. The top row corresponds to the elastic case, the middle row to the viscous case and the bottom row is the difference between the viscous and elastic models (second row minus first row). The pressure depletion is from left to right.

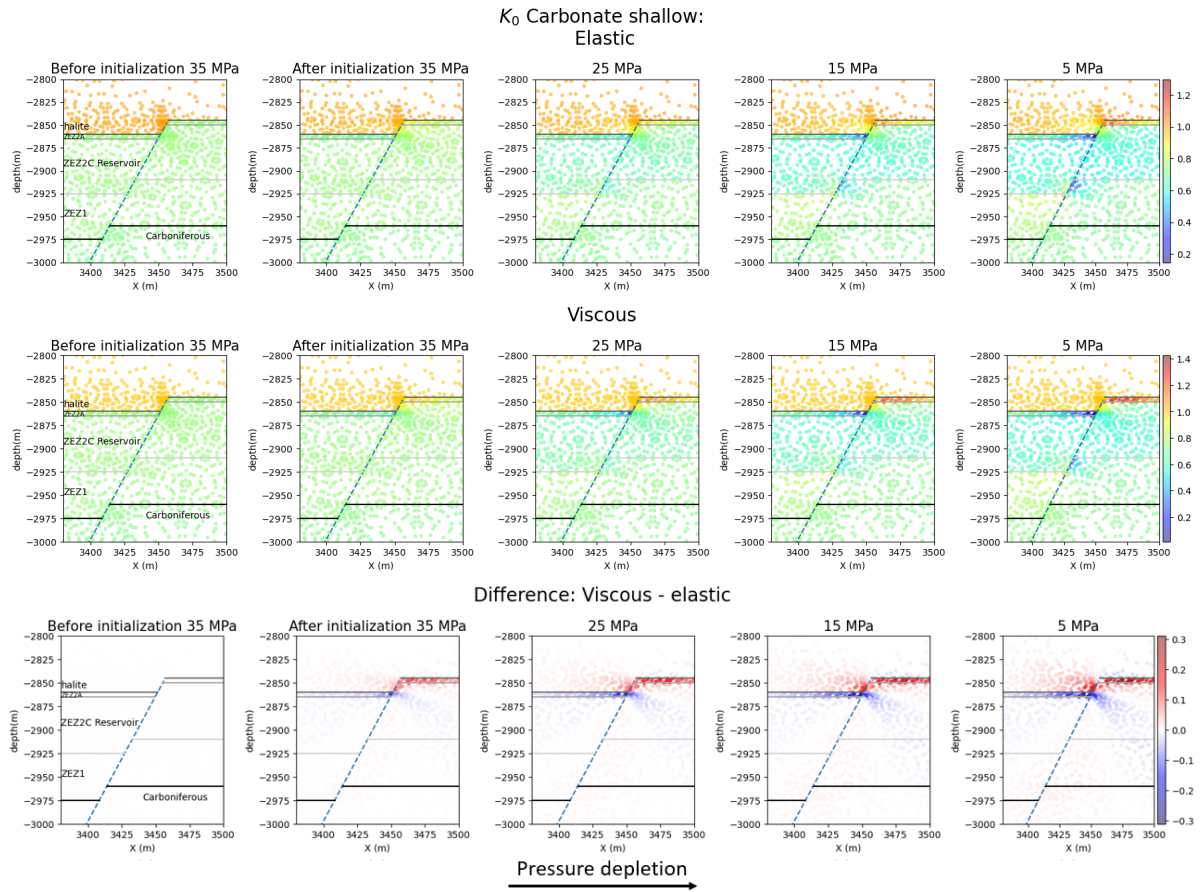


Figure 6.11: K_0 ratio for the Carbonate shallow model. The top row corresponds to the elastic case, the middle row to the viscous case and the bottom row is the difference between the viscous and elastic models (second row minus first row). The pressure depletion is from left to right.

For the Carbonate deep model the K_0 is plotted at the reservoir pressure of 30MPa in Figure 6.12. It can be seen that the stress ratio has become lower compared to its initial phase in the reservoir (0.65) and in the layers juxtaposed to the reservoir.

Above the reservoir in the footwall the K_0 has increased. The lowest value (0.2) can be found just below the halite in the ZE22A layer near the fault, where the stress has significantly be reduced with the viscous property. With the viscous property the ratio in the halite is not being decreased and the changes described above are amplified in the layers surrounding the halite. For the reservoir, the deeper and closer to the fault the ratio is larger for the viscous model, whereas further away the viscous model gives smaller ratios.

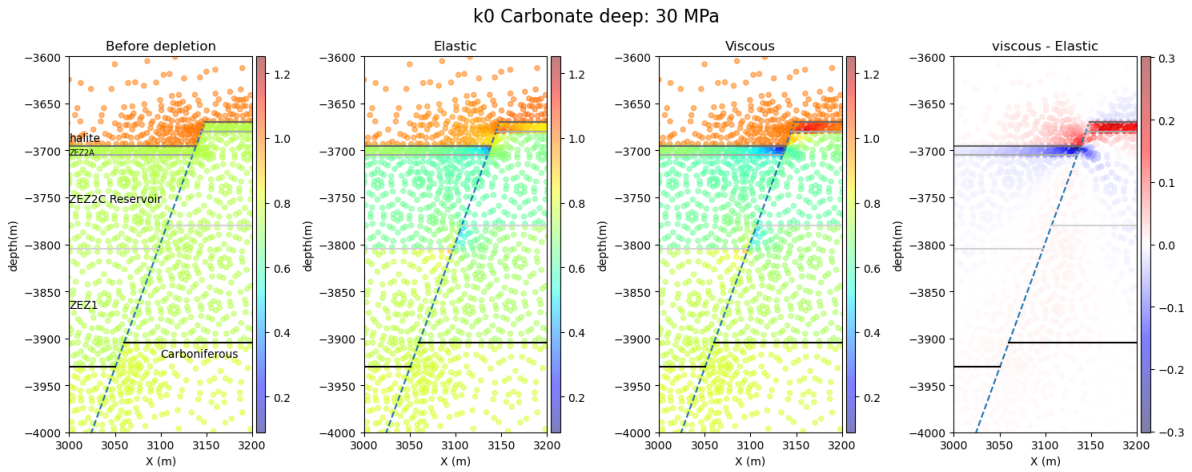


Figure 6.12: K_0 ratio for the Carbonate deep model

Rotliegend models

For the Rotliegend models the K_0 has also been plotted at a depletion of $\Delta P = 20MPa$. The RS1, RD1, RS3 and RD3 models can be found respectively in Figures 6.13, 6.14, 6.15 and 6.16. It can be seen that for all the Rotliegend models the ratio in the reservoir drops to 0.5-0.6 near the fault for both the elastic and viscous case. The ratio is also decreased with respect to the initial reservoir pressure in especially the Basal Zechstein layers in the hanging wall and in the layer (TB or SS) juxtaposed to the Basal Zechstein layers. The Basal Zechstein layers in the foot wall gives an increase in ratio. When comparing the elastic to the viscous model, it can be seen that the changes in stresses are amplified in the Basal Zechstein layers. Due to the large horizontal stresses in the halite, the ratio is further decreased with the viscous property in the BZ layers in the hanging wall and for the foot wall the ratio is further increased. An important note is however that this differences is strongest away from the fault. The closer to the fault the closer the difference becomes to zero.

The Rotliegend models with 1/4 offset show the largest difference between the elastic and viscous model in the Basal Anhydrite layer, reaching values up to 0.10. The difference in the halite layer is limited to (0.04).

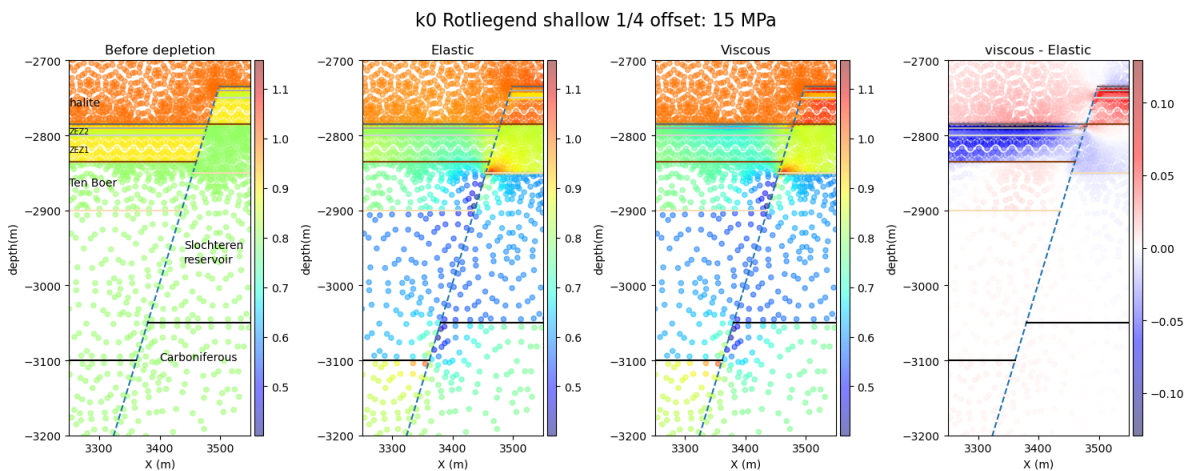


Figure 6.13: K_0 ratio for the Rotliegend shallow model with a relative reservoir offset of 1/4

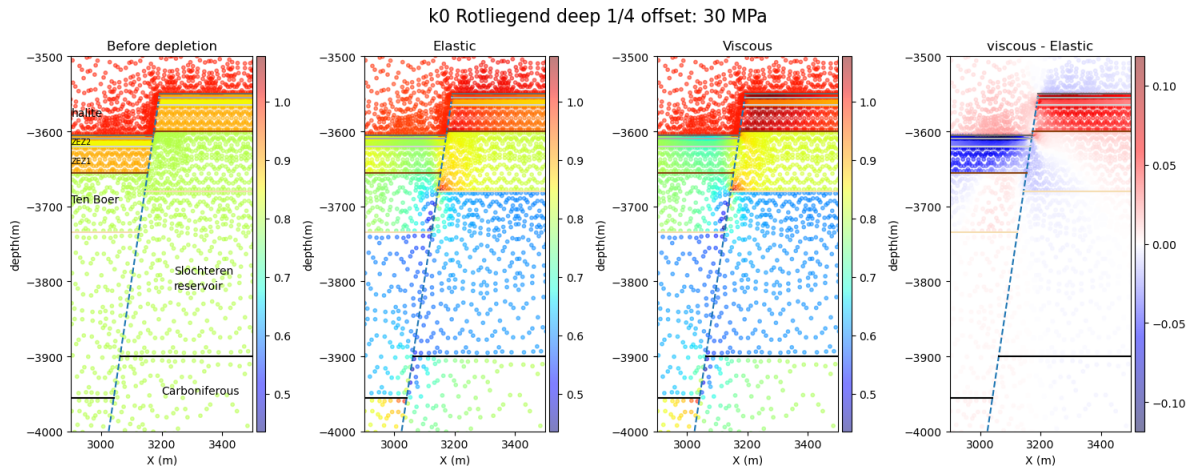


Figure 6.14: K_0 ratio for the Rotliegend deep model with a relative reservoir offset of 1/4

For the Rotliegend models with an offset of 3/4, the difference in ratio between the elastic and viscous model in the halite reaches up to about 0.3. Which is almost equal to the difference in the Basal Zechstein layers. For the reservoir, the difference between the elastic and viscous models is positive in around the fault and negative further away from the fault. Meaning that the viscous property gives higher stress ratios in the reservoir around the fault and lower values away from the fault.

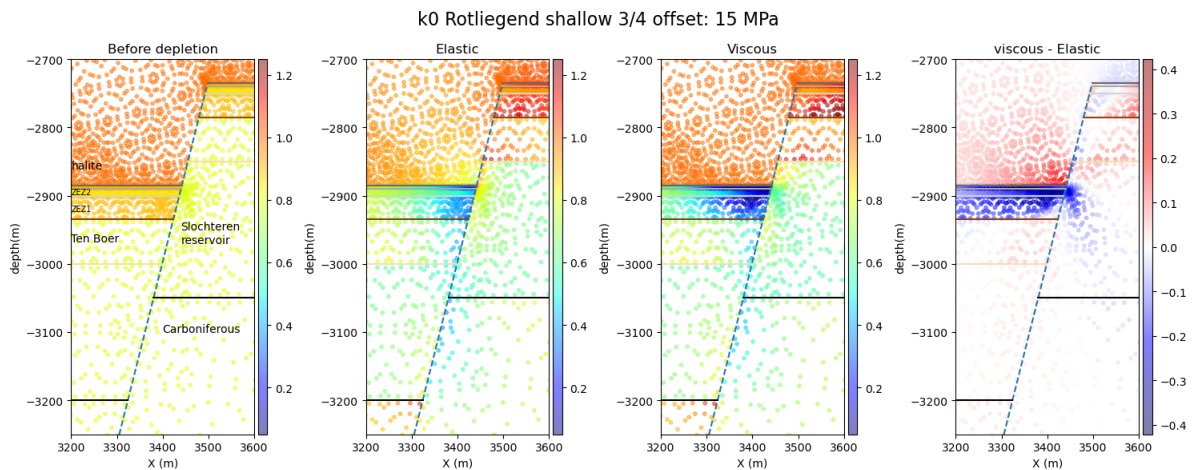


Figure 6.15: K_0 ratio for the Rotliegend shallow model with a relative reservoir offset of 3/4

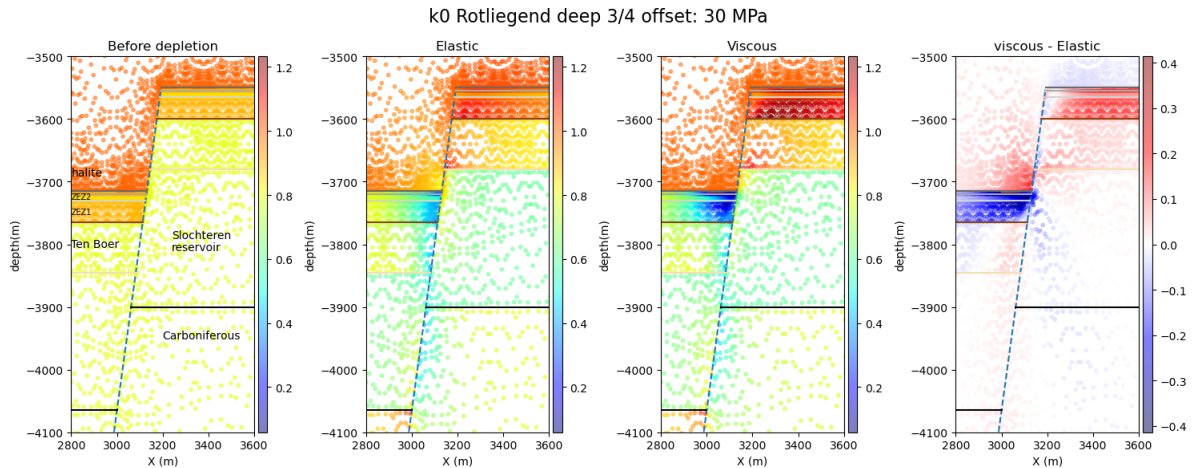


Figure 6.16: K_0 ratio for the Rotliegend deep model with a relative reservoir offset of 3/4

Reservoir Comparison

The overall depletion pattern is equal for all models. The stress ratio is being reduced in the reservoir and the layers juxtaposed to the reservoir, promoting normal faulting. Whereas it is increased above and below the reservoir, moving the fault away from criticality.

The viscous property prevents the stress ratios from decreasing in the halite, giving larger values. The large effective horizontal stresses in the halite, decreases the stress ratio in the layers directly below even more. Especially at the fault this results in very low stress ratio's, which may result in dilation of the fault and tension near the fault and consequently fault intrusion, however the dilation is not proven with these results. In the reservoir, the stress ratio is slightly larger for the viscous model, this is significantly lower than the difference in the other layers. But it does move the fault away from criticality there.

When comparing the different models it can be seen for all the models that the difference between the shallow and deep models is more or less similar. On the other hand there are some differences between the Carbonate, Rotliegend 1/4 and Rotliegend 3/4 models.

The depletion in the Rotliegend model result in a larger stress ratio decrease in the reservoir then for the Carbonate model (-0.3 for the Rotliegend and -0.1 for the Carbonate). This is due to the poro-elasticity which is dependent on the Poisson's ratio, which is larger for the Carbonate layer (giving smaller difference in stress increase).

The stress ratio at $\Delta P = 20 MPa$ is the smallest in the layers below the halite in the Carbonate and the R3 models, reaching values of $K_0 = 0.1 - 0.2$. Whereas for the R1 models this is limited to $K_0 = 0.6$. This shows that if the halite is not juxtaposed to the reservoir the changes are limited for both the elastic and viscous models compared to when the halite is juxtaposed to the reservoir. This can also be seen in the difference between the elastic and viscous models. The differences are much larger (up to 0.4) for the Carbonate and the R3 models then for the R1 models (maximum difference of 0.10).

When comparing the Carbonate and R3 models, it can be seen that they do show some differences due to the thickness of the layers in between the reservoir and halite. For the Carbonate only the ZEZ2A layer (5m) separates the halite from the reservoir, whereas for the Rotliegend there are multiple layers (up to 130m thick for RD model). This gives a larger area with very low stress ratio, which can potentially lead to normal shear slip.

6.2. 1D results along fault

In this section the effective horizontal and shear stresses acting on the fault are plotted. To recall it is expected that the effective normal and shear stress plots show a similar pattern as in Figure 3.7. The relative shear slip between both sides of the fault is also plotted as well as the calculated SCU value.

6.2.1. Carbonate models

The Carbonate shallow plots are given in Figures 6.17 and 6.18. As can be seen the pore pressure is being reduced from its initial value to the final depletion pressure. The pore pressure is constant over the whole reservoir and spans over all the fault section connected to the reservoir except for the juxtaposition with halite. For halite the pore pressure is zero and for the underburden it decreases with depth from the initial pore pressure.

The effective horizontal stress increases in general with depletion. The larger the depletion the larger the peaks of the reservoir juxtaposition with a different layer become. The curve is as expected, however where the halite is the stress is significantly larger. This is due to the absence of pore pressure in the halite. For the elastic model the normal stress is decreasing with depletion, whereas for the viscous model the stress remains constant in the halite. This is expected when looking at the 2D results, where the effective horizontal stress was decreasing for the elastic model in the halite and for the viscous property this remained constant.

For the shear stress the plot is as expected, with highest values in the reservoir sections of the fault and peaks in the opposite direction at the outer boundaries of the reservoir. The high pore pressure in the halite does not impact the shear stress as the shear stress is independent of the pore pressure. When comparing the elastic to the viscous model it can be seen that the shear stress in the viscous model remains around the initial value in the halite with a peak at the bottom halite boundary. Whereas for the elastic model the shear stress increases with depletion.

For both models there is some slip, however this very limited and is not considered as (a) seismic shear slip. As the slip is also not parallel to the fault (not visible in this plot) and there is no failure in the fault. This is also shown in the SCU plot, where the curve does not reach a value of 1.

The shallow and deep model curves are almost similar, except for the larger pore pressures and effective normal stresses, due to the larger depth.

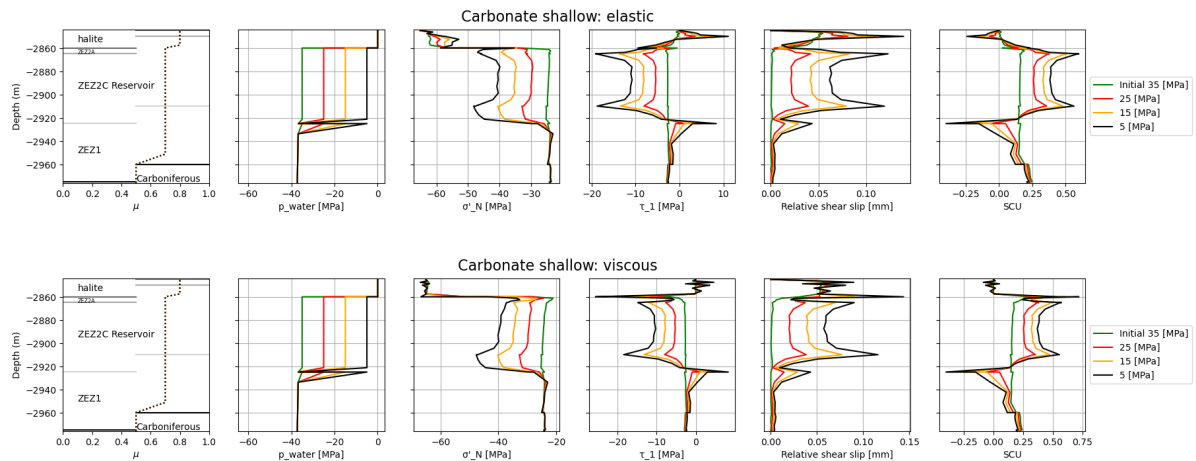


Figure 6.17: Results along the fault for the Carbonate shallow model with the depth on the Y-axis. On top the results are given where the Zechstein halite is modelled with Elastic properties and at the bottom with viscous properties. The first figure shows the geometry of the layers along the fault, with the corresponding μ value for the different phases. The other figures show from left to right the Pore pressure, effective normal stress, shear stress, relative shear slip and the calculated SCU along the fault.

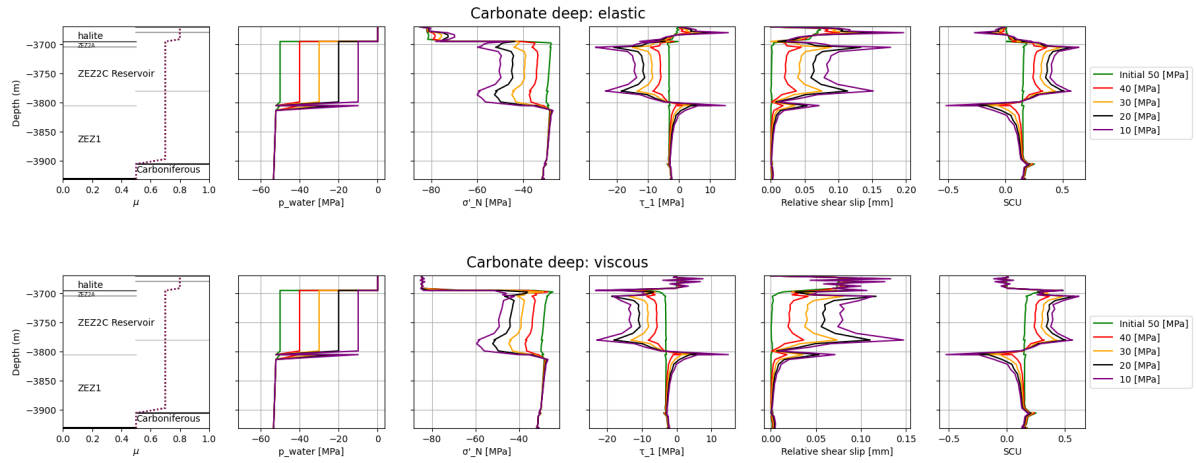


Figure 6.18: Results along the fault for the Carbonate deep model.

6.2.2. Rotliegend models 1/4 offset

The deep and shallow Rotliegend models with a relative reservoir offset of 1/4 are given in Figures 6.19 and 6.20. The pore pressure starts at the top with zero, after which it increases with depth to the hydrostatic pressure with the overpressure defined in Section 5.2.4. The reservoir has a constant pressure and is depleting per phase. Below the reservoir the pressure is increasing again with depth. The normal effective stress is highest in the halite part of the fault and lowest below the halite and above the reservoir.

For the shear stress the larger stresses in the reservoir behave as expected. However for the phases with a $\Delta P \geq 30$ a peak disappears at one or both of the inner reservoir boundaries with a different formation, the area between the peaks also becomes more irregular. When looking at the relative shear slip there are one or two peaks with a significant (a) seismic shear slip, matching the location of the missing peaks of the shear stress. At these slip boundaries the friction coefficient is being reduced due to failure to the dynamic friction coefficient. The corresponding SCU value with the decreasing friction coefficient equals a value of 1.0.

When comparing the elastic with the viscous models it can be seen that the elastic model has an extra slip location for the shallow model at $P = 5 \text{ MPa}$ ($\Delta P = 30 \text{ MPa}$). Also the amount of slip is larger in the elastic model than the viscous model. Where the slip is missing in the viscous model compared to the elastic model it can be seen that the SCU value almost touches one, meaning failure is close. For the deep model the relative shear slip curve does not show any peak in the viscous model at $\Delta P = 30 \text{ MPa}$ ($P = 20 \text{ MPa}$). The reason that the shallow model does show a peak, whereas the deep model does not can be because of the viscous property. Which can have a slightly larger impact at a reservoir, which is located deeper than shallow, due to the difference in behaviour. As mentioned before, the difference in behaviour at depth is not very large with the used model, however, this can just be enough to produce slip or not. It was also mentioned in section 5.2.1, that the K_0 that is used for the deep model is slightly larger than calculated. If the lower K_0 would be used, this would give a larger likelihood of slipping and peaks may be visible.

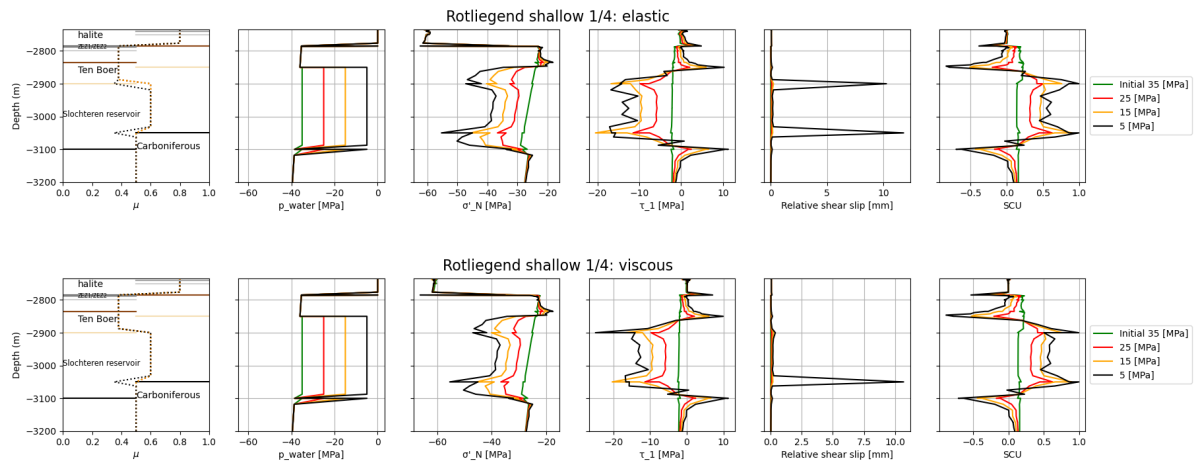


Figure 6.19: Results along the fault for the Rotliegend shallow model with a relative reservoir offset of 1/4.

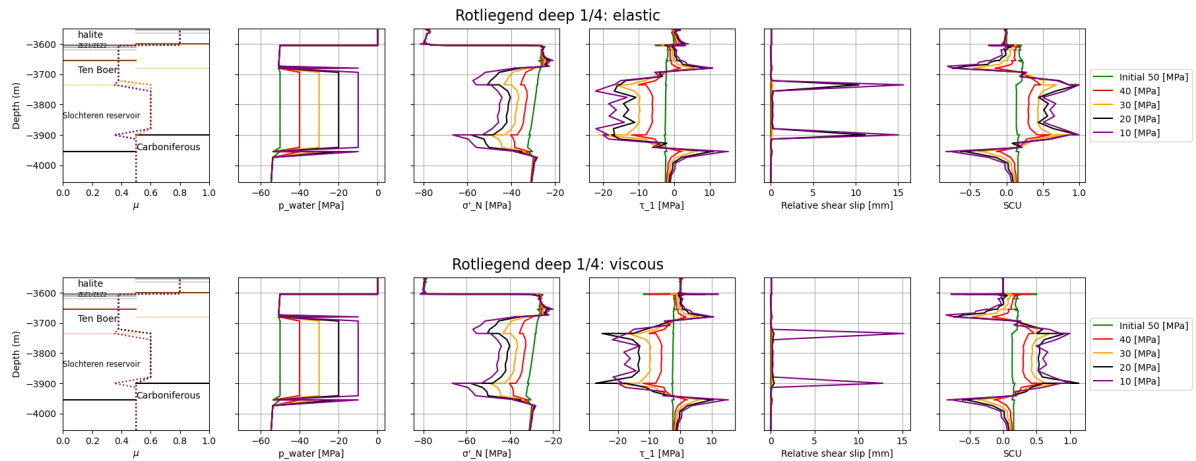


Figure 6.20: Results along the fault for the Rotliegend deep model with a relative reservoir offset of 1/4.

6.2.3. Rotliegend models 3/4 offset

The results for the Rotliegend models with a relative reservoir offset of 3/4 can be found in Figures 6.21 and 6.22. When looking at the effective normal and shear stress it can be seen that there are some clear differences between the elastic and viscous models in the upper part. The elastic model has a decreasing effective normal stress and an increasing shear stress in the halite section of the fault. Whereas, for the viscous model the stresses remain constant over depletion and the shear stress equals about zero.

When moving down along the fault the normal and shear stress starts to behave different from expected for the larger depletion phases. The large peaks disappear in particular in the shear stress at the boundaries and the curve starts to become irregular in between the layer boundaries. When looking at the relative shear slip a slip zone can be identified, where the reservoir is juxtaposing to itself. The slip but also slightly propagates into the fault section above and below the juxtaposition boundary. The friction coefficient decreases over the slip zone to the dynamic friction coefficient. Resulting in an SCU value of 1.0. At the top and bottom of the slip section the shear stress has drastically decreased to negative value in some cases.

When comparing the elastic to the viscous model it can be seen that with viscosity the shear slip is smaller than for the elastic model (80 against 100mm) (at 5MPa). For the deep model there is a slip

zone at 20MPa for the elastic model, however for the viscous model there is no zone, only two peaks.

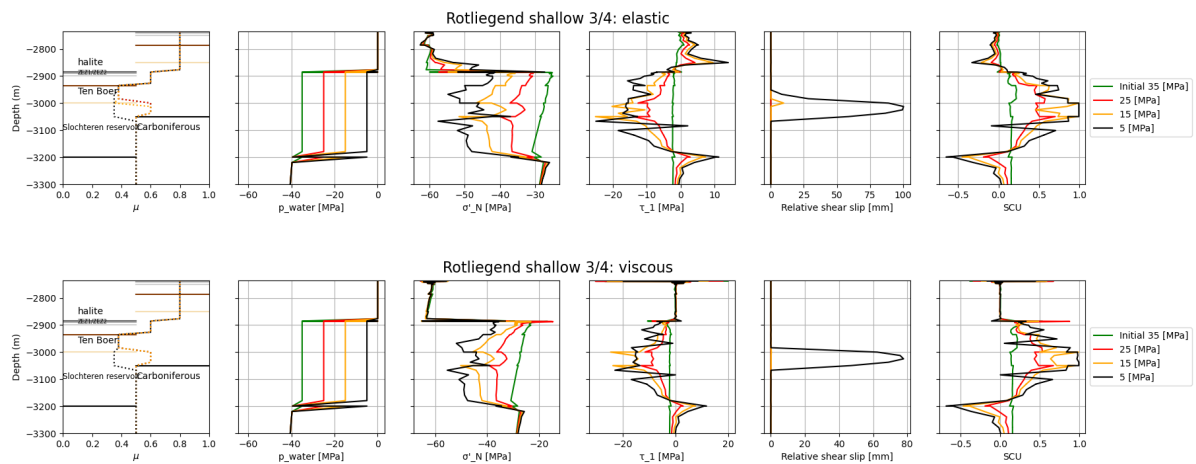


Figure 6.21: Results along the fault for the Rotliegend shallow model with a relative reservoir offset of 3/4.

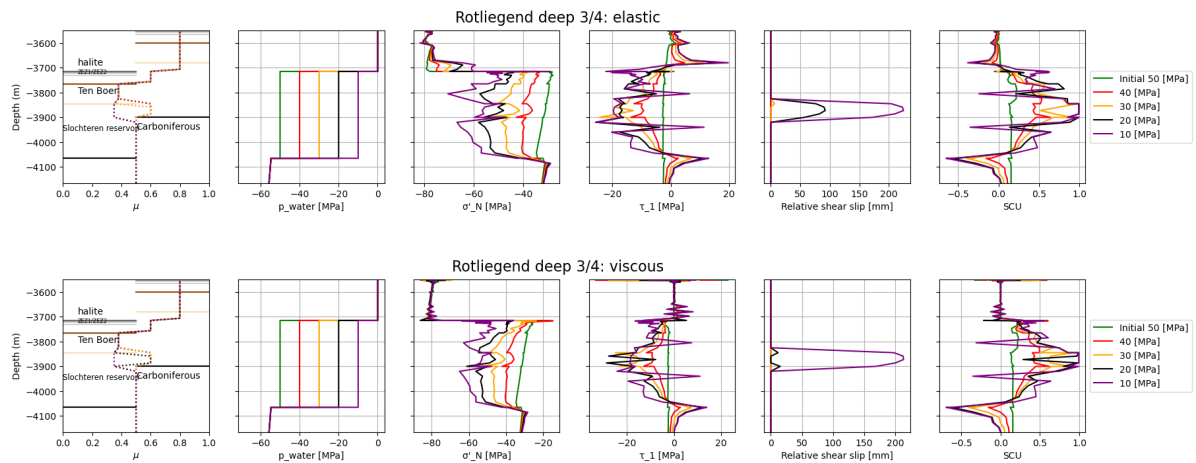


Figure 6.22: Results along the fault for the Rotliegend deep model with a relative reservoir offset of 3/4.

1D result comparison with 2D result & Reservoir Comparison

As discussed in the previous section the models in general behave as expected in Figure 3.7. Only the difference is that in other studies (Buijze et al., 2017; van den Bogert, 2018) the halite is modeled with a hydrostatic pore pressure, whereas in this study the pore pressure is zero, giving much larger effective horizontal stresses. As mentioned above the difference between the elastic and viscous models can be mainly found in the halite section of the fault. Where the effective normal stress decreases and shear stress increases over depletion for the elastic model and remains constant for the viscous. The exact differences for each model between the elastic and viscous properties are given in Figure 6.23. As can be seen especially for the Carbonate and the Rotliegend 3/4 models the effective normal stress increases in the halite and decreases just below the halite boundary with the viscous property. This is expected when looking at the difference plot of the effective vertical stress in 2D (Figure 6.9 and the other plots in the appendix). In the halite and the layer juxtaposed to the halite, the effective horizontal stress is larger for the viscous model, resulting in a larger stress acting normal to the fault. In the layers below the halite there is a decrease in effective horizontal stress for the viscous model compared to the elastic model. Resulting in a smaller stress acting normal to the fault. The further away from the bottom boundary of the halite the lower the difference in stress becomes.

When looking at the difference plot of Figure 6.10 and the other effective vertical stress figures in the appendix. It can be seen that below the bottom halite boundary, the vertical stress is lower for the viscous model around the fault then for the strain model. This results in a lower in shear stress below the halite section, which can be seen in Figure 6.23. When comparing the Carbonate model, with the R1 and R3 models in Figure 6.23, but also with the results shown in the previous sections. It can be seen that the difference pattern for the Carbonate and R3 are more or less similar, however the results from the Rotliegend 3/4 are a bit more spiky, as this model includes more layers between the halite and reservoir. The magnitudes in difference are on the other hand larger for the R3 model. The Rotliegend 1/4 model has the smallest differences in effective normal and shear stress between the elastic and viscous models. Due to the lack of juxtaposition with the reservoir and the corresponding stress changes described in Section 6.1.2.

What also can be seen from Figure 6.23, is that after failure, the difference in the normal and shear stress becomes much larger and irregular then in the phases before failure. This is visible in for example the purple curves from the RD1 and RD3 models.

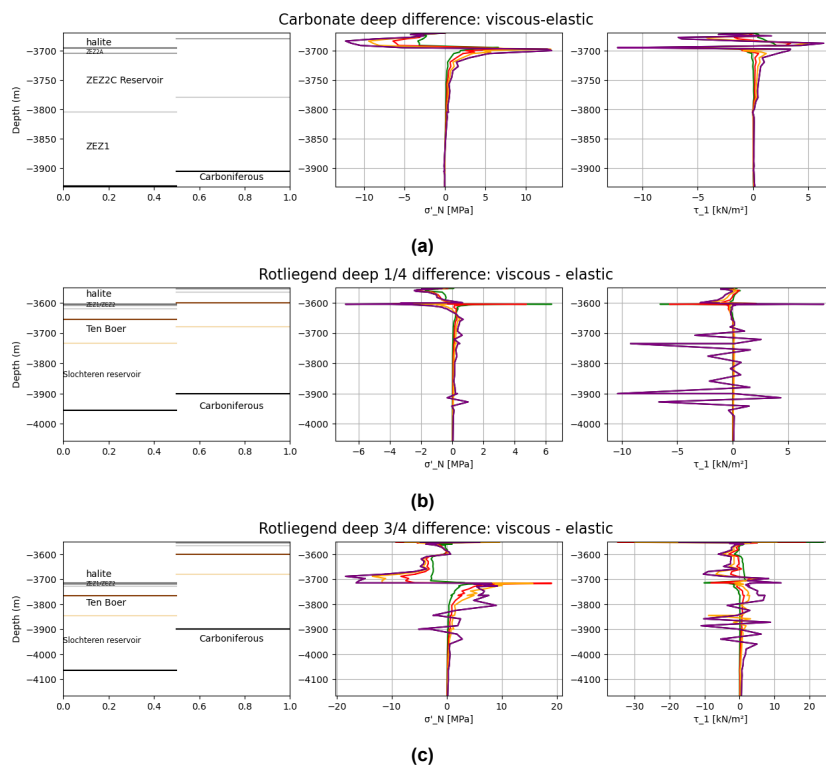


Figure 6.23: Difference between the elastic and viscous models plotted along the fault for the effective normal and shear stress. Only the deep models are shown, as the shallow models behave in a similar manner.

When comparing the Carbonate model with the R1 and R3 models, it can also be seen that the slip behaviour is significantly different for the models. For the Carbonate model no slip occurs, the R1 models only show slip at one or both reservoir boundaries with a different layer. For the R3 models there is slip along the whole reservoir juxtaposition, which continues a little in the sections above and below. The fault used in the Carbonate has larger friction coefficient (0.7 of the BZ) then the fault used in the Rotliegend (0.6 for SS, 0.5 DC and 0.4 TB). This gives a larger resistance against slipping. Another reason why there is no slip detected in the Carbonate models for this offset is that the K_0 decreases less with depletion, due to the higher Poisson's ratio of the Carbonate layer (0.35) against (0.2) of the Rotliegend. The Carbonate model is also not modelled with a relative offset of 3/4, which would give a larger risk of slipping.

The difference between the R1 and R3 model is due to the distance of the reservoir juxtaposition with itself. For the R1 model the distance is too large for the two peaks to connect, whereas for the R3 this

distance is small enough to be able to form a slip zone. Also the stress ratio's are larger for the R3 models compared to the R1 models.

6.2.4. Failure analysis

From the figures in Section 6.2, it can be concluded that the relative shear slip along the fault is larger for the elastic model then for the viscous model. The hypothesis mentioned in Section 3.3.2, stated that due to the high horizontal stresses within the salt, the horizontal stress is being reduced at reservoir level (Orlić & Wassing, 2012; Muntendam-Bos, 2021). The reduction in σ'_x would mean a lower K_0 ratio for the viscous model compared to elastic model and thus a larger potential for slip, however the opposite is observed.

From Section 6.1.2, it was concluded that the effective horizontal stress and the K_0 ratio are indeed lower for the viscous model in the Basal Zechstein layers below the halite (for the Carbonate model only in the ZEZ2A layer). However, in the reservoir layers, a slight increase in stress ratio can be observed (Figures 6.11 till 6.16). Figure 6.24, zooms in on the slip boundaries of the RS1 model, where the reservoir is juxtaposed to itself. The K_0 ratio is higher for the viscous model at reservoir level. The decrease of the effective horizontal stress with the viscous property on the layers below the halite is not visible anymore at reservoir level. On the contrary, the decrease in effective vertical stress is still visible at reservoir level, increasing the K_0 ratio.

In other words, for the layers just below the halite the horizontal decrease is lower then the vertical, resulting in a decrease in stress ratio K_0 . But for the deeper reservoir only the vertical stress decrease is present, reducing the slip potential.

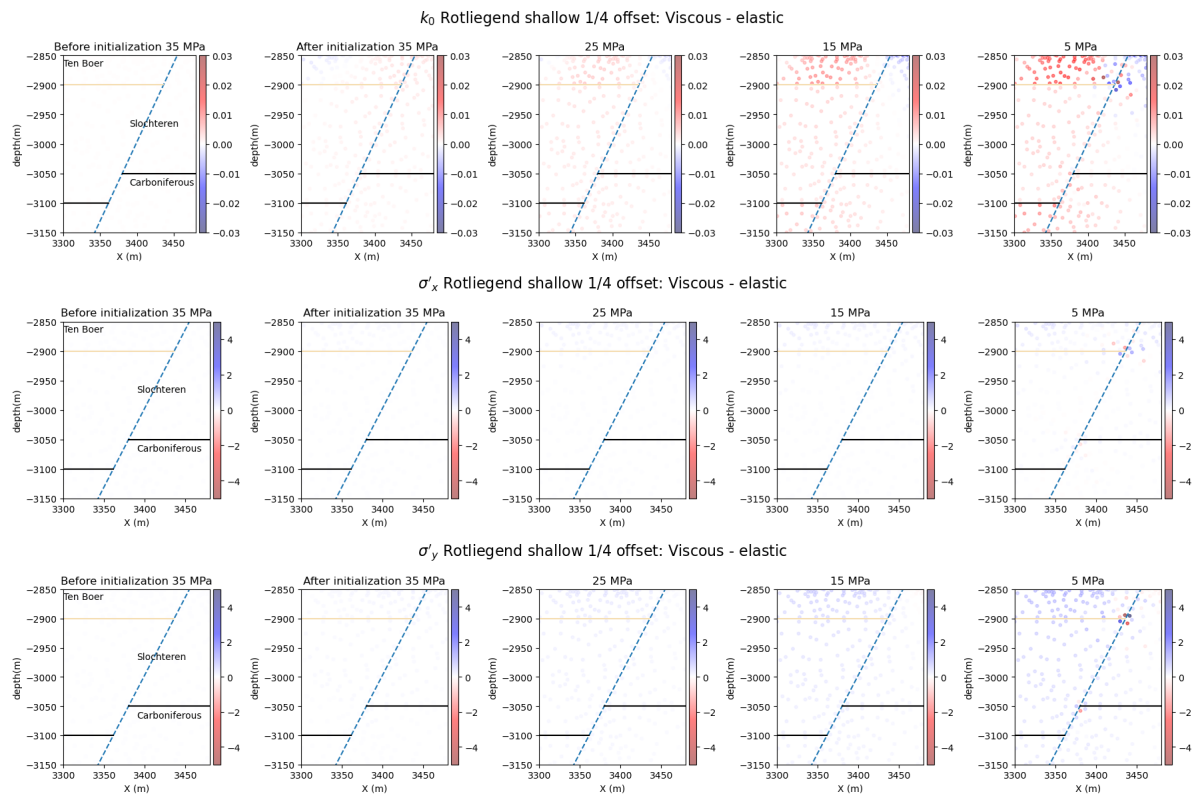


Figure 6.24: Stress results per depletion phase of the Rotliegend shallow model with 1/4 reservoir pressure. The section is zoomed in on the juxtaposition of the reservoir with itself and the boundaries, where the slip occurred in the final phase.

After failure, the vertical stress is being released with the slip, as mentioned before, the peak in shear stress decreases at the failure location. For the elastic model this release in stress is larger than for the viscous model, as the slip occurs for a smaller depletion pressure and has a larger magnitude. This gives a smaller difference in vertical stress between the viscous and elastic model at reservoir

level and can make the viscous model even larger than the elastic model. This can be seen at the reservoir pressure of 5MPa in the figure above, where some points become red around the failure location. At these points the horizontal stress (and consequently the normal stress) is being increased for the viscous model.

6.3. Summary of results

The key results of this chapter are summarised by Figure 6.25. This figure illustrates the stress ratio changes in and outside the reservoir when a reservoir is being depleted. The left figure gives the stress ratio changes for the elastic case, as discussed in Section 6.1.2, K_0 is being decreased within the reservoir and in the layers directly juxtaposed to the reservoir. Above and below the reservoir, the stress ratio is increased with depletion. The right figure, illustrates the stress change ratio for the viscous case with depletion. The figures also show the difference between the viscous and elastic case.

For the halite layer, the stress ratio is decreasing for the elastic model with depletion, but it remains constant for the viscous model (the = sign), as discussed above. Apart from the halite, the general stress change with depletion in the other layers is similar for the viscous models compared to the elastic. However, the magnitude of the increase or decrease is different.

As mentioned before, the stress ratio is being amplified with the viscous property in the layers above the reservoir in the footwall (red +). The stress ratio is larger for the viscous model in the layers next to the reservoir, giving the amplification in the overburden layers. On the other hand this gives a smaller decrease in stress ratio for the viscous model, compared to the elastic model, in the reservoir directly juxtaposed to the halite. For the layer directly below the halite, K_0 is further decreased in the Basal Zechstein layers, which gives the red colour of the minus sign (amplification). The same can be identified in the layer juxtaposed to these BZ layers. The amplification of the stress decrease, means a larger risk of failure, however, these areas have not shown any slip.

When moving further down, it can be concluded that in the reservoir, the decrease in stress ratio is less for the viscous model compared to the elastic model (contradicting Orlić & Wassing (2012)). This blue minus sign is the reason why there is less slip in the viscous model compared to the elastic model. The stress ratio is slightly larger for the viscous model, moving the fault slightly further away from criticality. The reason for the sudden change in red minus in the Basal Zechstein layer to the blue minus in the Reservoir, is due to the propagation of the differences in effective vertical and effective horizontal stress, which has been discussed in the previous section (6.2.4). Figures C.16 and C.17 in the appendix, show the same figures but then for the effective horizontal and vertical stresses. The reason why the effective vertical stress differences propagate further into the reservoir, whereas the effective horizontal stress is limited to the Basal Zechstein layer, can not be explained by this project and further research is needed for that.

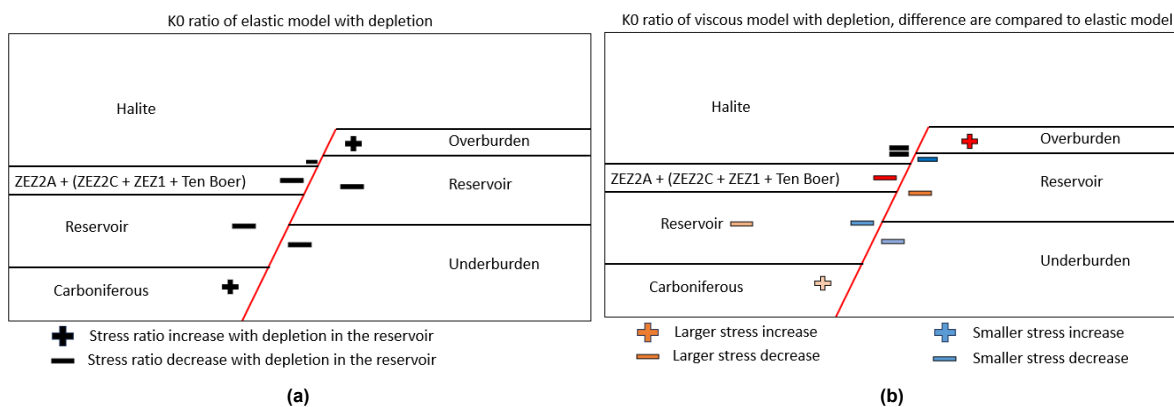


Figure 6.25: The change in stress ratio regime with reservoir depletion. For the elastic model (a) and the viscous model (b). The viscous figure does also indicate the relative change in stress with respect to the elastic model. If the sign is red, it means that the stress ratio increase or decrease is amplified for the viscous model. If the sign is blue, it means that the stress ratio decrease is smaller compared to before depletion with the viscous model. The darker the colour, the larger the difference between the elastic and viscous model.

Figure 6.25, is applicable to the Carbonate model, as well as the Rotliegend 1/4 and 3/4 models. However, the magnitude of the signs and the magnitude of the differences between the elastic and viscous model is different. The Rotliegend 3/4 models show the largest magnitudes, followed by the Carbonate model, which are the reservoirs which juxtapose the halite to the reservoir. The Rotliegend model 3/4 show larger magnitudes than the Carbonate model, as the Carbonate model is more resistance against deformation and thus stress changes. The smallest magnitudes can be found in the Rotliegend 1/4 model, where the impact of the viscous property is the smallest due to a lack of juxtaposition to the reservoir.

7

Discussion

With the results being discussed, the aim of this chapter is to assess the quality of the results. First of all, the results will be validated by the study of Buijze et al. (2017), to validate the software that is being used (Section 7.1). Secondly, the assumptions and limitations will be discussed and their impact on the outcome of the study (Section 7.2).

7.1. Result validation

As already discussed in Chapter 6, the results behave as expected. Both the change in stress within the reservoir as the change in stress in the layers surrounding the reservoir is in agreement with the theory described in Sections 3.2.2 and 3.2.3.

In addition, the software (Plaxis 2D) and the corresponding models that are being used can be validated by comparing the results to the study of Buijze et al. (2017), which uses a different software (DIANA). As discussed in Section 5.1, the Rotliegend Shallow model is created with the Groningen model in Buijze et al. (2017) as a reference. Therefore the geomechanical models are similar, which allows for a suitable comparison between the results of both studies. DIANA and Plaxis are both geotechnical, structural and civil engineering finite element softwares, with which stress changes can be simulated. Figure 7.1, shows the plots from the study by Buijze et al. (2017), together with the results of the Plaxis output of this study. The results that are plotted are the vertical strain, horizontal- and vertical displacement. Buijze et al. (2017), uses a depletion pressure of 12.89, in this project pressure depletion is modelled with steps of 10MPa. Therefore the results of $\Delta P = 10$ MPa are used, as this is closest to the pressure depletion of 12.89 MPa.

When looking at the figure, it can be seen that the plots of this study and the study of Buijze et al. (2017), show a similar pattern. The values of the study of Buijze et al. (2017), are slightly larger, but this is because the depletion is also slightly larger (extra 2.89 MPa). From this figure it can be concluded that the results from Plaxis (elastic) can be validated by other studies using different software, in this case Buijze et al. (2017). This only validates the results retrieved from the elastic models (Mohr Coulomb model) and not the from the creep model, as this is not included in the study of Buijze et al. (2017). An important note is that both studies use similar assumptions, which have an impact on the results. Therefore, the results of both studies are an approximation of reality. The assumptions will be covered in the next section.

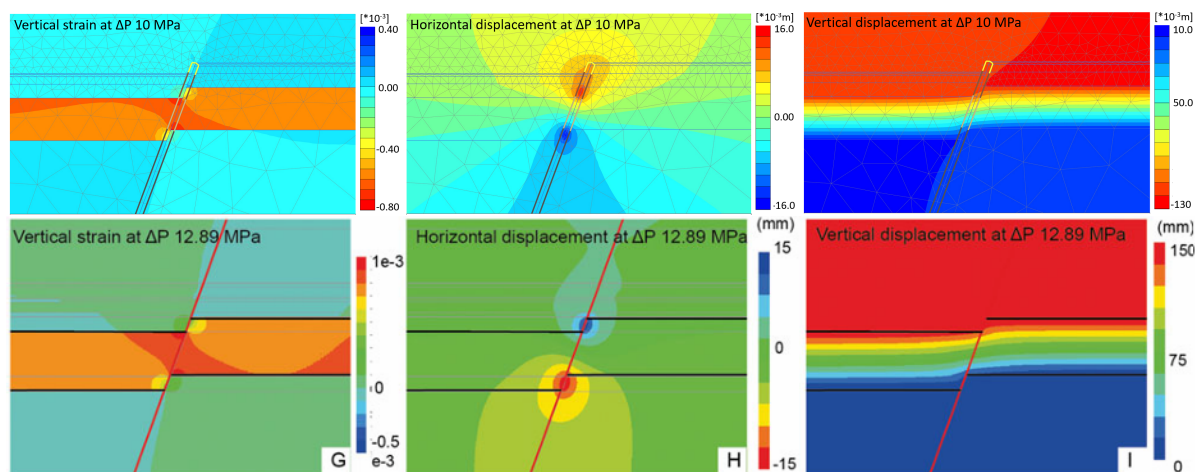


Figure 7.1: Comparison of the deformation results with Buijze et al. (2017). Note the difference in sign convention between the two studies and the difference in legend for the horizontal displacement.

7.2. Limitations and assumptions

In this section the limitations and assumptions will be discussed. First the limitations of the software are covered, which is followed by the assumptions that are made.

7.2.1. Limitations of software

Plaxis has the following limitations:

First of all, the software is not able to model salt intrusion into the fault. Moreover, it is also not possible to assign properties to a fault element such as viscous creep and isotropic stress, only elastic and failure parameters could be assigned to the fault elements. Therefore, the impact of the salt intruding a fault, as described by Kettermann et al. (2017), and the corresponding consequences on the stress and slip, can not be analysed with Plaxis.

Secondly, there are also some limitations with the material models and in particular the one used for the halite, the user-defined N2PC-MC model. This is a visco-plastic model, whereas the Zechstein halite behaves in a visco-elastic manner. While the visco-elastic strain would return to its initial value over time if the stress is released, the visco-plastic strain does remain constant with stress release. For this study, the depletion of the reservoir is modelled, therefore the stress is mainly building up and no stress release is considered. As mentioned before, there is some stress release when failure is occurring, however, this is relatively limited and significantly far away from the halite. So even though it is not tested, it is not expected that the difference between visco-plastic and visco-elastic plays a significant role in this project. However, it is important to consider this difference when using this model in future studies and other subsurface projects where there is a significant stress release (for example, cyclic hydrogen storage).

Another limitation is the implementation of slip weakening. In the studies by Buijze et al. (2017); van den Bogert (2018) and others, a linear slip-weakening function is used, however in the Mohr Coulomb model of the discontinuity element there is an instant slip-weakening. Hence, the friction coefficient does not decrease over the critical slip distance to the dynamic friction coefficient. According to van den Bogert (2018), the reservoir depletion at which seismic rupture occurs is strongly influenced by the slope of the linear slip-weakening. However, neither the slope of the linear slip-weakening or the critical slip distance can not be implemented as a parameter in Plaxis.

7.2.2. Assumptions

For the modelling there are some assumptions made, which can have a significant impact on the results. The assumptions have already been mentioned in chapter 5, but this section will highlight some of those assumptions and discuss the impact of the on the outcome of this study. First the assumptions on the time interval and K_0 ratio are covered, because relatively high values have been implemented for these parameters. But due to limited time simulations could not be run for other values. After these sections,

the other assumptions and their consequences on the outcome will be covered.

Implementation of the time interval and salt properties

As mentioned in Section 5.2.4, the time interval used for the different depletion phases is 15 years. This is based on the Groningen gas reservoir, however, for the smaller gas fields this should be significantly smaller. The time does have a significant impact on the results. The smaller the time interval, the smaller the deformation and the smaller the impact of the viscous property compared to the elastic model.

Therefore, to compare the effect of the the time interval, this section will present results with a depletion interval of 5 years. Due to time constraints this is only done for the model that has been effected most by the viscous property, which is the Rotliegend model with a relative reservoir offset of 3/4. The stress ratio results (K_0) at a depletion of $\Delta P = 20 \text{ MPa}$ are shown in Figure 7.2. It shows both the original result of the viscous model with a 15 years depletion interval (similar to Figure 6.16, as well as the new result plot for a time interval of 5 years. The difference between the two results is also given in the right plot. The plots are also given for the effective horizontal and vertical strains in Figures D.1 and D.2 in the appendix.

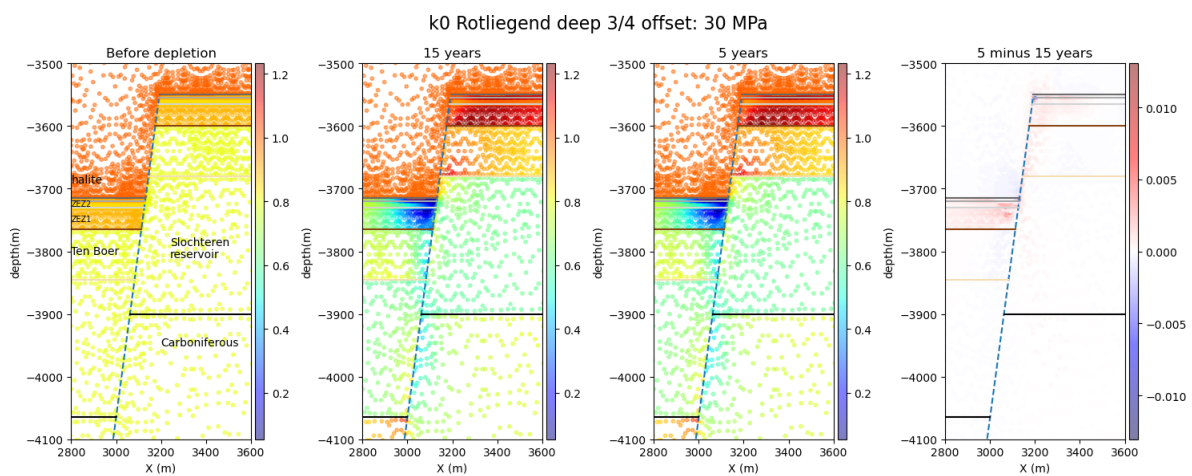


Figure 7.2: K_0 ratio for the viscous RD3 model with a depletion time interval of the original 15 years and 5 years.

When comparing the results for different time intervals, it can be seen that the 15 years time interval gives a slightly larger decrease in stress ratio in the Basal Zechstein layers below the halite. This is because with 15 years, the salt has a longer time to deform at a slow strain rate. Therefore, the impact of the viscous salt is larger. However, when comparing the stress ratio difference between the two time intervals with the stress ratio difference of the viscous model and the elastic model, given in Figure 6.16. It can be seen that the stress ratio difference in time interval is much smaller (up to 0.010) than the difference between the viscous and elastic model (up to 0.4). Therefore, it can be concluded that the time interval of 15 years does not significantly impact the model compared to a time interval of 5 years. Most deformation is taking place within 5 years after depletion and the equilibrium has almost formed. This can also be seen in the figures in the appendix, the difference in strain between the time intervals is relatively small. Compared to the difference in strain between the elastic and viscous models. The depletion rate can be even faster, giving smaller intervals than 5 years, which can have an impact on the model. However, due to limited time, smaller interval time have not been investigated.

Another salt related assumption is concerning the input parameters for the N2PC-MC model. These have been taken from the Plaxis manual (Plaxis, 2022) and are not specifically for the Zechstein salt. Using different parameters can have an impact on the behaviour and strain rate of the salt. A first indication of the sensitivity of the input parameters can be seen in appendix Figure D.3, which compares the stresses acting on the fault for different input parameters. However, this plot has been made in an early phase of the study, the model has been slightly changed afterwards. Due to time constraints a new sensitivity analysis could not have been performed. From the figure it can be seen that the difference

between input parameters is limited (less than 1 MPa). However, these results are with a time interval of 15 years, giving a long time to reach equilibrium for both parameters. A smaller time interval can potentially give a significant difference between different input parameters. However, further studies on the input parameters and the time interval are needed to confirm this hypothesis.

K_0 of the deeper models

As discussed in Section 5.2.1, due to time constraints the input for the K_0 has been set equal for both the shallow and deep model (0.75 for Rotliegend and 0.78 for Carbonate). However, as calculated the K_0 ratio for the deep models should be lower (0.71 and 0.75) due to a larger overpressure. A smaller K_0 ratio would result in a larger Mohr Circle and a larger risk of fault reactivation. Less pore pressure is needed for slip to occur, therefore, this is an important assumption to take into consideration. It is assumed that the smaller stress ratios do not influence the viscous behaviour of the halite and therefore do not have an impact on the conclusions related to the viscous property, only on the slip in general. Further studies are needed to investigate the exact impact of the smaller stress ratios on the slip. It is also recommended to perform a sensitivity analysis to see the uncertainty of stress ratio (and other parameters) in the Plaxis software. The initial plan was to include that in this project, however due to time constraints this was not feasible.

Other assumptions

As mentioned in 5, other assumptions have also been made. The assumptions and the consequences are given as follows:

First of all, there are some assumptions regarding model geometry and formation properties.

The study uses a conceptual model, including one fault and a simplistic geometry. However, the structures in the subsurface can be much more complicated. With a combination of different faults, different offsets, and tilted layers, which would impact the state of stress. The impact of the viscous salt has not been straight-forward for all the reservoirs in the North-East Netherlands.

In this study it has been decided to use the same formation parameters for all the models. However, properties such as porosity, may be highly variable between different gas fields and even within a field. A change in porosity would also effect parameters such as the Young's modulus and Poisson's ratio. The subsurface is very heterogeneous and the parameters are in reality different for every field. There is also a large uncertainty in the initial stress ratio of all the fields. Therefore, the conclusions made in this report are not an true comparison between different reservoirs and gas fields.

Another assumption is regarding the halite pore pressure. Different studies use different pore pressure values for the Zechstein formation, which is considered to have almost zero porosity. van den Bogert (2018), Buijze et al. (2017) and Orlic (2016), use a hydrostatic pore pressure. However, Orlic & Wassing (2012), Lele et al. (2015) and Muntendam-Bos et al. (2008) use a zero pore pressure for the Zechstein formation. Orlic & Wassing (2012) is the only study, which studies the impact of the salt, therefore it has been decided to also use zero pore pressure for the halite. Furthermore, most studies model the Zechstein as a homogeneous formation, without the anhydrite and carbonate layers. Therefore, they use the same pore pressure for all the layers within the Zechstein. However, the permeability of the halite is significantly different from the Carbonate and anhydrite. The pore pressures of the Carbonate and anhydrite is considered to be non-zero and depending on the overpressure. However, there has been very limited research on the anhydrite layers and it is not certain what the salt concentration is and consequently if there is any pore pressure in this layer.

The viscous parameters used in the models is retrieved from a Plaxis example. Even though these are rock salt parameters, these are not specific for the Zechstein rock salt. There have been other research to the viscous parameters of rock salt, however they are not specific for the Zechstein. Also the equations used in those studies is slightly different from the equation in the N2PC-MC model.

Secondly the assumptions regarding reservoir depletion:

It is assumed that depletion occurred only in the Slochteren and ZEZ2C layer, without any depletion in the over and underburden layer. For the Rotliegend there might be some depletion in the Carboniferous and Ten Boer layer, due to sand lenses (figure 2.7a). The pressure decrease in these layers influences and complicates the state of stress on the fault and consequently the slip behaviour.

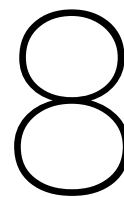
Furthermore it is also assumed that there is a homogeneous depletion throughout the whole reservoir. However, due to structures such as tilted layers, a Gas-Water content which is located somewhere in

between the reservoir and a (partially) sealing fault depletion might not be homogeneous. Moreover, for simplicity, fluid flow has been neglected in this study. However, according to Zbinden et al. (2017), fluid flow processes exert a strong influence on the evolution of pore pressure and stress within fault zones intersecting reservoirs. For example, fault strength will significantly be reduced due to fluid flow, affecting the slip of the fault.

Finally, there are also some important assumptions regarding the fault modelling, which are already partially described in chapter 5.

It is assumed that the pore pressures in the fault is similar to the reservoir if the fault section is connected to the reservoir, except for the halite fault sections. However, in reality the fault is less permeable than the reservoir, especially if the fault gouge consist of different materials. The permeability of the Anhydrite fault is uncertain, in this research it is assumed that the Anhydrite fault section gets the same pore pressure as the reservoir, however this is not confirmed. A different pore pressure in a fault would give a different effective normal stress acting on the fault and consequently different resistance against slipping.

Furthermore the weakest lithology is assigned to a fault if two different lithologies are assigned. Whereas the fault gouge would consist of a mixture of both lithologies. Consequently, the friction parameters and the friction behaviour of the fault will be different. Moreover, the fault is considered to be cohesionless, however experiments have shown that over time fault healing occurs Buijze et al. (2017). This would result in a larger cohesion and consequently larger resistance against slipping. The longer the healing time, the greater the re-strengthening of the fault. If the fault is reactivated again, the healing may be lost and the cohesion is dropped again.



Conclusion

The question posed in the beginning of this report was:

How do the viscous salts in the Zechstein formation influence the state of stress and slip in the Rotliegend and Carbonate gas fields in the North-East of the Netherlands?

To answer this question different models have been created, representing fault structures in gas fields in the North-East Netherlands. Gas depletion has been modelled with different salt properties, elastic and viscous, in order to investigate the influence of the viscous behaviour of the salt.

Reviewing the 2D strain it can be concluded that the viscous behaviour amplifies the strain behaviour in the halite and the layers juxtaposed to the halite.

For the stresses it can be concluded that the effective horizontal stresses are larger for the viscous model in the halite and the juxtaposed layers. The higher horizontal stresses cause a decrease in horizontal stress in the layers directly below the halite. The vertical stresses are smaller for the viscous property in the halite and layers below, this decrease is smaller than the decrease for the horizontal stress. These stress changes result in a larger K_0 ratio in the halite and the juxtaposed layers, with the viscous property, moving the fault away from criticality. **With the viscous behaviour, the K_0 is smaller in the layers directly below the halite (Figure 6.25). The difference in stress are already observed before depletion.**

The difference of the vertical stress in the layers below the halite, penetrates deeper than the difference in horizontal stress. This results in still a decrease vertical stress, but no decrease in horizontal stress at reservoir level, with the viscous property. **Consequently the K_0 is larger for the viscous property in the reservoir around the fault and a larger pore pressure decrease needed for slip, this contradicts the study of Orlić & Wassing (2012).** However, in that study the visco-elastic caprock was located directly above the reservoir, whereas in this study there are some layers separating the halite and reservoir. **If slip occurs in both models, the amount of slip is also larger for the elastic model compared to the viscous model.**

For the different offsets and reservoir properties the following conclusions can be made:

Firstly, the influences of the viscous model are the largest if the halite is juxtaposed to the reservoir. However, the influence of the viscous property on the slip can still be seen when the halite is not juxtaposed to the reservoir.

The difference in the viscous deformation behaviour of the N2PC-MC model does not significantly depend on depth. There is a limited difference between the results of the elastic and viscous models are more or less similar for the shallower and deeper models.

Finally, the impact of the viscosity is larger on the Rotliegend models than on the Carbonate models, due to the larger resistance against deformation of the Carbonate layer, compared to the Sandstone layer.

A number of recommendations can be made for future studies:

- It is recommended to perform a sensitivity analysis, to assess the uncertainty of Plaxis.
- Further studies are needed on the time interval, salt properties and the K_0 ratio. In order to get a clear overview of the impact of those parameters on the results, as this is not done in this study due to time constraints.
- It is recommended to validate the results of the N2PC-MC model to results using a different material model for the rock salt, such as visco-elastic models or other visco-elastic/plastic models with a different implementation.
- It would be helpful to do a similar study in which the salt intrusion can be modelled or in which properties can be assigned to the fault. To further understand the impact of the viscous salt on the stress and slip.
- For the Carbonate reservoirs it is recommended to get a better understanding of the properties of the Carbonate and mainly the Anhydrite layers. As most modelling studies are focussed on the Rotliegend reservoirs, less is known about these layers.
- Finally, it is recommended to use a similar dynamical model as Buijze et al. (2017), to analyse the influences of the viscous property on the nucleation and fault rupture. In addition, fault healing can also be considered.

Bibliography

- Anderskouv, K. & Surlyk, F. The influence of depositional processes on the porosity of chalk. *Journal of the Geological Society*, 169:311–325, 05 2012. doi: 10.1144/0016-76492011-079.
- Baisch, S., Seidemann, M., Vörös, R., & Bartels, T. Numerical Simulation of Seismicity Induced by Gas Production—Implications for the seismic hazard Assessment. *Journal of Geophysical Research: Solid Earth*, 128(9), 9 2023. doi: 10.1029/2023jb027025.
- BOA. Eindrapport multidisciplinair onderzoek naar de relatie tussen gaswinning en aardbevingen in Noord-Nederland. Technical report, BOA (Begeleidingscommissie Onderzoek Aardbevingen), 11 1993.
- Bonté, D., van Wees, J.-D., & Verweij, J. Subsurface temperature of the onshore netherlands: new temperature dataset and modelling. *Netherlands Journal of Geosciences - Geologie en Mijnbouw*, 91(4):491–515, 2012. doi: 10.1017/S0016774600000354.
- Buijze, A. J. L. *Numerical and experimental simulation of fault reactivation and earthquake rupture applied to induced seismicity in the Groningen gas field*. PhD thesis, Utrecht University, Utrecht, 07 2020. URL <https://dspace.library.uu.nl/handle/1874/400692>.
- Buijze, L., Van Den Boogert, P., Wassing, B., Orlić, B., & Veen, J. T. Fault reactivation mechanisms and dynamic rupture modelling of depletion-induced seismic events in a Rotliegend gas reservoir. *Netherlands Journal of Geosciences*, 96(5):s131–s148, 12 2017. doi: 10.1017/njg.2017.27.
- de Jager, J. & Geluk, M. Petroleum geology of the netherlands. 01 2007.
- de Jager, J. & Visser, C. Geology of the groningen field - an overview. *Netherlands Journal of Geosciences*, 96:s3–s15, 12 2017. doi: 10.1017/njg.2017.22.
- Dhatt, G., Lefrançois, E., & Touzot, G. *The Finite Element Method: its Basis and Fundamentals*. 1 2013. doi: 10.1016/c2009-0-24909-9. URL <https://doi.org/10.1016/c2009-0-24909-9>.
- Duin, E., Doornbal, J., Rijkers, R., Verbeek, J., & Wong, T. Subsurface structure of the netherlands - results of recent onshore and offshore mapping. *Netherlands J. Geosci.*, 85, 12 2006. doi: 10.1017/S0016774600023064.
- Fjær, E., Holt, R., Horsrud, P., Raaen, A., & Risnes, R. Chapter 3 geological aspects of petroleum related rock mechanics. In *Petroleum Related Rock Mechanics 2nd Edition*, volume 53 of *Developments in Petroleum Science*, pages 103–133. Elsevier, 2008a. doi: [https://doi.org/10.1016/S0376-7361\(07\)53003-7](https://doi.org/10.1016/S0376-7361(07)53003-7). URL <https://www.sciencedirect.com/science/article/pii/S0376736107530037>.
- Fjær, E., Holt, R., Horsrud, P., Raaen, A., & Risnes, R. Chapter 1 elasticity. In *Petroleum Related Rock Mechanics 2nd Edition*, volume 53 of *Developments in Petroleum Science*, pages 1–53. Elsevier, 2008b. doi: [https://doi.org/10.1016/S0376-7361\(07\)53003-7](https://doi.org/10.1016/S0376-7361(07)53003-7).
- Fossen, H. Chapter 6 rheology. In *Structural Geology*, volume 53 of *Developments in Petroleum Science*, pages 411–486. Elsevier, 2016.
- Hol, S., van der Linden, A., Zuiderwijk, P., Marcelis, F., & Coorn, A. Mechanical characterization of Permian reservoir sandstone from the Moddergat-3 well in the Dutch Wadden Area. Technical Report SR.15.11614, Shell Global Solutions International B.V., Rijswijk, 2015.
- Hunfeld, L. B. *Frictional properties of simulated fault gouges from the Groningen gas field and implications for induced seismicity*. PhD thesis, Utrecht University, Utrecht, 06 2020.
- Kettermann, M., Abe, S., Raith, A. F., de Jager, J., & Urai, J. L. The effect of salt in dilatant faults on rates and magnitudes of induced seismicity – first results building on the geological setting of the groningen rotliegend reservoirs. *Netherlands Journal of Geosciences*, 96(5):s87–s104, 2017. doi: 10.1017/njg.2017.19.
- Kim, Y. & Lee, E. Y. Numerical analysis of sedimentary compaction: Implications for porosity and layer thickness variation. 54:631–640, 12 2018. doi: 10.14770/jgsk.2018.54.6.631.
- Lele, S., Garzon, J., Hsu, S.-Y., DeDontney, N., Searles, K., & Sanz, P. Groningen 2015 Geomechanical Analysis. Technical report, NAM (Nederlandse Aardolie Maatschappij), 11 2015.
- Li, S. & Urai, J. L. Rheology of rock salt for salt tectonics modeling. *Petroleum science/Petroleum*

- Science*, 13(4):712–724, 10 2016. doi: 10.1007/s12182-016-0121-6. URL <https://doi.org/10.1007/s12182-016-0121-6>.
- Li, S., Abe, S., Urai, J., Strozyk, F., Kukla, P., & Gent, H. A method to evaluate long-term rheology of zechstein salt in the tertiary. *Mechanical Behavior of Salt VII - Proceedings of the 7th Conference on the Mechanical Behavior of Salt*, pages 215–220, 03 2012. doi: 10.1201/b12041-31.
- Mulders, F. M. M. *Modelling of stress development and fault slip in and around a producing gas reservoir*. PhD thesis, Delft University of Technology, Delft, 12 2003.
- Muntendam-Bos, A. Geomechanical characteristics of gas depletion induced seismicity in the Netherlands. *55th U.S. Rock Mechanics/Geomechanics Symposium*, 6 2021. URL <https://onepetro.org/ARMAUSRMS/proceedings/ARMA21/All-ARMA21/ARMA-2021-1038/468234>.
- Muntendam-Bos, A., Wassing, B., Geel, C., Louh, M., & van Thienen-Visser, K. Bergermeer Seismicity Study. Technical Report R1071/B, TNO, 11 2008.
- Muntendam-Bos, A., Hoedeman, G., Polychronopoulou, K., Draganov, D., Weemstra, C., Van Der Zee, W., Bakker, R., & Roest, H. An overview of induced seismicity in the Netherlands. *Netherlands Journal of Geosciences*, 101, 1 2022. doi: 10.1017/njg.2021.14.
- NAM. Technical Addendum to the Winningsplan Groningen 2013 Subsidence, Induced Earthquakes and Seismic Hazard Analysis in the Groningen Field. Technical report, Nederlandse Aardolie Maatschappij B.V., 11 2013.
- NAM. Technical Addendum to the Winningsplan Groningen 2016 Production, Subsidence, Induced Earthquakes and Seismic Hazard and Risk Assessment in the Groningen Field Part I Summary Production. Technical report, Nederlandse Aardolie Maatschappij B.V., 4 2016.
- NLOG. Groningen gasfield, 2024. URL <https://www.nlog.nl/en/groningen-gasfield>.
- Oosterhout, B., Hangx, S., & Spiers, C. *A threshold stress for pressure solution creep in rock salt: Model predictions vs. observations*, pages 57–67. 06 2022. ISBN 9781003295808. doi: 10.1201/9781003295808-6.
- OpenLearn. Introduction to finite element analysis, 2019.
- Orlic, B. Geomechanical effects of CO₂ storage in depleted gas reservoirs in the Netherlands: Inferences from feasibility studies and comparison with aquifer storage. *Journal of Rock Mechanics and Geotechnical Engineering*, 8(6):846–859, 2016. ISSN 1674-7755. doi: 10.1016/j.jrmge.2016.07.003. URL <https://www.sciencedirect.com/science/article/pii/S167477551630141X>.
- Orlić, B. & Wassing, B. A study of stress change and fault slip in producing gas reservoirs overlain by elastic and viscoelastic caprocks. *Rock Mechanics and Rock Engineering*, 46(3):421–435, 12 2012. doi: 10.1007/s00603-012-0347-6.
- Paulides, C. Production analysis of the fractured zechstein-2 carbonate member in the Netherlands a dual porosity model approach, 2016.
- Peryt, T., Geluk, M., Mathiesen, A., Paul, J., & Smith, K. *Zechstein*. In: Doornenbal, J.C. and Stevenson, A.G. (editors): Petroleum Geological Atlas of the Southern Permian Basin Area. EAGE Publications b.v. (Houten): 123-147, 2010.
- Pijnenburg, R. P. J. *Deformation Behavior of Reservoir Sandstones from the Seismogenic Groningen Gas Field: An experimental and mechanistic study*. PhD thesis, Utrecht University, Utrecht, 10 2019.
- Plaxis. *User Defined Soil Models: N2PC-MCT: A VISCOPLASTIC CREEP MODEL INCLUDING A PLASTIC FAILURE MECHANISM FOR ROCKS [ULT]+[GSE]*. Bentley, 1 2022.
- Plaxis. *Material Models Manual 2D*. Bentley Advancing Infrastructure, 12 2023a.
- Plaxis. *Reference Manual 2D*. Bentley Advancing Infrastructure, 12 2023b.
- Plaxis. *Scientific Manual 2D*. Bentley Advancing Infrastructure, 12 2023c.
- Reijers, T. Sedimentology and diagenesis as ‘hydrocarbon exploration tools’ in the late Permian zechstein-2 carbonate member (the Netherlands). *Geologos*, 18:163–195, 11 2012. doi: 10.2478/v10118-012-0009-x.
- Roholl, J., Brunner, L., Versteijlen, N., Hettelaar, J., & Wilpshaar, M. Deterministische Hazard Analyse voor Geïnduceerde Seismiciteit (DHAI), actualisatie 2021. Technical Report R10977, TNO, 2 2022.
- Strozyk, F., Reuning, L., Scheck-Wenderoth, M., & Tanner, D. *The Tectonic History of the Zechstein Basin in the Netherlands and Germany*. 06 2017. ISBN 9780128094174. doi: 10.1016/B978-0-12-809417-4.00011-2.
- TNO. Factsheet Vlagtweede. Technical report, Ministerie van Economische Zaken and TNO, 2009.
- TNO. Injection Related Induced Seismicity and its relevance to Nitrogen Injection: Modelling of geomechanical effects of injection on fault stability. Technical Report R11259, TNO, 11 2015. URL <https://www.tno.nl/en/research-and-development/energy-and-environment/induced-seismicity>.

- [//www.nlog.nl/sites/default/files/tno-report-2015-r10906-public-final05112015_anonymous.pdf](http://www.nlog.nl/sites/default/files/tno-report-2015-r10906-public-final05112015_anonymous.pdf).
- TNO-GDN. *Stratigraphic Nomenclature of the Netherlands, TNO – Geological Survey of the Netherlands*. DINOloket, 2024.
- Tolsma, S. Seismic characterization of the zechstein carbonates in the dutch northern offshore, 2014.
- van den Bogert, P. Depletion-induced fault slip and seismic rupture. Technical report, Shell Global Solutions International B.V., Rijswijk and NAM (Nederlandse Aardolie Maatschappij), 12 2018.
- Van Thienen-Visser, K., Roholl, J., Kempen, B., Hettelaar, J., Geel, C., De Bruin, G. P., & Van Hooff, T. Seismiciteit onshore gasvelden Nederland. Technical Report R10164, TNO, 6 2016. URL <https://repository.tno.nl/islandora/object/uuid%3Aaa00e4fa-4a4b-4837-8a29-05bb04014d0c>.
- van Uijen, W. Rotliegend geology in the southern permian basin: the development of synrift sediments and its relation to seismic imaging, 2013.
- Verweij, J., Simmelink, H., Underschultz, J., & Witmans, N. Pressure and fluid dynamic characterisation of the Dutch subsurface. *Netherlands Journal of Geosciences*, 91(4):465–490, 12 2012. doi: 10.1017/s0016774600000342.
- Zbinden, D., Rinaldi, A. P., Urpi, L., & Wiemer, S. On the physics based processes behind production induced seismicity in natural gas fields. *Journal of Geophysical Research: Solid Earth*, 122(5):3792–3812, 5 2017. doi: 10.1002/2017jb014003.

A

Seismicity and Geology of the North-East Netherlands

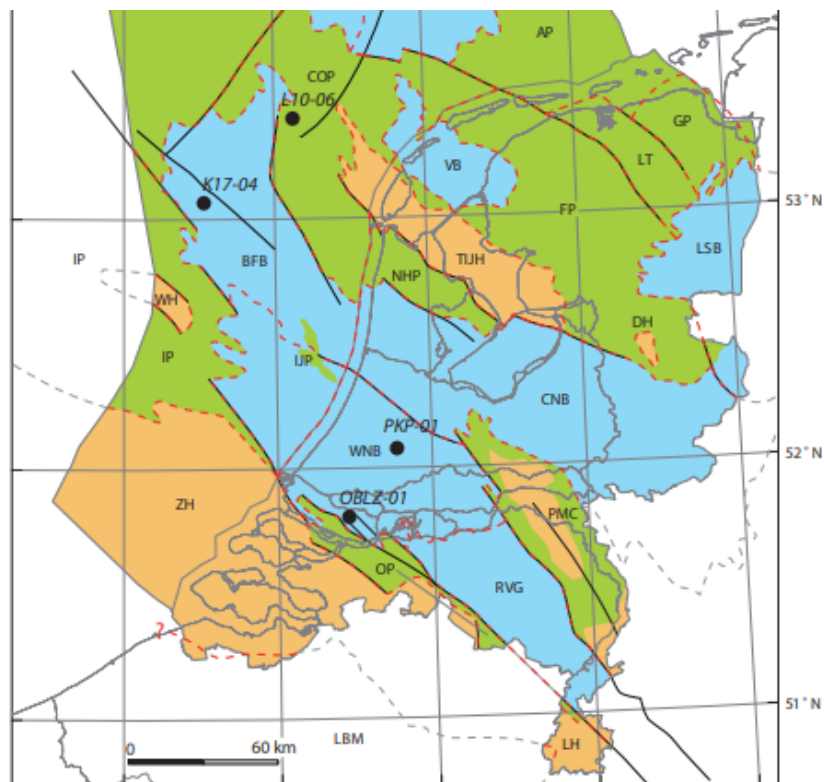


Figure A.1: Structural framework of the Netherlands (Verweij et al., 2012). Platforms are given in green and basins in blue. LT is the Lauwerssea Trough, GP the Groningen platform or Groningen high and LSB the Lower Saxony Basin.

B

Model set-up

Formation	Dalen			Coevorden								Schoonebeek		Average
	Dal-01	Dal-04	Dal-06	Coe-43	Coe-35	Coe-42	Coe-25	Coe-12	Coe-20	Coe-18	Coe-53	SCH-313	SCH-580	
Tertiary	0	0	0	0	0	0	0	0	0	0	0	0	0	0
Cretaceous	600	405	385	356.5	299	380	464	354	508	470	305	348	354	402.2
Jurassic	1173	1361.3	1277	947.5	853.5	1065	1301	873.5	1459	1017	1215	857.5	1079	1113.8
Triassic	1576	1733.5	1631	1103	1089	1340	1342.5	1052	1459	1255	1308	1453	1543	1375.8
Halite (Zechstein)	2615.3	2732.4	2615.5	1984	2177	2364	2329.5	1971	2319	2362	2259	2511	2651.5	2376.2
ZEZ2 anhydrite	2993.5	2792	2971	2842	2772	2938.5	2702.5	2610	2812	2672	2686	2802	3003	2815.1
ZEZ2 carbonaat	2998.5	2796	2973	2846.5	2775	2950	2706	2614	2814.5	2675.5	2692	2808	3012	2820.1
ZEZ1 anhydrite	3060.5	2852.5	3023.5	2905	2820.5	3041.5	2751.5	2671	2854.5	2719	2728	2928.5	3085	2880.1
ZEZ1 carbonaat	3124	2900.5	3072.5		2870.5	3103.5	2797.5	2710	2895	2755	2767	2983.3		2907.2
Coppershale	3129	2904.5	3077		2873	3108	2799.5	2712.5	2896.5	2757	2771	2984.7		2910.2
Slochteren (Rotliegend reservoir)	3130	2905	3078			3109	2800.5				2772			2965.8
Carboniferous	3137	2910.5	3080		2874	3113.5	2804	2713	2897	2758	2779	2985.7		

Figure B.1: The wells that are used for defining the model geometry of the Carbonate shallow model. Retrieved from www.nlog.nl/datacenter/brh-overview and converted to true vertical depth.

Formation	Emm-08	emm-10	emm-12	emm9	emm-14	Average
Tertiary	0	0	0	0	0	0
Cretaceous	380	328	322	383.5	296	353
Triassic	1520.6	1150	1119	1508	1236	1324
Halite (Zechstein)	1831.8	1264	1316	1831	1632.5	1561
ZEZ2 anhydrite	3313	2473	2754	3226	3024.5	2942
ZEZ2 carbonaat	3664.5	3743	3602	3533	3914	3636
ZEZ1 anhydrite	3671	3747	3617	3600	3925	3659
ZEZ1 carbonaat	3797.5	3795	3640	3690	3981	3731
Coppershale	3875	3859	3822	3898	4053	3864
ten Boer	3881.5		3824.5	3900	4056	3869
Slochteren (Rotliegend reservoir)	x	x	x	x	x	x
Carboniferous	3882		3825	3901	4057	3869

Figure B.2: The wells that are used for defining the model geometry of the Carbonate deep model. Retrieved from www.nlog.nl/datacenter/brh-overview and converted to true vertical depth.

Formation:	Well:	SDM-01	ZRP-01	PAU-01	BRH-01	ODP-01	SMR01	Average
Tertiary		0	0	0	0	0	0	0
Cretaceous		850	831	822	860	919	818	850
Triassic		1835	1810	1762.7	1713.8	1900	1883.5	1817.5
Halite (Zechstein)		1878	2025	1825	1816.65	2064	2080	1948.1
ZE2 anhydrite		2727.5	2783.5	2717	2748.2	2791	2674	2740.2
ZE2 carbonaat		2731.5	2788.5	2719.9	2753.2	2797.5	2677	2744.6
ZE1 anhydrite		2739	2796.3	2730.4	2762.2	2806	2685	2753.2
ZE1 carbonaat		2765	2824.3	2757.2	2788.1	2839	2709	2780.4
Coppershale		2774.5	2833.2	2765.7	2797.1	2842	2723	2789.3
ten Boer		2775.5	2834.2	2766.3	2798.1	2842.5	2723.5	2790.0
Slochteren (Rotliegend reservoir)		2840	2897	2821.5	2861	2913	2776	2851.4
Carboniferous		3047	3101	2995	3046.5	3136	2938.5	3044

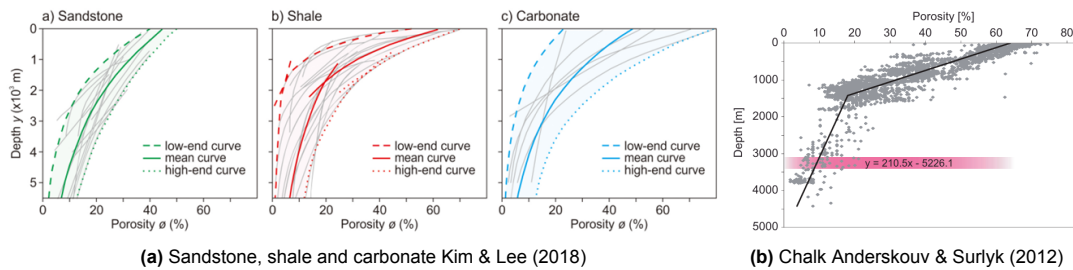
Figure B.3: The wells that are used for defining the model geometry of the Rotliegend shallow model. Retrieved from www.nlog.nl/datacenter/brh-overview and converted to true vertical depth.

Field	Nes	Mestlawier	Anjum	
Well	MGT2	ANJ02	ANJ01	Average
Formation				
Tertiary	0	0	0	0
Cretaceous	1590	1196	1222	1336
Triassic	2738	2136	2379	2417.667
Halite (Zechstein)	3063	2626	3050	2913
ZE2 anhydrite	3557	3524	3636	3572.333
ZE2 carbonaat	3561	3528	3639.5	3576.167
ZE1 anhydrite	3568	3537	3647	3584
ZE1 carbonaat	3602	3568	3680	3616.667
kopershale	3604	3572		3588
ten Boer	3604.5	3573	3688	3621.833
Slochteren (Rotliegend reservoir)	3682	3650	3760	3697.333
Carboniferous	3920	3875	4003	3932.667

Figure B.4: The wells that are used for defining the model geometry of the Rotliegend deep model. Retrieved from www.nlog.nl/datacenter/brh-overview and converted to true vertical depth.

Table B.1: Porosity values of different sources per layer

Formation	Porosity	Source																								
Tertiary	0.35	Kim & Lee (2018) (see figure below)																								
Cretaceous	0.25	Anderskov & Surlyk (2012)(see figure below)																								
Triassic	0.18	Kim & Lee (2018)(see figure below)																								
Jurassic	0.2	Kim & Lee (2018)(see figure below)																								
Halite	0.005	Fjær et al. (2008a)																								
ZEZ2A	0.02	ZEZ2C																								
ZEZ2C	0.02	<table border="0"> <tr> <td>Paulides (2016)</td> <td>2%</td> <td>Dalen</td> </tr> <tr> <td></td> <td>0-4%</td> <td>Emmen</td> </tr> <tr> <td></td> <td>1.5%</td> <td>OSH, ENA</td> </tr> <tr> <td>Tolsma (2014)</td> <td>15%</td> <td>offshore</td> </tr> <tr> <td>Peryt et al. (2010)</td> <td>2-13%</td> <td>Schoonebeek</td> </tr> <tr> <td>TNO (2009)</td> <td>10-15%</td> <td>Vlagtwedde</td> </tr> <tr> <td>de Jager & Geluk (2007)</td> <td>14%</td> <td>Best Zechstein</td> </tr> <tr> <td></td> <td>4-5%</td> <td>DAL, EMM, COE</td> </tr> </table>	Paulides (2016)	2%	Dalen		0-4%	Emmen		1.5%	OSH, ENA	Tolsma (2014)	15%	offshore	Peryt et al. (2010)	2-13%	Schoonebeek	TNO (2009)	10-15%	Vlagtwedde	de Jager & Geluk (2007)	14%	Best Zechstein		4-5%	DAL, EMM, COE
Paulides (2016)	2%	Dalen																								
	0-4%	Emmen																								
	1.5%	OSH, ENA																								
Tolsma (2014)	15%	offshore																								
Peryt et al. (2010)	2-13%	Schoonebeek																								
TNO (2009)	10-15%	Vlagtwedde																								
de Jager & Geluk (2007)	14%	Best Zechstein																								
	4-5%	DAL, EMM, COE																								
ZEZ1A	0.02	ZEZ2C																								
Ten Boer	0.07	NAM (2016)																								
Slochteren	0.15	<table border="0"> <tr> <td>Lele et al. (2015); Buijze et al. (2017)</td> <td>15-20%</td> </tr> <tr> <td>de Jager & Visser (2017)</td> <td>10-26%</td> </tr> <tr> <td>NAM (2013)</td> <td>15%</td> </tr> <tr> <td>Orlic (2016)</td> <td>20%</td> </tr> </table>	Lele et al. (2015); Buijze et al. (2017)	15-20%	de Jager & Visser (2017)	10-26%	NAM (2013)	15%	Orlic (2016)	20%																
Lele et al. (2015); Buijze et al. (2017)	15-20%																									
de Jager & Visser (2017)	10-26%																									
NAM (2013)	15%																									
Orlic (2016)	20%																									
Carboniferous	0.07	Kim & Lee (2018)(see figure below)																								

**Figure B.5:** Porosity vs depth curves, used in table B.1.

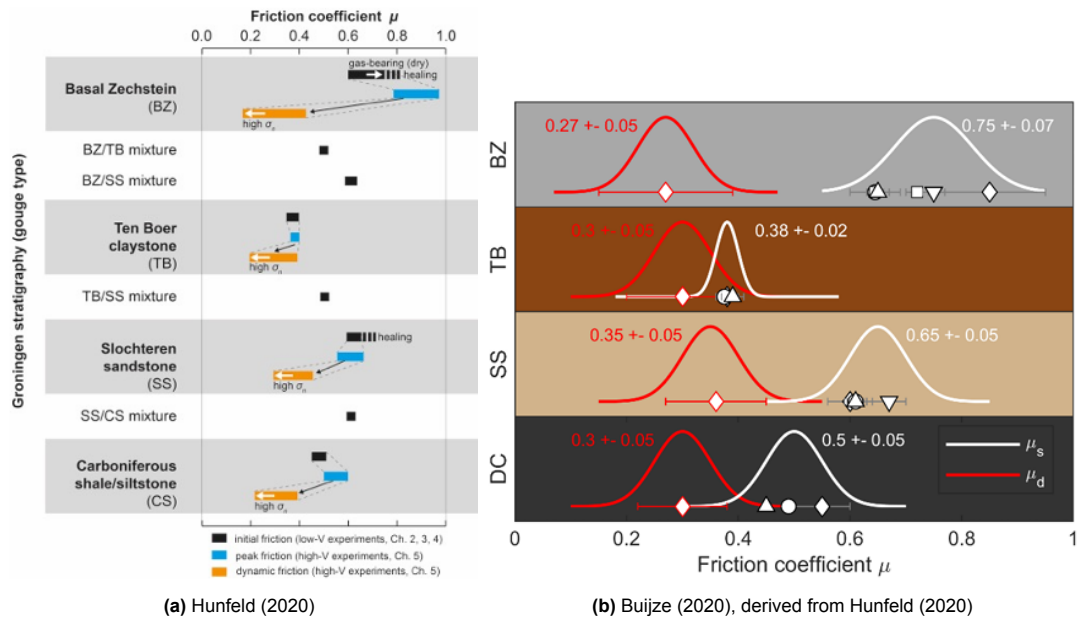
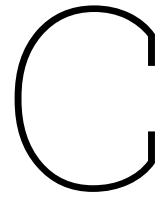


Figure B.6: Static and Dynamic friction coefficients.



Results

The results that are shown include the 2D results of the horizontal and vertical strain and the K_0 ratio for all phases of the Carbonate deep, Rotliegend 1/4 and 3/4 model, as these are not shown in the text. The lay-out of the figures is similar to the layout of the Carbonate shallow figures in the text.

2D Deformation Horizontal strain:

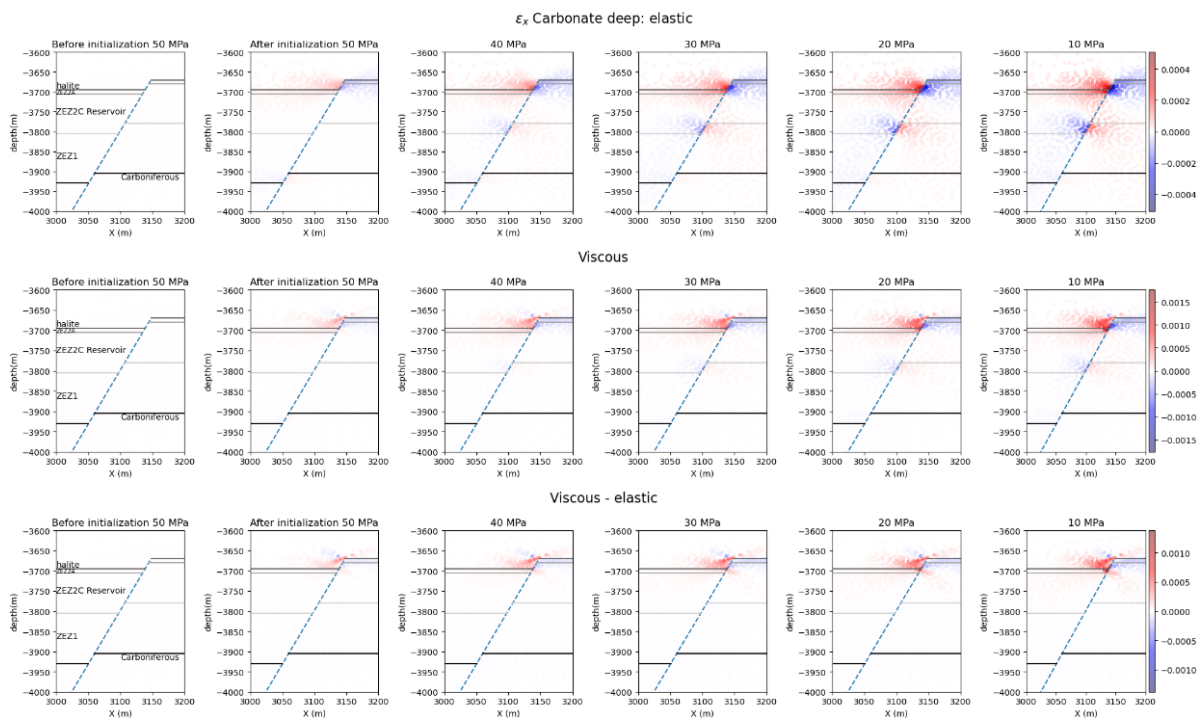


Figure C.1: ϵ_{xx} for all phases of the elastic and viscous Carbonate deep model. Top row is the elastic model, middle row the viscous model, and the bottom row the difference between the viscous and elastic model. From left to right the pressure is depleting corresponding to the phases given in table 5.5.

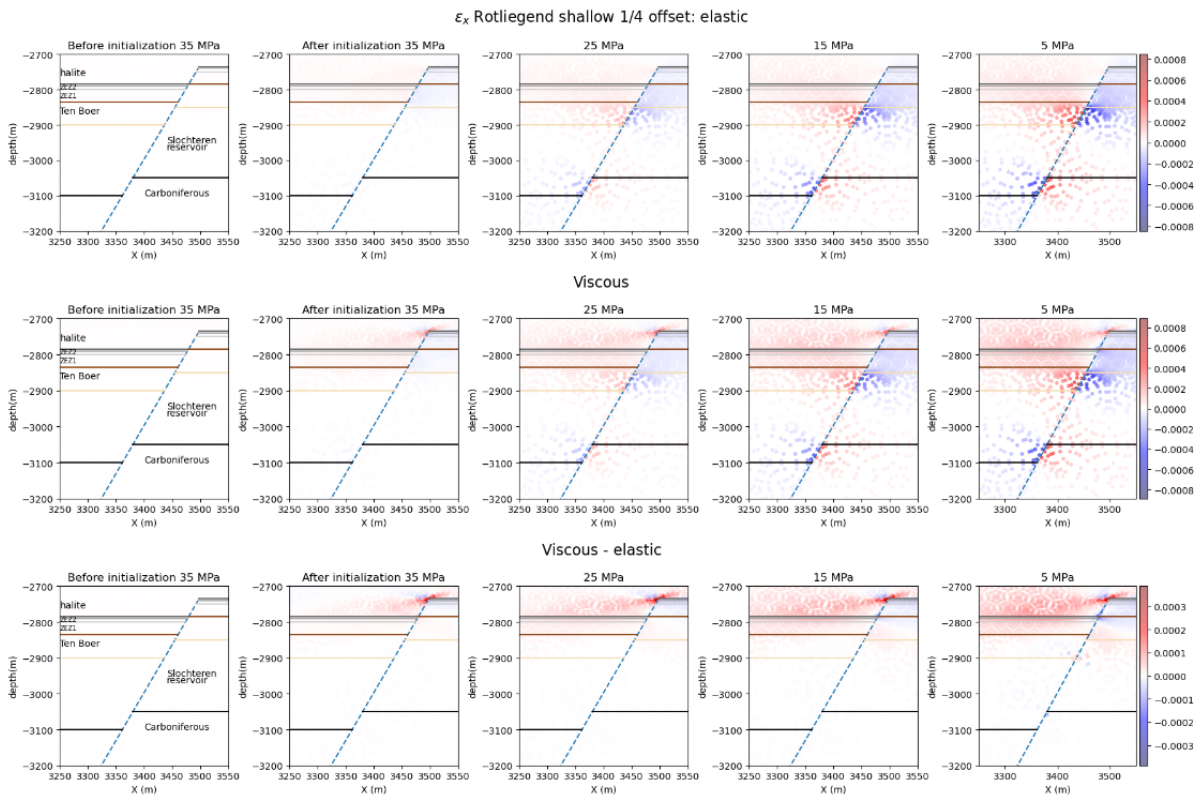


Figure C.2: ϵ_{xx} for all phases of the elastic and viscous RS1 model. Top row is the elastic model, middle row the viscous model, and the bottom row the difference between the viscous and elastic model. From left to right the pressure is depleting corresponding to the phases given in table 5.5.

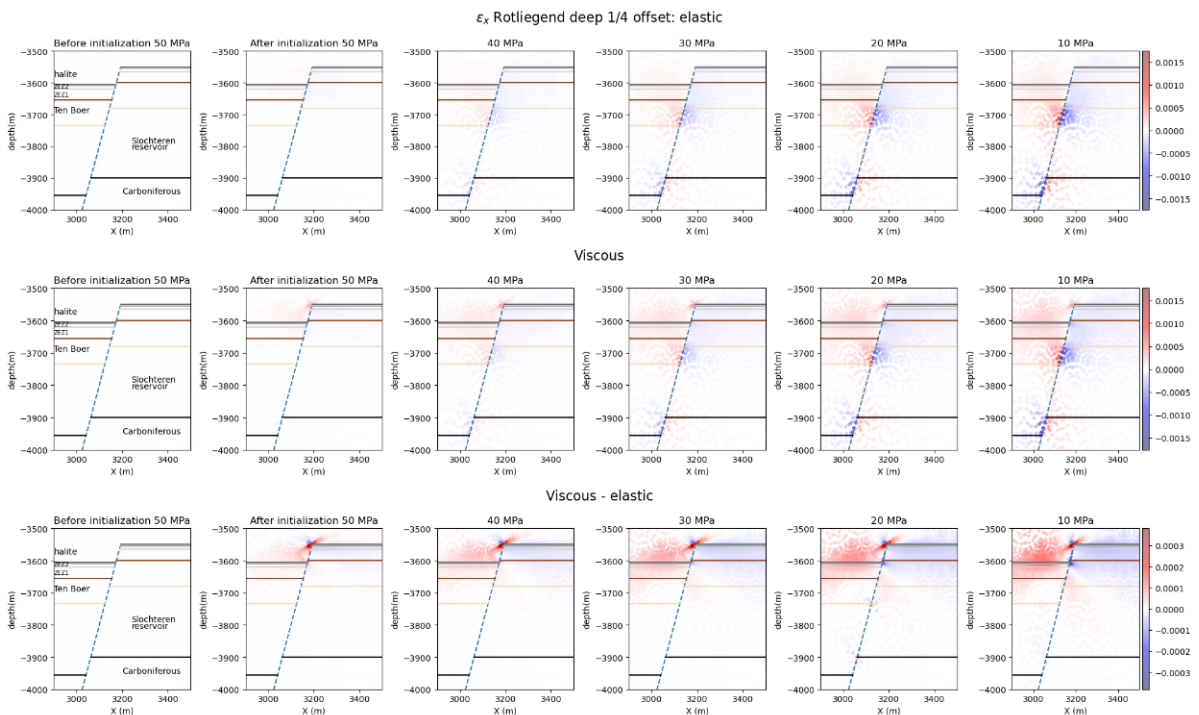


Figure C.3: ϵ_{xx} for all phases of the elastic and viscous RD1 model. Top row is the elastic model, middle row the viscous model, and the bottom row the difference between the viscous and elastic model. From left to right the pressure is depleting corresponding to the phases given in table 5.5.

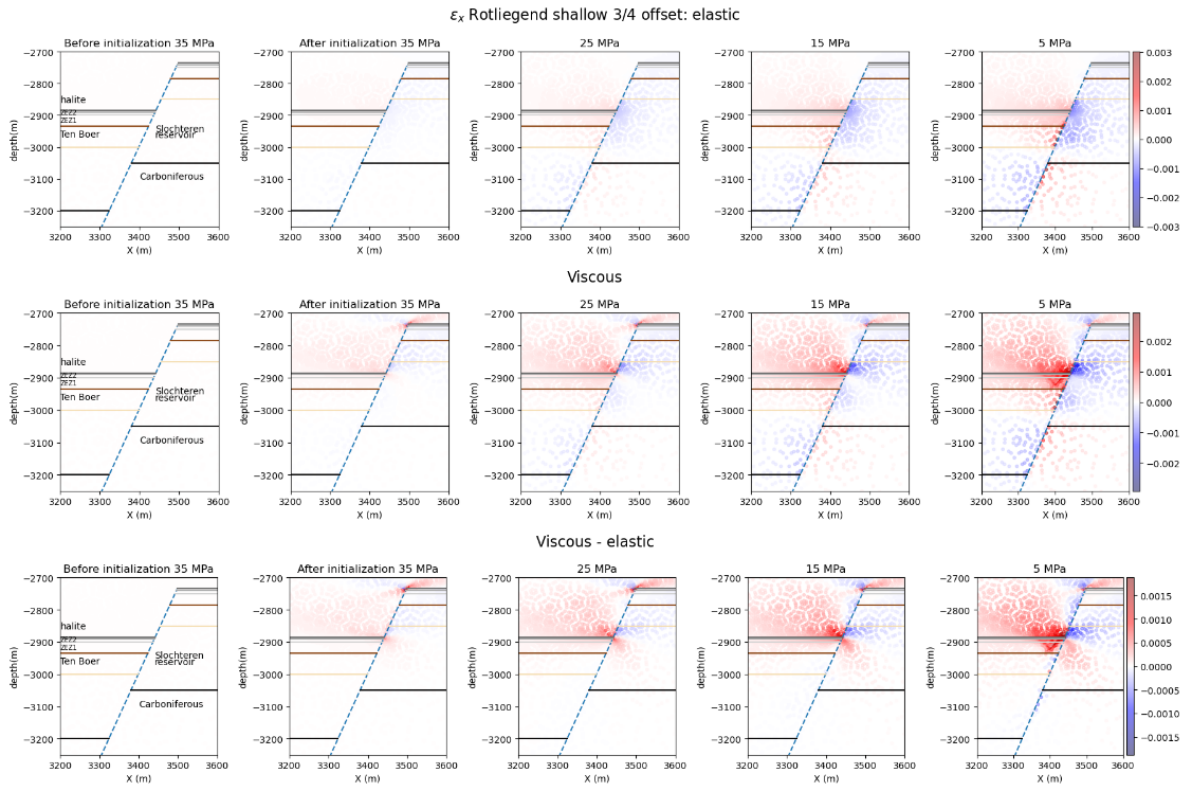


Figure C.4: ϵ_{xx} for all phases of the elastic and viscous RS3 model. Top row is the elastic model, middle row the viscous model, and the bottom row the difference between the viscous and elastic model. From left to right the pressure is depleting corresponding to the phases given in table 5.5.

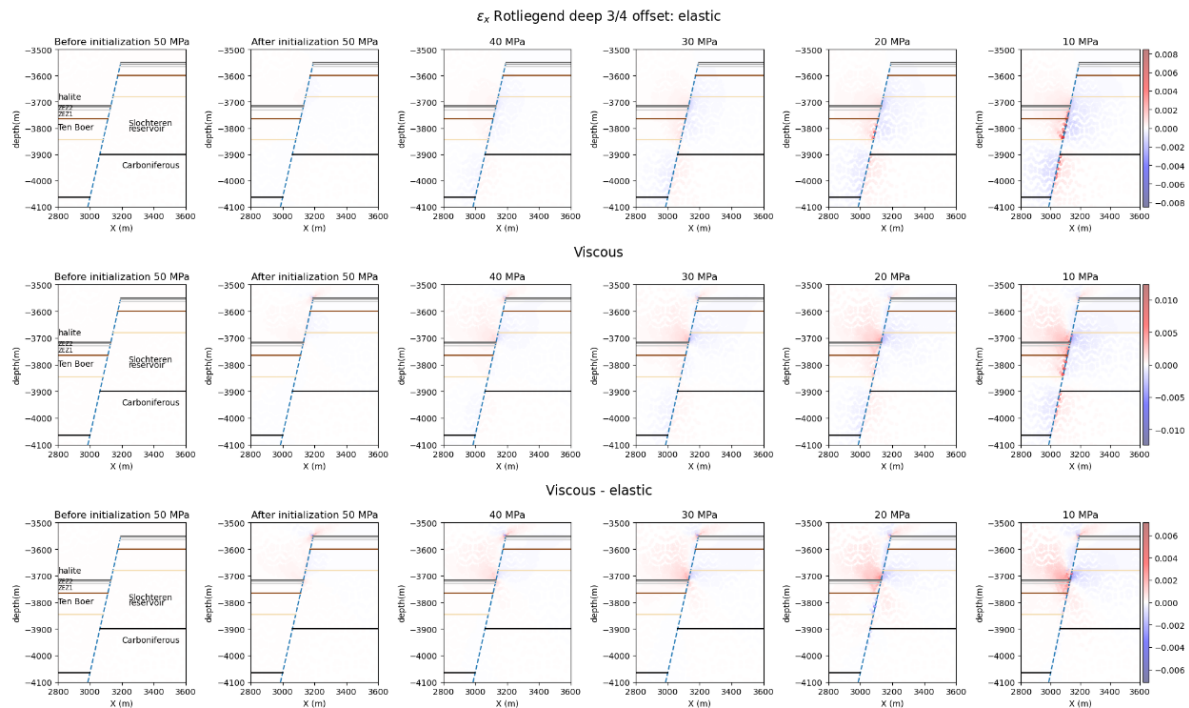


Figure C.5: ϵ_{xx} for all phases of the elastic and viscous RD3 model. Top row is the elastic model, middle row the viscous model, and the bottom row the difference between the viscous and elastic model. From left to right the pressure is depleting corresponding to the phases given in table 5.5.

Vertical strain:

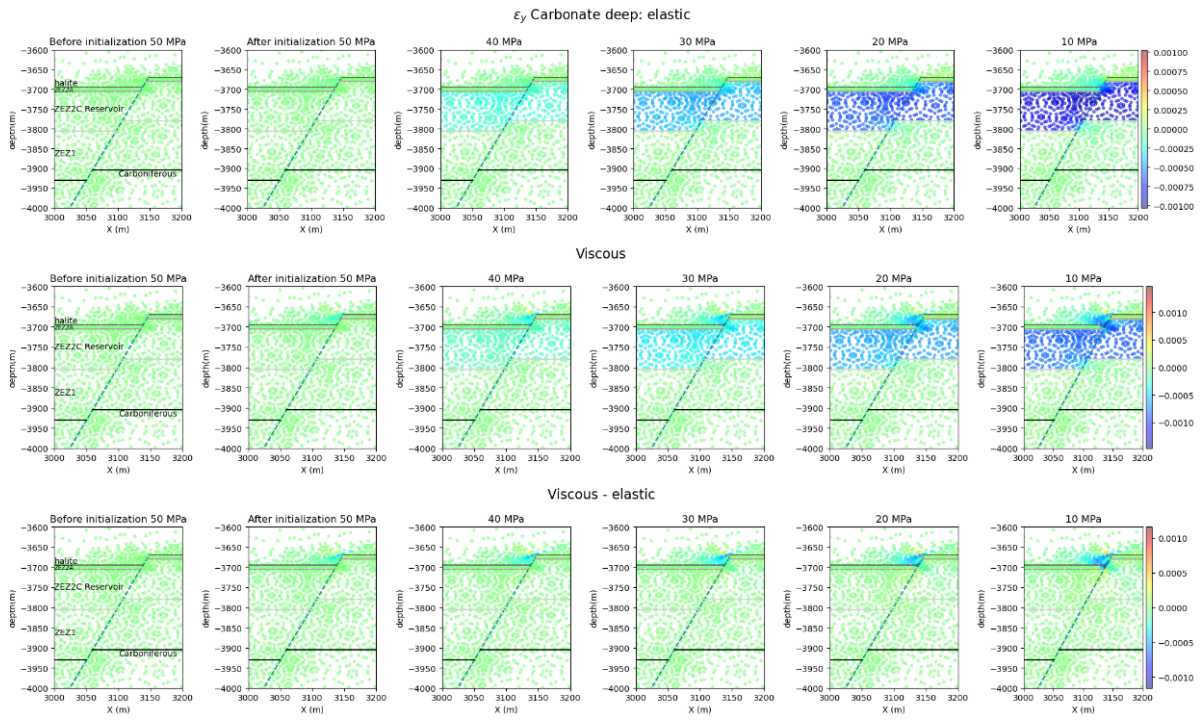


Figure C.6: ϵ_{yy} for all phases of the elastic and viscous Carbonate deep model. Top row is the elastic model, middle row the viscous model, and the bottom row the difference between the viscous and elastic model. From left to right the pressure is depleting corresponding to the phases given in table 5.5.

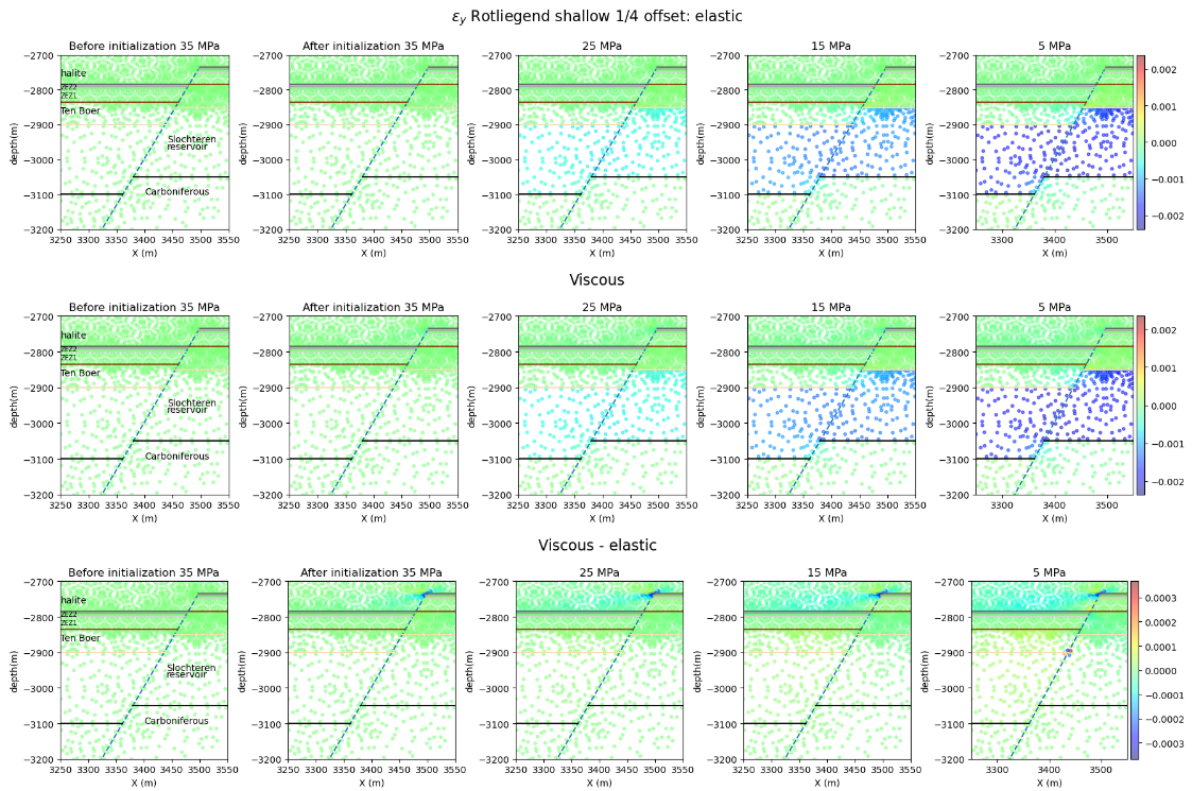


Figure C.7: ϵ_{yy} for all phases of the elastic and viscous RS1 model. Top row is the elastic model, middle row the viscous model, and the bottom row the difference between the viscous and elastic model. From left to right the pressure is depleting corresponding to the phases given in table 5.5.

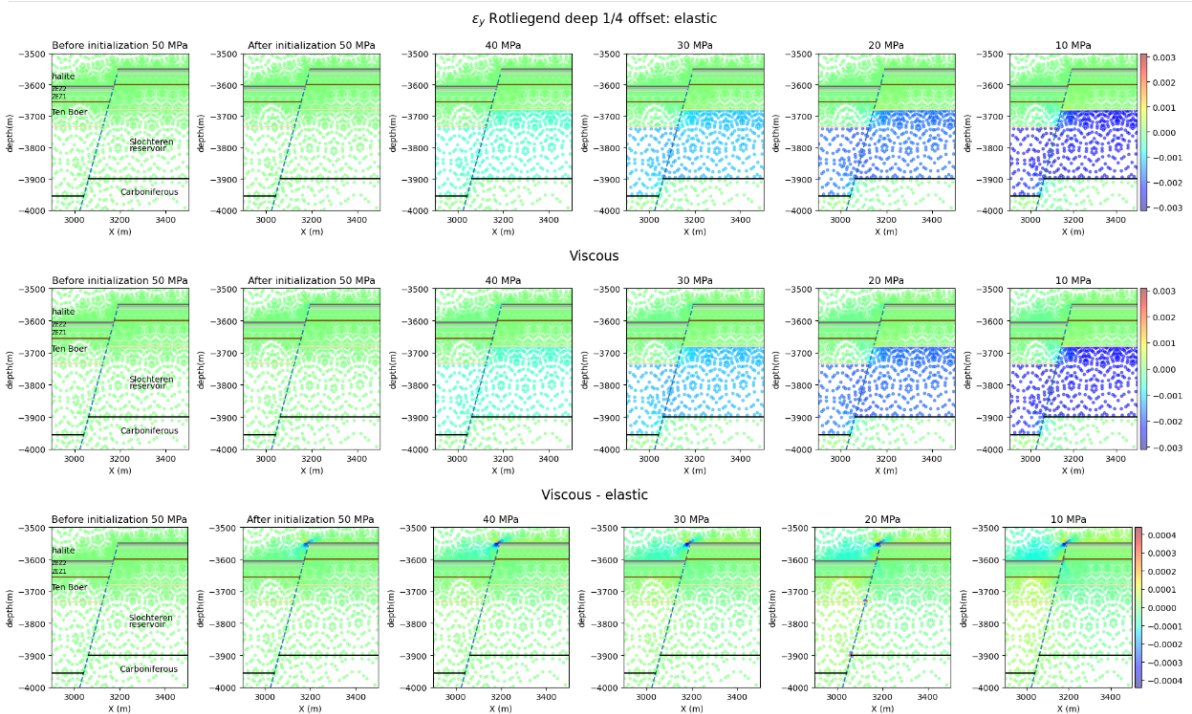


Figure C.8: ϵ_{yy} for all phases of the elastic and viscous RD1 model. Top row is the elastic model, middle row the viscous model, and the bottom row the difference between the viscous and elastic model. From left to right the pressure is depleting corresponding to the phases given in table 5.5.

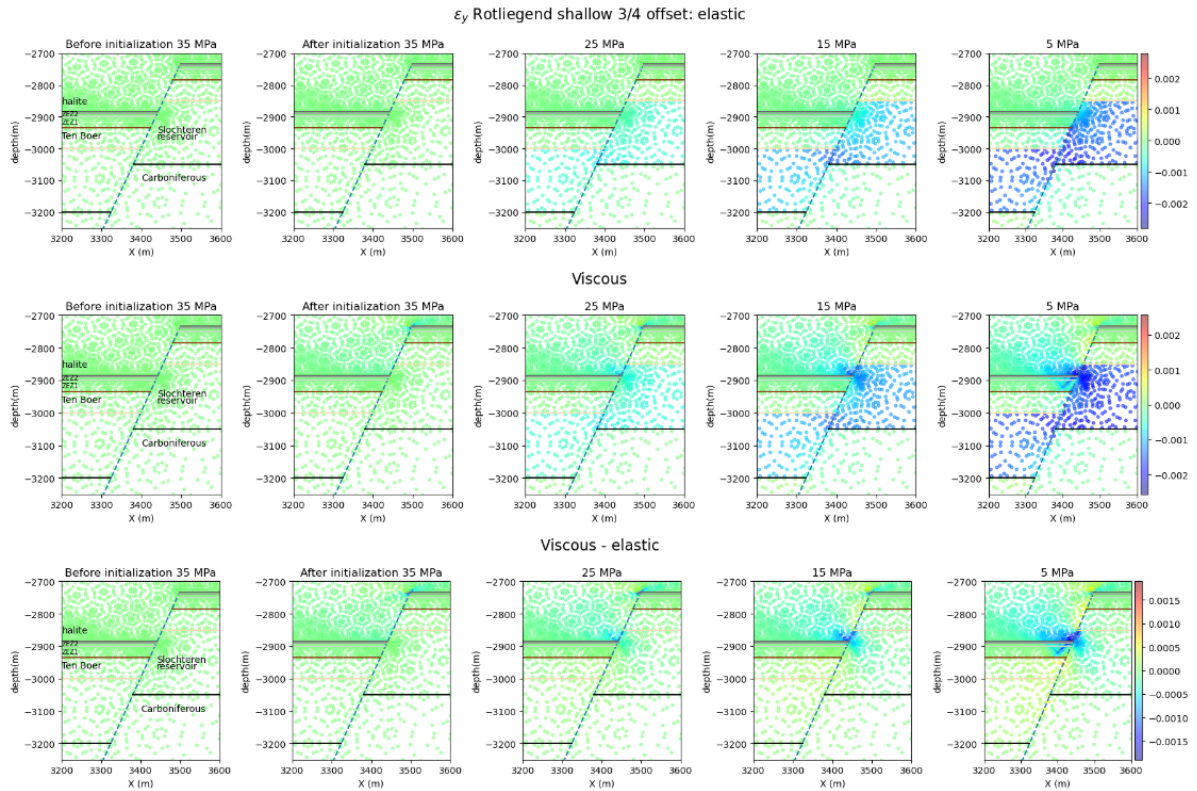


Figure C.9: ϵ_{yy} for all phases of the elastic and viscous RS3 model. Top row is the elastic model, middle row the viscous model, and the bottom row the difference between the viscous and elastic model. From left to right the pressure is depleting corresponding to the phases given in table 5.5.

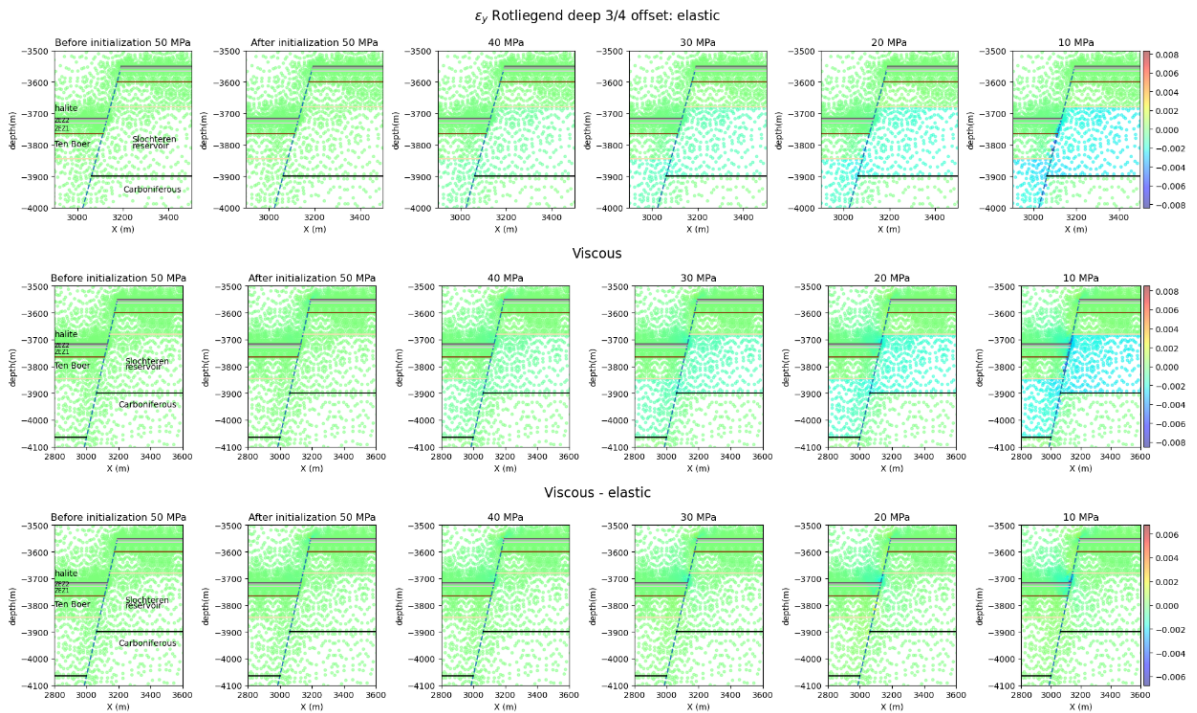


Figure C.10: ϵ_{yy} for all phases of the elastic and viscous RD3 model. Top row is the elastic model, middle row the viscous model, and the bottom row the difference between the viscous and elastic model. From left to right the pressure is depleting corresponding to the phases given in table 5.5.

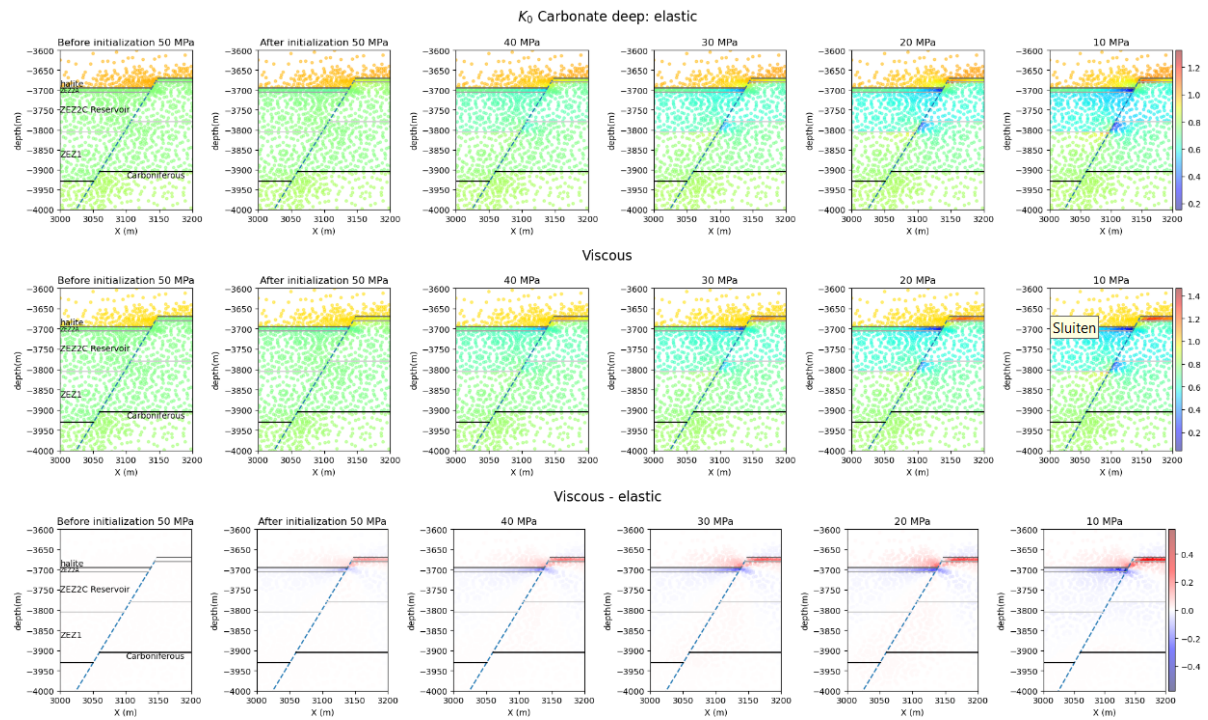
2D K_0 ratio

Figure C.11: K_0 ratio for all phases of the elastic and viscous Carbonate deep model. Top row is the elastic model, middle row the viscous model and the bottom row the difference between the viscous and elastic model. From left to right the pressure is depleting corresponding to the phases given in table 5.5.

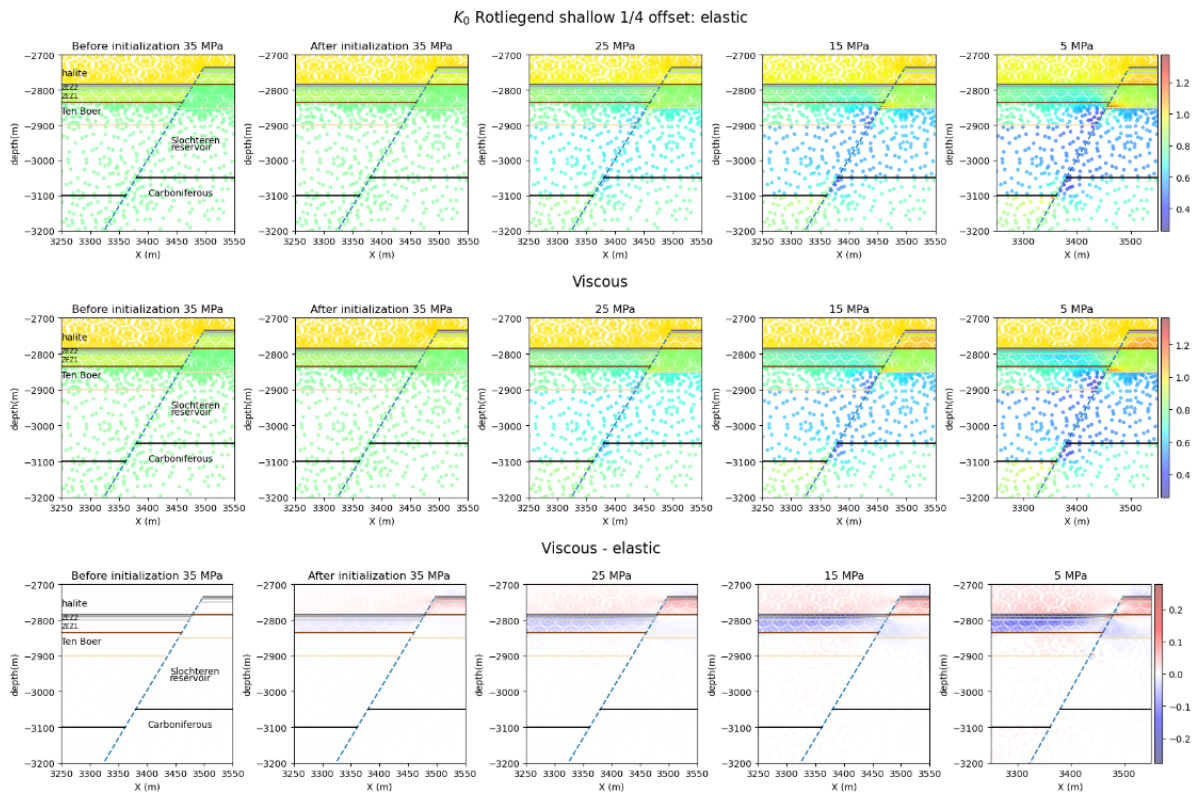


Figure C.12: K_0 ratio for all phases of the elastic and viscous RS1 model. Top row is the elastic model, middle row the viscous model and the bottom row the difference between the viscous and elastic model. From left to right the pressure is depleting corresponding to the phases given in table 5.5.

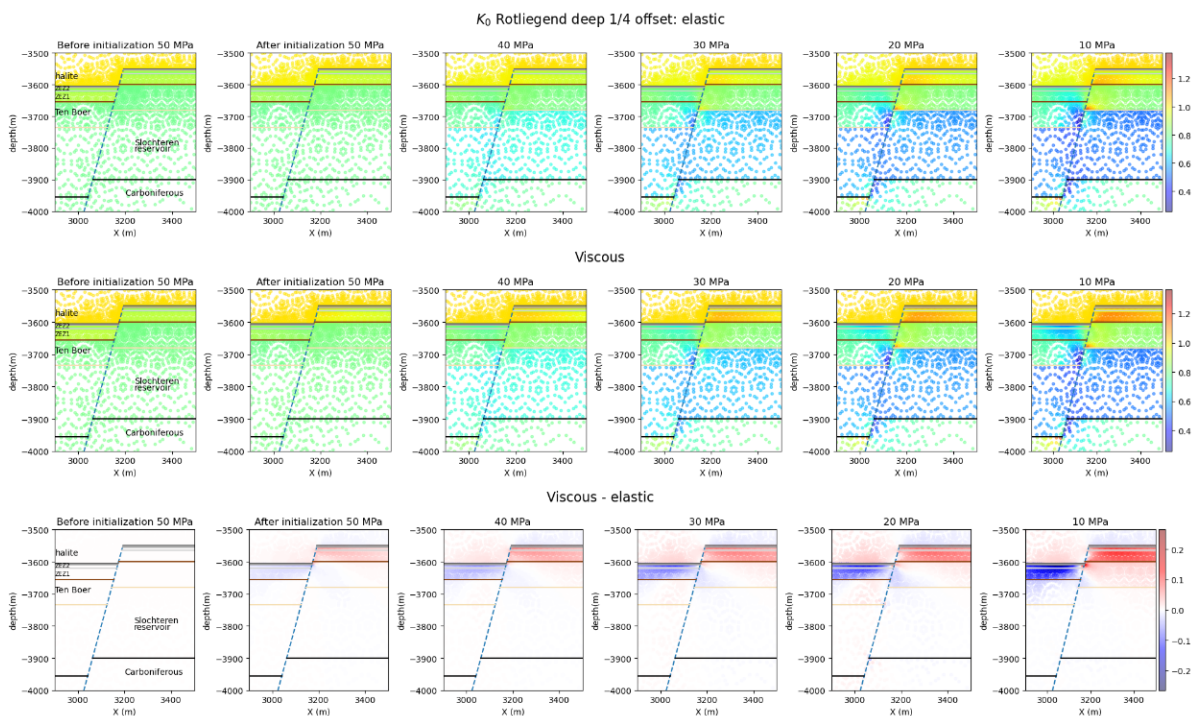


Figure C.13: K_0 ratio for all phases of the elastic and viscous RD1 model. Top row is the elastic model, middle row the viscous model and the bottom row the difference between the viscous and elastic model. From left to right the pressure is depleting corresponding to the phases given in table 5.5.

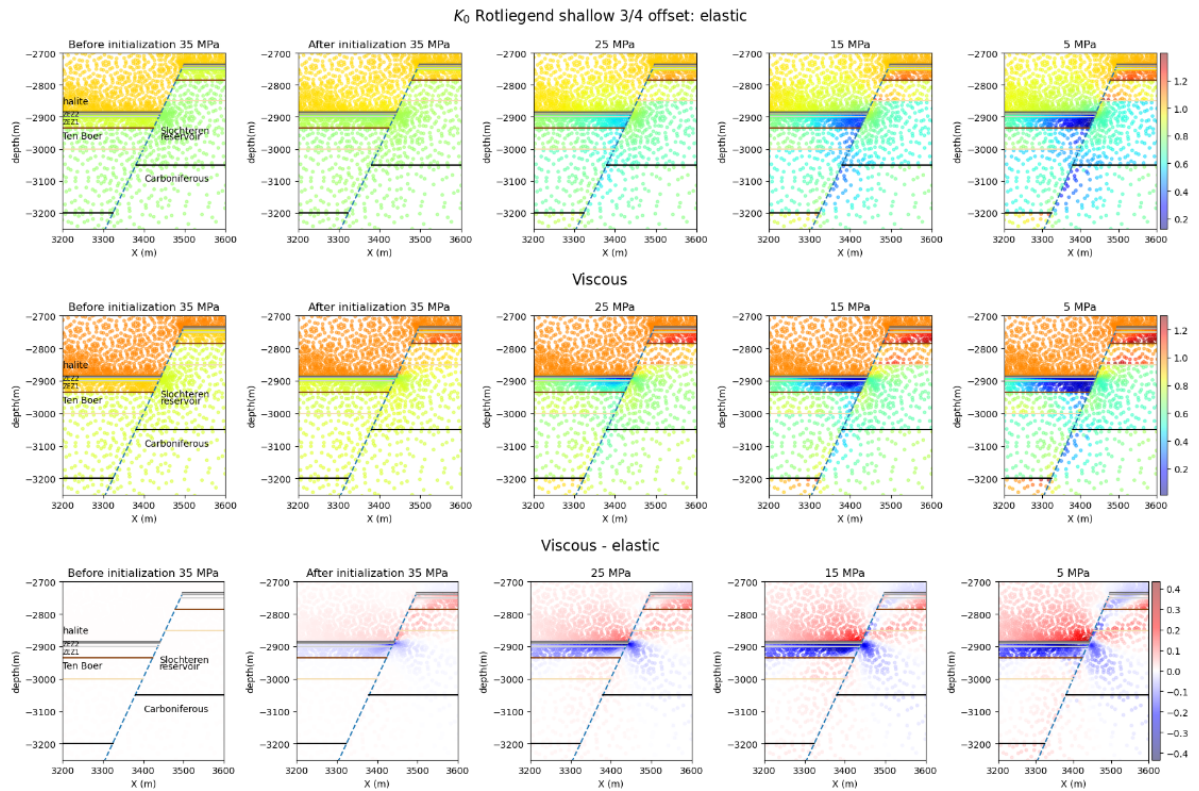


Figure C.14: K_0 ratio for all phases of the elastic and viscous RS3 model. Top row is the elastic model, middle row the viscous model and the bottom row the difference between the viscous and elastic model. From left to right the pressure is depleting corresponding to the phases given in table 5.5.

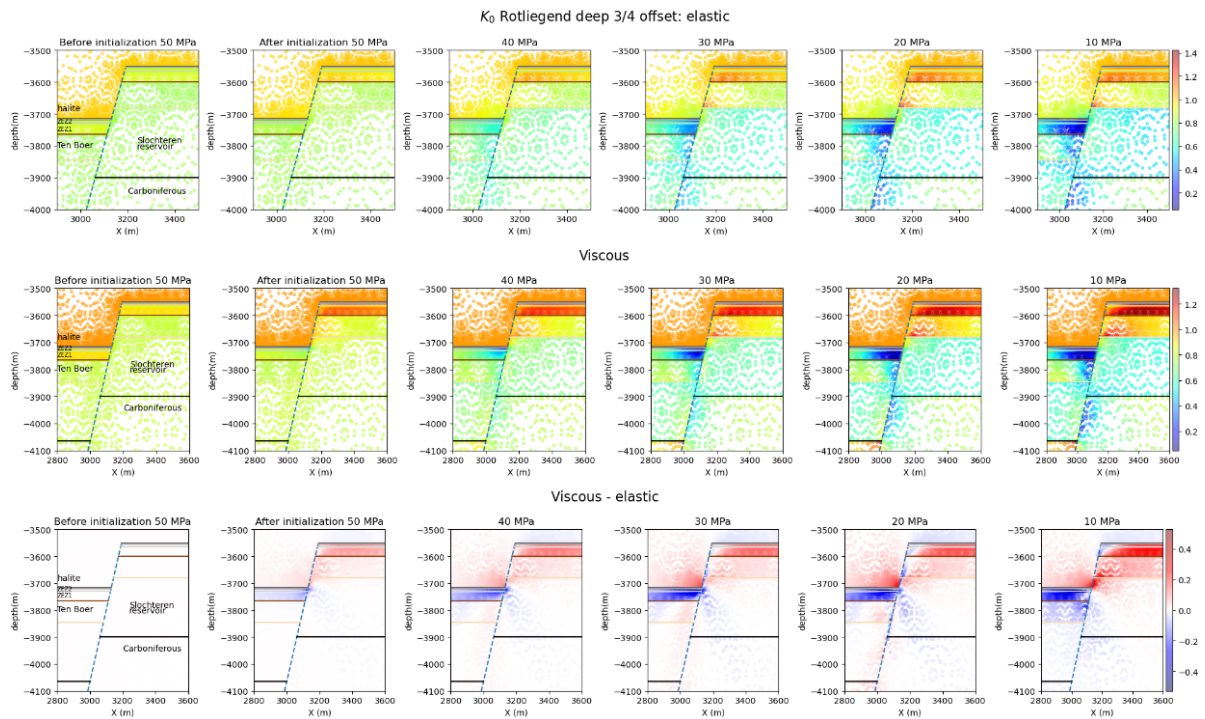


Figure C.15: K_0 ratio for all phases of the elastic and viscous RD3 model. Top row is the elastic model, middle row the viscous model and the bottom row the difference between the viscous and elastic model. From left to right the pressure is depleting corresponding to the phases given in table 5.5.

Results summary

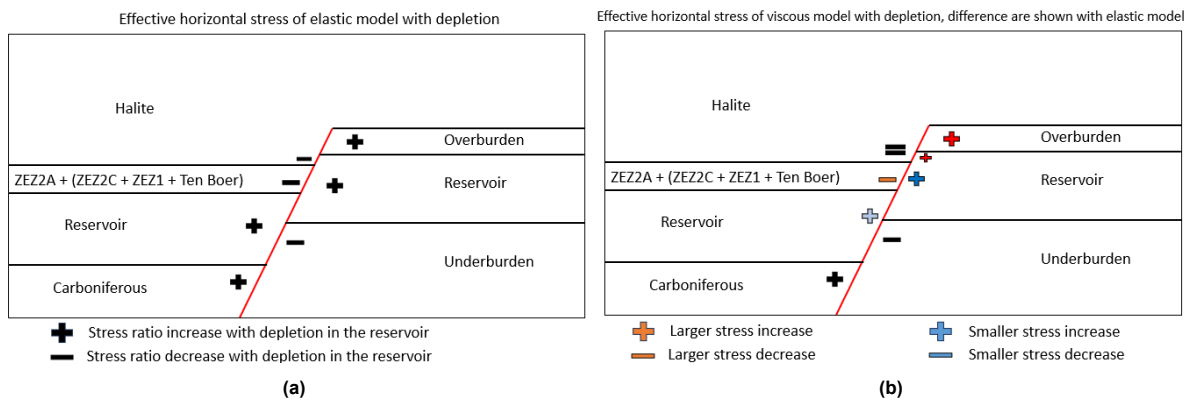


Figure C.16: Effective horizontal stress change with depletion. For the elastic model (a) and the viscous model (b). The viscous figure does also indicate the relative change in stress with the elastic model. If the plus or minus sign is black in (b), there is no difference between the viscous and elastic model. The darker the colour, the larger the difference.

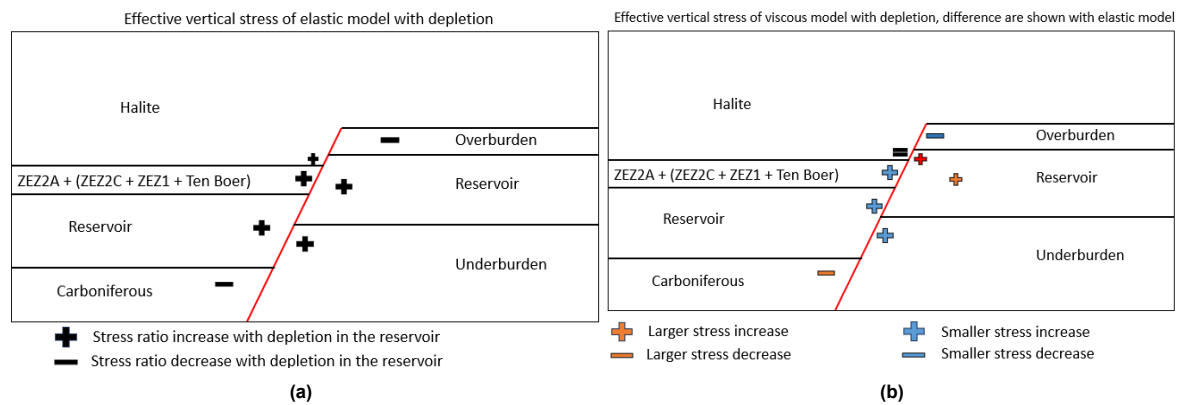


Figure C.17: Effective vertical stress change with depletion. For the elastic model (a) and the viscous model (b). The viscous figure does also indicate the relative change in stress with the elastic model. The darker the colour, the larger the difference.

D

Discussion

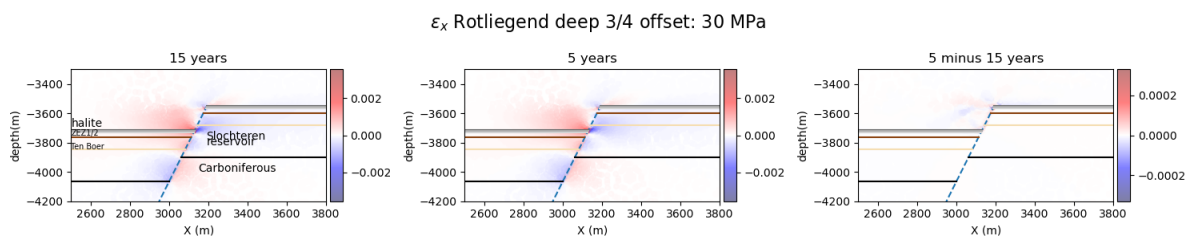


Figure D.1: Difference in horizontal strain between time interval of 15 and 5 years.

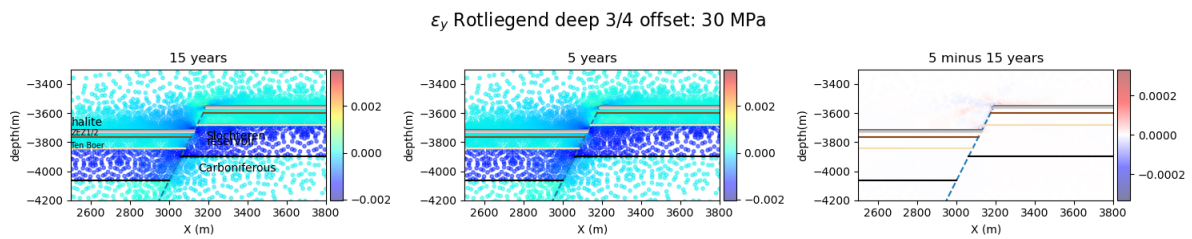


Figure D.2: Difference in vertical strain between time interval of 15 and 5 years.

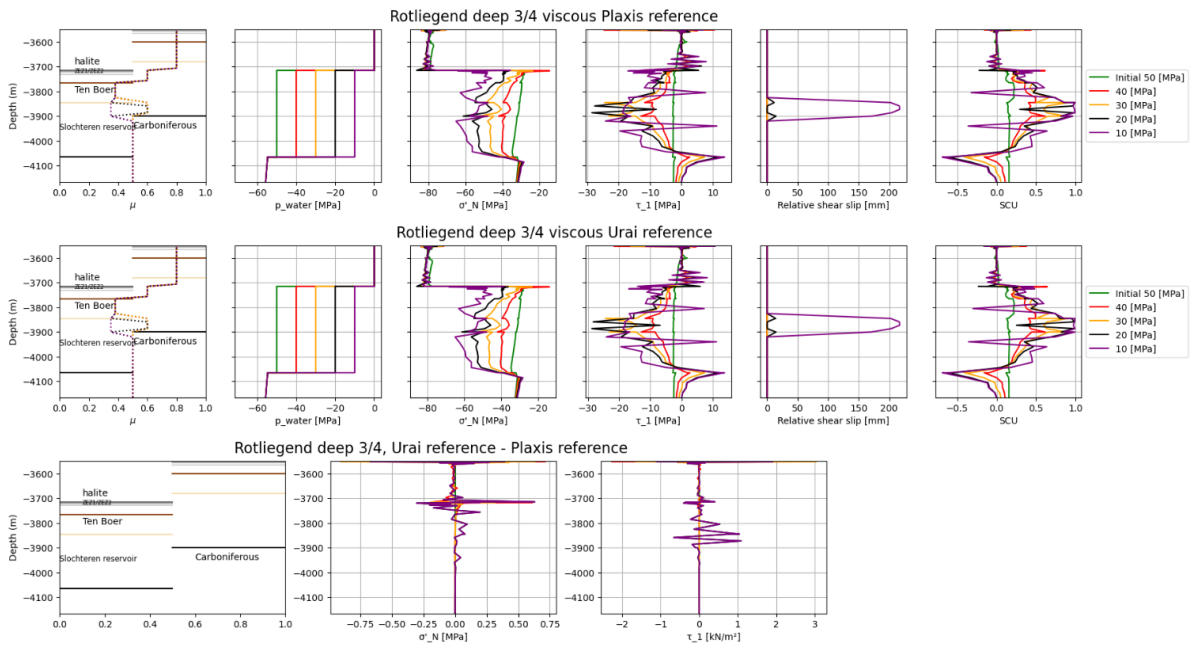


Figure D.3: Stresses acting on fault for different fault sources (Plaxis, 2022; Li & Urai, 2016). Also the difference between the two are plotted. This figure has been made in an early stadium of the project, after which minor changes have been made to the model.